EXPERIMENTAL INVESTIGATIONS OF FLUID–MINERAL INTERACTIONS IN OLIVINE AND DOLOMITE

A Dissertation
Presented for the
Doctor of Philosophy Degree
The University of Tennessee, Knoxville

Michael Thomas DeAngelis
December 2011

Dedication

This dissertation is dedicated to my father, my sister, and my brother. Rob, you always give me laughter when I need it most. Becky, you are always there to listen when I need to be sad. Dad, you are always there to take care of the rest. Thank you.

Acknowledgments

The pages of this dissertation only exist because of the unending patience, guidance and support I have received from my advisor, Theodore C. Labotka. Thank you for giving me that first chance to come to graduate school back in 2002, and thank you for bringing me back for my doctorate in 2006 after I had temporarily gone astray. You never let me give up, even when I really, really, REALLY wanted to.

I am also deeply indebted to David R. Cole, without whom none of this work would have been possible. Dave graciously opened up his labs at Oak Ridge National Lab to me, and was ceaseless in his support of this work. Thank you so much for teaching me how some problems just need a little muscle, especially when the problem is opening a cold-seal vessel! I would also like to thank my other committee members David B. Finkelstein, Harry Y. McSween Jr., and Claudia J. Rawn. Dave, I doubt I would have made it through this degree if I had not had our many conversations over cups of coffee, bowls of Tom Kha soup, and bottles... many bottles... of scotch!. Hap, thanks for showing me, by example, how to focus and just get things done. Claudia, thanks for asking about that rock on the table during my preliminary exams. I was so happy when you did, because it was the only thing I was certain I could talk about with a moderate amount of confidence. I must also acknowledge the tutelage of my unofficial sixth committee member, Larry M. Anovitz. Thank you, Larry, for always having the random answer to the random question I would randomly ask.

There have been so many people within the UT Department of Earth and Planetary Sciences that I will be forever be indebted to. Linda Kah stepped in with financial, and often emotional, support just when I needed it most. Thank you, Bill

Deane, for always finding ways to keep me teaching in the classroom where I am most happy. Colin Sumrall, Larry Taylor, Larry McKay, Alan Patchen, and the other UT faculty – thank you for supporting me through all of this each in your own unique ways. I, of course, need to thank the two most important people in the UT EPS department, Melody Branch and Teresa Parrott. How would any of us grad students survive without you both? Thank you, thank you, thank you!

I would also like to thank my collaborators outside the university. Mostafa Fayek at the University of Manitoba has always been gracious with SIMS time and advice. Without the help of Michelle Pawel, Adam Rondinone, and others at the Center for Nanophase Materials Science at ORNL, the fayalite synthesis project never would have been as successful as it was. Thank you to Harry Meyer, Tracey Brummett and Larry Walker at HTML for help with XPS and SEM analyses. I must also sincerely thank all the members of the Geochemistry and Interfacial Sciences group at ORNL for use of labs and for many helpful conversations about science.

Perhaps the most important people in making this all possible were my graduate student friends at UT. Thank you to all of the friends I first got to know during my M.S. degree: Chris and Jen Whisner, Jeff Nettles, Rhiannon Mayne, Whitney Nelson, Melissa Hage, Arthur Merschat, Tabbatha Cavendish, Cara Thompson, Craig Hardgrove, and so many others, and for all the great friends I have made during my Ph.D degree: René Shroat-Lewis, Will Atwood, Megan Ennis, Jackie and Paul Langille, Kevin Thaisen, Sharon Hull, and a whole bunch more. You have each meant so much more to me than you will ever know. Thank you to Jason and Joselynn Birner, Lisa and Joe Welke, Kim Barden, Zeb Page, and many other non-grad student friends for supporting me even

though you may not have any idea what I do or why I am doing it! I want to thank Ralph and Marge Lawson for being great neighbors and my surrogate parents for all the years of this dissertation. A special thanks also to William Peck, my undergraduate petrology T.A., collaborator, mentor, and friend for guiding me through all this. I also want to thank David for being there at the beginning and Kelsey for being there at the end.

Finally, thank you to each and every member of my family: Granny Mitzi, Granddad Russ, Grandma Lucy, Papa Frank, Aunt Sarah, Aunt Lynn, Aunt Jane, Uncle Devan, Aunt Piper, Uncle John, Cousin Steven, Cousin Jeanne, Cousin Matthew, Niece MaKayla, Nephew Sebastian, Niece Emmalisa, Nephew Parker, Sister Angie, Brother Rob, Sister Becky, Dad Mark and Mom Robin. Some of you are no longer around to actually see me finish this thing, but each of you has been so important in helping me along the way. Thank you so much. I will love each of you always.

Abstract

Geochemical processes involving the interaction of fluids and minerals occur in nearly every environment on the surface and in the crust of the Earth. The variety of fluid–mineral processes on the Earth is quite diverse, and these various processes can occur under a large range of geochemical conditions. Aqueous dissolution and alteration, hydration, protonation, solution–precipitation, diffusion, and fluid and isotope exchange are among the many fluid–mineral interaction processes that contribute to the overall cycling of elements on Earth. This dissertation uses analog experiments to examine fluid–mineral interaction processes found in different geological environments and under a range of environmental conditions. The first part of this dissertation examines the reactive and diffusive exchange of oxygen isotopes that results from performing a dolomite breakdown experiment under a temperature, pressure, and fluid condition analogous to a contact metamorphic environment. The second two parts of the dissertation involve the development of new methods for the growth of nanocrystalline fayalite and intermediate composition olivine. The final two parts of this dissertation focus on the interaction of olivine with either H_2O or acidic solutions (0.005 M H_2SO_4 or 0.01 M HCl) at low temperature and pressure. The first of these two parts experimentally uses different surface area olivine powders that are reacted with low pH fluids in non-buffered, closed system experiments where pH and solution composition are allowed to change. The second of these two parts uses various analytical techniques that can examine changes to the surfaces of olivine single crystals at the nanoscale resulting from experiments performed under environmental conditions where the fluid–mineral

interaction transitions from dissolution at low temperature and pressure to alteration at moderate temperature and pressure. Though the individual projects contained within this dissertation are varied, they share the common theme of using experiments to examine fluid–mineral interaction processes.

Table of Contents

List of Tables

List of Figures

Part I.
Introduction

1. Overview

1.1. Fluid–mineral interactions

Geochemical processes involving the interaction of fluids and minerals occur in nearly every environment on the surface of and in the crust of the Earth. The evolution and diversity of mineralization on Earth, for example, began with the aqueous alteration of minerals (e.g. Mg-olivine, Mg-pyroxene, Fe-Ni metal, FeS, and others) found in differentiated planetesimals that formed the Earth during planetary accretion (Hazen et al., 2008). The origin of water on Earth and its role at the beginning of Earth history is often debated (e.g. Morbidelli et al., 2000; Robert, 2001; Drake and Righter, 2002; Valley et al., 2002), but it is clear that fluids and minerals began to react to form hydrous minerals (e.g. phyllosilicates, hydroxides, sulfates, and many others) within the first few million years following planet formation (Hazen et al., 2008). The number of fluid–mineral processes occurring at present on the Earth is quite large, and these processes occur in many different environments under a large range of geochemical conditions. Aqueous dissolution and alteration, hydration, protonation, solution–precipitation, diffusion, and fluid and isotope exchange are among the many fluid–mineral interaction processes that contribute to the overall cycling of elements on Earth.

Chemical weathering of minerals is perhaps the most significant interaction between fluids and minerals on the surface of the Earth. This type of weathering results in large fluxes of ions being removed from continental crust and transported, generally by fluvial processes, to the oceans (Chester, 2003). There are four major cations (Na^{+}, Mg^{2+}, Ca^{2+}, K^{+}) that contribute most to the overall chemistry of seawater, and low-temperature weathering of continental crust is one of the primary sources for this material (Chester,

2003). Dissolution is the most common mechanism of chemical weathering under the low temperature and pressure, fluid-rich environmental conditions on the surface (Brantley, 2008). Minerals with isolated silicon-oxygen tetrahedral structure, such as olivine, are the most susceptible group of minerals to this process. The dissolution of olivine, for example, is a major contributor to the nearly 1.4×10^{14} g of Mg^{2+} that are added to the oceans every year (Richardson and McSween, 1989).

Within the oceans, there are several processes of fluid–mineral interaction that occur simultaneously. For example, the circulation of hydrothermal fluid through oceanic crust adjacent to mid-ocean ridges results in competing processes of mineral dissolution, cation diffusion, solution–precipitation, and the formation of secondary mineral phases by hydration reactions (Alt, 1995). The dominant process at any given location is dependant on the environmental conditions at that location. Increases in temperature and pressure with depth can result in transition from mostly dissolution and solution-precipitation processes near the ocean floor–ocean crust interface, to the hydration of mineral phases through alteration reactions (e.g. serpentinization) at depth within ocean crust. The hydration and alteration of minerals in this environment results in a large volume increase and density change of oceanic crustal rocks, and may play a significant role in the motion of tectonic plates (Labotka et al., 2006).

Subduction of ocean crust at ocean-continent convergent plate boundaries results in dehydration reactions that releases volatiles to the fluids contained within the overlying continental crust rocks. For example, the mixed H_2O-CO_2 fluids associated with the emplacement of granitic plutons in contact metamorphic aureoles are often composed of

both mantle- and meteoric-derived fluids, where exchange between the two is driven by thermal and chemical potential gradients (e.g. Nabelek et al., 1984).

The intent of this dissertation is to experimentally examine fluid–mineral interaction processes as they apply to some of the various environments and environmental conditions described above. The dissertation is divided into five parts (II through VI) representing individual research papers, each of which has already been or soon will be submitted for peer review and publication in scientific journals. Though the individual projects contained within this dissertation are somewhat varied, they all share the common theme of using experiments to examine different aspects of fluid–mineral interaction. The last four parts (III through VI) are all in some way focused on the interaction of fluids with the mineral olivine, either through growth and cation exchange within new crystals (III and IV) or the dissolution, alteration, and hydration on surfaces of natural olivine crystals (V and VI). The first part (II) instead uses dolomite as the starting material for experiments, but is still focused on the fluid-driven processes of mineral reaction, solution-precipitation, diffusion, and isotope exchange.

1.2. Fluid–mineral interactions in dolomite – Part II

The first part (II) of this dissertation examines the reactive and diffusive exchange of oxygen isotopes that resulted from performing a dolomite breakdown experiment under a temperature, pressure, and fluid condition analogous to a contact metamorphic environment. The experiment described in this section of the dissertation was originally performed for a study of reaction kinetics associated with dolomite breakdown (DeAngelis et al., 2007), but was re-examined here to investigate the exchange of oxygen isotopes as it relates to processes of diffusion, solution-precipitation, and fluid-enhanced

reaction and recrystallization. This study compared electron probe microanalysis X-ray images of both reacted and non-reacted zones with ion images and quantitative isotope spot analyses collected with a secondary ion mass spectrometer (SIMS) to investigate the locations and extent of oxygen isotope exchange.

1.3. Crystal growth of olivine – Parts III and IV

These two parts of the dissertation involve the development of new methods for the growth of olivine. Part III describes the development of a new sol-gel synthesis technique for the growth of nanocrystalline fayalite (nanofayalite). The sol-gel synthesis method is a wet chemical technique in which a solution containing a mixture of chemicals is refluxed and produces an amorphous gel over some period of time (Park et al., 1993). This pre-cursor gel is then dried and calcined at a temperature and pressure of interest, generally with close attention paid to the atmospheric environment during calcination. For the production of nanofayalite, careful control of oxygen fugacity (fO_2) was necessary to prevent the oxidation or reduction of iron.

Part IV of this dissertation describes a flux growth technique developed with the intention of producing intermediate composition olivine ($MgFeSiO_4$) for use in Mars olivine analog experiments. This flux growth method used a lithium borate flux to dissolve a 1:1:1 mixture of magnesite ($MgCO_3$), siderite ($FeCO_3$), and silica powder (SiO_2). The advantage of using a flux is that the components contained within the flux dissolve at a temperature significantly below the melting point of the desired mineral phase. For these crystal growth experiments, the temperature of the vacuum oven used was 1100 °C. This temperature is significantly lower than the ~1500 °C melting point of

intermediate composition olivine. Other advantages and some limitations of using a flux growth technique are further described in this section of the dissertation.

1.4. Fluid–mineral interactions in olivine – Parts V and VI

The interaction of olivine with either H_2O or acidic solutions (0.005 M H_2SO_4 or 0.01 M HCl) at low temperature and pressure are examined in the final two parts (V and VI) of this dissertation. Part V examines the interaction of olivine with fluids as a function of pH, surface area of olivine powders, and variation in fluid–mineral ratios of the experiment. Olivine in the presence of low-pH fluids and low temperature and pressure dissolves congruently and results in an increase in pH due to the protonation of vacant octahedral sites (Brantley, 2008; Rimstidt et al., in press). Most dissolution experiments involving olivine are interested in determining dissolution rates, so the pH of the solutions are continuously buffered to a predetermined value of pH. In contrast, the goal of this section of the dissertation was to examine the changes to olivine powders and accompanying solutions as dissolution rate and pH changed with time.

Part VI of this dissertation examines the changes that occur to the surfaces of olivine single crystals in experiments designed to "bridge the gap" from congruent dissolution at low temperature and pressure to incongruent alteration at moderate temperature and pressure. Most studies of olivine dissolution at low temperature and pressure focus on changes to solution and are not designed to determine changes to olivine surfaces (Brantley, 2008; Rimstidt et al., in press). With the use of several nanometer scale analytical techniques (profilometry, X-ray photoelectron spectroscopy, scanning electron microscopy, and secondary ion mass spectrometry), we perform

detailed examination of olivine surfaces after experiments that used a range of temperature, pressure, fluid–mineral ratio, and starting solution conditions.

References Cited

Alt, J. C. (1995) Subseafloor processes in mid-ocen ridge hydrothermal systems. In: Humphris, S. E., Zierenberg, R. A., Mullineaux, L. S., and Thompson, R. E. Eds., *Geophysical Monograph 91 Seafloor Hydrothermal Systems: Physical, Chemical, Biological, and Geological Interactions*. American Geophysical Union, Washington, DC.

Brantley, S. (2008) Kinetics of mineral dissolution. In: Brantley, S., Kubicki, J. D., and White, A. F. Eds.*The Kinetics of Water-Rock Interactions*. Springer, New York.

Chester, R. (2003) *Marine geochemistry*. Blackwell Pub.

DeAngelis, M. T., Labotka, T. C., Cole, D. R., Fayek, M., and Anovitz, L. M. (2007) Experimental investigation of the breakdown of dolomite in rock cores at 100 MPa, 650-750 degrees C. *American Mineralogist* **92**, 510-517.

Drake, M. J. and Righter, K. (2002) Determining the composition of the Earth. *Nature* **416**, 39-44.

Hazen, R. M., Papineau, D., Leeker, W. B., Downs, R. T., Ferry, J. M., McCoy, T. J., Sverjensky, D. A., and Yang, H. X. (2008) Mineral evolution. *American Mineralogist* **93**, 1693-1720.

Labotka, T. C., Cole, D. R., Fayek, M., and Anovitz, L. M. (2006) An experimental study of the serpentine cycle: The hydration of dunite. *EOS Trans. AGU* **87(52)**, Fall Meet. Suppl., Abstract V32B-05.

Morbidelli, A., Chambers, J., Lunine, J. I., Petit, J. M., Robert, F., Valsecchi, G. B., and Cyr, K. E. (2000) Source regions and timescales for the delivery of water to the Earth. *Meteoritics & Planetary Science* **35**, 1309-1320.

Nabelek, P. I., Labotka, T. C., Oneil, J. R., and Papike, J. J. (1984) Contrasting fluid rock intereaction between the Notch Peak granitic intrusion and argillites and limestones in western Utah - evidence from stable istopes and phase assemblages. *Contributions to Mineralogy and Petrology* **86**, 25-34.

Park, D. G., Burlitch, J. M., Geray, R. F., Dieckmann, R., Barber, D. B., and Pollock, C. R. (1993) Sol-Gel Synthesis of Chromium-Doped Forsterite. *Chemistry of Materials* **5**, 518-524.

Richardson, S. M. and McSween, H. Y. (1989) *Geochemistry: Pathways and processes*. Prentice Hall.

Rimstidt, J. D., Brantley, S., and Olsen, A. A. (in press) Systematic review of forsterite dissolution rate data. *Geochimica Et Cosmochimica Acta*.

Robert, F. (2001) The Origin of Water on Earth. *Science* **293**, 1056-1058.

Valley, J. W., Peck, W. H., King, E. M., and Wilde, S. A. (2002) A cool early Earth. *Geology* **30**, 351-354.

Part II.
Oxygen Transport and Exchange in Dolomite Rock at 700 °C, 100 MPa

This part is a reformatted version of a paper, by the same name, submitted to American Mineralogist by Michael T. DeAngelis, Theodore C. Labotka, Mostafa Fayek, David R. Cole, and Lawrence M. Anovitz.

DeAngelis, M.T., Labotka, T.C., Fayek, M., Cole, D.R., and Anovitz, L.M. 2011. Oxygen transport and exchange in dolomite rock at 700 °C, 100 MPa. *Submitted*.

Abstract

The transport and exchange of oxygen isotopes in dolomite rock during the reaction dolomite = calcite + periclase + CO_2 was examined experimentally. The starting material was a cylindrical core of Reed Dolomite from southwestern Nevada. The core was reacted with isotopically enriched water having the composition $HD^{18}O_{0.5}{}^{16}O_{0.5}$ at 700 °C and 100 MPa for 29 days. Reaction products formed along grain boundaries, fractures, and the outside of the core, and some dolomite grains became enriched in Fe as a result of dolomite recrystallization. Because ^{18}O was 50% of the oxygen in the fluid and that amount was much greater than the background concentration of ^{18}O in the dolomite, ^{18}O could be used as a tracer of fluid transport and isotopic exchange. Electron probe microanalysis (EPMA) and secondary ion mass spectrometry (SIMS) analyses showed pervasive infiltration of fluid along grain boundaries and fractures, growth and isotopic exchange with products of reaction, and diffusion of ^{18}O into dolomite grains. Ion probe spot analyses of reaction products (e.g. calcite) from both the center and the edge of the core have similar values of $F = {}^{18}O$ counts / ($^{18}O+{}^{16}O$) counts = 0.14 ± 0.1. These values indicate that fluid infiltration was fast along grain boundaries to the sites of reaction and that reaction products record a mix of both dolomite- and fluid-derived oxygen. An estimate of the diffusion coefficient of oxygen in dolomite was determined by comparing ion probe spot analyses with diffusion calculations and was found to be between D =

1×10^{-14} and 5×10^{-12} cm^2/s. This range is comparable to oxygen diffusion coefficients for calcite exchanging with an H_2O-rich fluid. The amount of uptake of ^{18}O in the dolomite was also calculated and was found to have a value of $F = 0.009$. Spot analyses of the Fe-rich, recrystallized dolomite near the core edge had an average value of $F = 0.02 \pm 0.002$; nearly 10 times the value of $F \approx 0.002$ for unreacted dolomite. These results show that not only do the neomorphic phases record a mix of both dolomite- and fluid-derived oxygen, but that there is also extensive exchange between the extant dolomite and fluid by both recrystallization and diffusion.

1. Introduction

Oxygen isotopes are useful tracers of fluid transport and exchange in contact metamorphic aureoles because there can be significant isotopic contrast between magmatic fluids associated with an intruding pluton and the minerals and fluids in the host rock (Cook and Bowman 1992; Ferry 1991; Moore and Kerrick 1976; Nabelek et al. 1984, Nabelek 1991; Roselle et al. 1999; Valley et al. 1986; Valley 2001). The rates of isotope exchange can be relatively fast in some contact metamorphic environments (e.g. Bowman et al. 2008), but vary depending on the mechanisms for exchange. Exchange mechanisms in contact metamorphic aureoles can include: neomorphic exchange (i.e. isotope exchange during the reactive growth of new minerals), recrystallization, and diffusive exchange. It is likely that no single mechanism is totally responsible for the redistribution of oxygen isotopes in rock-water systems far from equilibrium. Therefore, all possible mechanistic pathways should be considered to fully describe exchange (e.g. Souza and Labotka 2011).

We performed a dolomite rock core experiment (MR6) using environmental conditions similar to those found in natural contact metamorphic environments. DeAngelis et al. (2007) determined rates and mechanisms of mineral reaction for this experiment, so the purpose here is to examine the exchange of oxygen isotopes between the fluid, dolomite, and reaction products. Experiment MR6 was selected because it contains both reaction-rich and reaction-free zones; some dolomite grains adjacent to reaction zones are recrystallized, while other dolomite grains around these zones are unchanged. The presence of these different zones within one sample has allowed us to examine the impact of all three of the exchange mechanisms described above. We find

that oxygen in neomorphic crystals is both dolomite- and fluid-derived, that recrystallization resulted in ^{18}O-enriched dolomite, and that diffusive exchange occurred in dolomite adjacent to both reactive and non-reactive grain boundaries.

2. Methods

2.1. Experimental techniques

The experiment was conducted using the Late Proterozoic Reed Dolomite from Nevada as starting material. The Reed Dolomite is a massive, brown to tan, medium- to coarse-grained dolomitic marble (Richards et al. 1996). The grain size ranges from 0.5 to 1.0 mm in diameter, and the grains are anhedral in shape. This sample also contains minor quartz veins, trace pyrite, and intergranular fractures. Average $\delta^{18}O$ values of the Reed Dolomite ranges from 11.1‰ to 21.5‰ (SMOW) (Richards et al. 1996).

A small core, approximately 4 mm in diameter and 6 mm in length, was drilled from the marble sample. The core was placed in a thin-walled, 5 mm gold capsule, approximately 7.5 cm in length. An aliquot of $HD^{18}O_{0.5}{}^{16}O_{0.5}$ was added to the sample (see Table II-2), and the capsule was purged with CO_2 gas and arc-welded closed. The prepared capsule was placed in a vacuum oven for approximately 24 hours and then reweighed to ensure that there were no leaks. The capsule was then placed in a cold-seal hydrothermal apparatus at 700°C and 100 MPa for 29 days. The experiment was heated to the desired temperature over a period of thirty to forty minutes. During the course of the experiment, both pressure and temperature were monitored and recorded. The experiment was isobarically quenched to ambient temperature over a period of twenty

minutes. The capsule was then removed from the hydrothermal apparatus, weighed to test for leakage, and punctured under vacuum. Any water present was cryogenically captured, and any reaction produced CO_2 was measured by manometry. The dolomite core was then removed from the gold capsule, embedded in epoxy, and sectioned longitudinally.

2.2. Analytical techniques

Reaction products, reaction textures, and extent of reaction were determined by petrography and EPMA. Back-scattered electron (BSE) and Ca, Mg, Si, and Fe Kα X-ray images were collected with the Cameca SX-100 at the University of Tennessee. For these analyses, the microprobe had an accelerating voltage potential of 15 kV, a beam current of 4 nA, and a beam size of 1 μm. Images were generated by rastering the sample stage over a 512 x 512 μm area using a 2 μm step and a counting time of 1 ms per step. Quantitative mineral analyses were also collected, and for these analyses the microprobe had an accelerating voltage potential of 15 kV, a beam current of 6 nA, a beam size of 1 μm, and a counting time of 40 seconds for most elements. Natural standards of calcite, dolomite, and periclase were used for calibration.

Oxygen isotope distributions were obtained by ion imaging and isotope ratio analysis using the CAMECA ims 7f SIMS located in the Manitoba Regional Materials and Surface Characterization Facility at the University of Manitoba, Canada. The sample was prepared by applying a thin gold coat (~15 seconds of sputtering time) to a thin section mount. Oxygen isotope (^{18}O and ^{16}O) ion images were generated by rastering over a 250 x 250 μm area using a 150 pA Cs^+ primary beam and a 200 V high voltage energy offset. Oxygen isotope ratio spot analyses of the sample, dolomite standards (MD Dolomite: $\delta^{18}O_{SMOW}$ = 21.9‰; Brumado Dolomite: $\delta^{18}O_{SMOW}$ = 14.0‰), and a calcite

standard (Joplin Calcite: $\delta^{18}O_{SMOW}$ = 5.8‰) were measured using a 300 pA Cs^+ primary beam and 200 volt energy offset. This primary beam current was selected to keep the spot size small (≤10 μm); however, a minimum pre-sputtering period of 30 seconds was required to obtain a stable count rate (~$1.5x10^5$ counts on ^{16}O) before collecting oxygen isotope ratio spot analyses.

To compare mineral composition in reaction zones with areas of isotope transport and exchange, X-ray and ion images were co-registered with use of the program ENVI by selecting corresponding control points and resizing the ion image to match X-ray image dimensions.

3. Results

3.1. Reaction products and textures

Areas of reaction are present throughout sample MR6 (Figure II-1), and the total fractional extent of reaction for sample MR6 has been previously determined by EPMA point counting to be 0.19 (see Table 3 in DeAngelis et al. 2007). The most extensive reaction occurred in the fluid-accessible areas near the edges of the core; however, limited reaction is also present toward the interior of the core where fluid was localized along grain boundaries and fractures. A thin quartz vein is present through the center of the core, and some additional reaction occurred in and around this vein. Primary products of reaction are calcite and periclase, with minor amounts of other Mg-carbonates (e.g. nesquehonite [$MgCO_3 \cdot 3H_2O$] as an exterior quench phase) and some Mg-silicates (e.g.

forsterite adjacent to the quartz vein). The two areas selected for detailed analysis of ^{18}O and ^{16}O distributions are shown in Figure II-1.

3.1.1. X-ray imaging

The area displayed in Figure II-2 was selected because it has unreacted dolomite grains adjacent to both grain boundary reaction and reaction-free zones. The X-ray images in Figure II-2a show the typical mottled appearance of a grain boundary reaction zone, with small (10-20 μm), anhedral calcite grains interspersed with void space immediately adjacent to dolomite grains, and periclase located primarily along channels at the remnant original grain boundary. The location and small grain size of the periclase suggests that most magnesium remained in solution until quench of the experiment.

The area displayed in Figure II-3 has newly formed minerals and unreacted dolomite similar to Figure II-2, with similar mottled reaction zones along grain boundaries and fractures that contain a mixture of interspersed calcite, hydrated magnesium carbonate, and minor Mg-silicates. The area in Figure II-3 also contains some zones within dolomite that are enriched in Fe relative to the original, unreacted dolomite. These areas of Fe enrichment are interpreted to represent dolomite recrystallization and not diffusion of Fe into the dolomite, because the concentration of Fe is uniform throughout these zones and there is a sharp boundary between the Fe-rich zone and original dolomite. Minor amounts of pyrite (<1%) are the only possible source for Fe in this dolomite core, and some pyrite is observed in the quartz vein adjacent to the recrystallized dolomite.

3.2. Isotope transport and exchange

The average $\delta^{18}O$ values of the Reed Dolomite range from 11.1‰ to 21.5‰ (Richards et al. 1996), therefore, the amount of ^{18}O in the starting $HD^{18}O_{0.5}{}^{16}O_{0.5}$ water (50%) far exceeds the amount of ^{18}O in the original dolomite marble. Any significant increase in the ^{18}O at any location within the experiment cores, therefore, resulted from exchange with the fluid. Because the measured concentrations of ^{18}O span a large range, isotope ratio values reported here use the *F* notation [$F = {}^{18}O$ counts / ($^{18}O+{}^{16}O$) counts] instead of the more traditional $\delta^{18}O$ notation. The *F* value range of the Reed Dolomite for the $\delta^{18}O$ values above is $F = 0.00201$ to 0.00204.

3.2.1. Oxygen imaging

Qualitative oxygen isotope ion images can be useful to observe ^{18}O distribution (e.g. Labotka et al. 2007), and have been generated in select zones within Figures II-2a and II-3a (Figures II-2b and II-3b). The dimensions of the ion images are smaller than the dimensions for X-ray and BSE images, so only a portion of the BSE images in Figures II-2b and II-3b are overlain by ion images.

The oxygen isotope ion image overlay in Figure II-2b shows the distribution of ^{18}O along a portion of a grain boundary reaction zone near the center of sample MR6. The background BSE image in Figure II-2b shows an area of transition from abundant reaction products along grain boundaries in the upper left and middle that thins to an area free of reaction products along a grain boundary to the lower right. The purple-colored areas of the overlain ion image are concomitant with the location of reaction products in the BSE image, showing that reaction products have a significant increase in ^{18}O and that these neomorphic minerals exchanged with the isotopically enriched fluid during growth.

Areas of ^{18}O enrichment also appear along the grain boundary in the reaction-free zone to the lower right, indicating grain boundary diffusion of an ^{18}O-rich fluid despite the lack of reaction products. The orange-colored areas of the overlain ion image also indicate elevated values of ^{18}O extending into the dolomite grains adjacent to the grain boundary zone. Because there is no chemical evidence for recrystallization (i.e. Fe enrichment) of the dolomite immediately adjacent to the grain boundary reaction zones in Figure II-2b, the increase in ^{18}O values is interpreted as resulting from diffusive exchange into unreacted dolomite. Similar to Figure II-2b, the ion image overlay in Figure II-3b also has significant ^{18}O enrichment in the reaction products, but also shows greater enrichment extending into dolomite grains near the outer edge of the core.

Because ^{18}O is much more concentrated in the reaction products compared to areas lacking significant exchange (e.g. the centers of most dolomite grains), there is a lower threshold of ^{18}O concentration ($F \approx 0.10$) that can be displayed in these ion images. For more detailed resolution, spot analyses were performed to quantify ^{18}O concentrations.

3.2.2. Oxygen spot analyses

Detailed oxygen isotope spot analyses were performed on reaction products, unreacted dolomite, and recrystallized dolomite (Table II-1). Isotopic spot analyses of the calcite in the Figure II-2 grain boundary reaction zone (cc1-2) have an average value of $F = 0.14$ (n=2), and calcite grains within the Figure II-3 grain boundary reaction zone (cc3-5) have a similar average value of $F = 0.15$ (n=3). The average value for all spots measured on calcite, used to represent the value of all reaction products, is $F = 0.14 \pm 0.1$

(n=5). The periclase in both reaction areas is too small to analyze by SIMS spot analysis, but is presumed to have oxygen values that are similar to those measured in calcite.

Three oxygen isotope spot analysis traverses (A, B, C) were collected in the dolomite grain immediately below the grain boundary reaction zone in Figure II-2b (Figure II-2c). Each traverse started approximately 1–5 μm inside the grain boundary edge of the dolomite and each spot was collected in 20 μm steps advancing toward the dolomite grain center. These traverses exhibit increased *F* values in the dolomite near the grain boundary that decrease toward the grain core. There are also lateral differences between these traverses, with Traverse B, which originates adjacent to the most highly reacted zone, showing slightly increased *F* values over Traverse C, the traverse adjacent to the reaction-free zone.

Four oxygen-isotope spot analysis traverses (D, E, F, G) were also performed through a dolomite grain in the Figure II-3b area near the edge of the dolomite core (Figure II-3c). Traverse D contains three spots beginning at a grain boundary and traversing toward the center of the unreacted portion of the dolomite grain. The rim value of this traverse is elevated adjacent to the grain boundary ($F = 0.049$), but quickly drops to the unreacted value for the dolomite grains ($F \approx 0.002$). Traverse E also contains three spots analyzed in the recrystallized portion of the dolomite. These analyses show an average enrichment of $F = 0.02 \pm 0.002$ (n=3); more than 10 times the unreacted value of ^{18}O for the dolomite. Spots along two additional traverses (F, G) were analyzed from the reaction zone on the right side of dolomite grain through the recrystallized and non-recrystallized portions of the dolomite grain and ending near the grain boundary on the left side of the grain. Similar to spots in traverses D and E, these

traverses have elevated values for the spots analyzed in the recrystallized region, background values for the unreacted areas, and greatly enriched values for the analyses immediately adjacent to reaction products near the edges of the dolomite grain.

4. Discussion

4.1. Oxygen isotope mass balance from extent of reaction

The measured *F* values from reaction products are similar from different areas within the dolomite core, suggesting that the final fluid was well mixed and that the reaction products were continuously exchanging with the fluid during growth. Since this was a closed system experiment in which the total amount of oxygen must be conserved among all the phases, the known values of *F* from the initial fluid ($F = 0.5$) and reaction products ($F = 0.14$) along with the estimated fractional extent of reaction for sample MR6 (0.19) were used to calculate the oxygen isotope mass balance and to estimate the final fractions of oxygen isotopes in all phases (Table II-2).

If the final *F* value for the fluid was the same as the value measured in the neomorphic crystals (i.e. $F = 0.14$), these estimates suggest that slightly more than half (0.48 mmol) of the ^{18}O originally concentrated in the fluid has exchanged with the dolomite by the end of the experiment. Dividing this amount of ^{18}O in the dolomite by the total number of moles of oxygen in the remaining dolomite after experiment (6.27 mmol) results in an estimated $F = 0.08$ for the total uptake of ^{18}O in all dolomite. This means that the value of *F* measured at any location within any dolomite grain in sample MR6 should be 0.08 if there were an even distribution of ^{18}O after uptake. As previously shown in Figures 2c and 3c, however, the actual measured values from oxygen isotope

spot analyses within the dolomite vary considerably, and indicate diffusive exchange with the fluid during the experiment.

4.2. Diffusive exchange in unreacted dolomite

The oxygen isotope spot analyses in Traverses A–C from Figure II-2b were performed to examine the diffusive distribution of ^{18}O along the edge of unreacted dolomite. These data were plotted along with diffusion profiles that were calculated using the solution for diffusion in a sphere (i.e. a single dolomite grain) from a well-stirred solution of limited volume (modified from equation 6.36 in Crank, 1975):

$$F_t(r) = F_\infty\left[1 + \sum_{n=1}^{\infty} \frac{6(1+\alpha)\exp(-Dq_n^2 t/a^2)}{9 + 9\alpha + q_n^2\alpha^2} \frac{a}{r} \frac{\sin(q_n r/a)}{\sin q_n}\right] + F_0 \quad (1)$$

where $F_t(r)$ is the F value at the end of the experiment and a diffusive radius of interest, F_∞ is the F value for the whole system at infinite time, F_0 is the F value of unreacted dolomite, D is the oxygen diffusion coefficient, a is the radius of a dolomite grain, r is the diffusive radius of interest, α is the ratio of the moles of O in the fluid and solid at the end of the experiment, and t is the duration of the experiment (Figure II-4; Table II-3). The values for q_n were calculated by finding the positive, non-zero roots of the following expression (equation 6.31 in Crank, 1975):

$$\tan q_n = \frac{3q_n}{3 + \alpha q_n^2} \quad (2)$$

A consideration in the use of these diffusion equations is that the dolomite grain does not maintain a constant radius, a, adjacent to a grain boundary reaction zone throughout the experiment. While this is not an issue for the Traverse A and Traverse C data collected adjacent to unreacted dolomite, the Traverse B data is adjacent to a grain

boundary reaction zone in which the unreacted dolomite grain edge has moved slightly inward (~40 μm) because of reaction. We have elected to plot all data in Figure II-4 relative to the current grain edge and have not attempted to adjust their location relative to any presumed original grain boundary.

Four diffusion profiles were calculated for values of D between 10^{-11} and 10^{-14} cm^2/s (Figure II-4). The measured data from Traverses A–C are also plotted in Figure II-4, and show that the diffusion coefficient for oxygen in the dolomite falls within a range between $D = 1.0\times10^{-14}$ and 5.0×10^{-12} cm^2/s. The error bars on these data reflect the ≤10 μm diameter size of ion analysis spots. This determined range of D is comparable to values determined for oxygen diffusion in other carbonate diffusion experiments (Anderson 1972; Labotka et al. 2011). Labotka et al. (2011) reports log D between -13 and -14 for oxygen diffusion in calcite exchanging with an H_2O-rich fluid at the same pressure and temperature conditions (700 °C, 100 MPa) as the MR6 experiment.

The calculated diffusion coefficients can also be used to compute the uptake of ^{18}O in dolomite during diffusion for comparison with the value determined by mass balance. We used the uptake equation for diffusion in a sphere from a well-stirred solution of limited volume (modified from Eq. 6.30 in Crank, 1975):

$$F_{\text{total}} = F_{\infty}\left[1 - \sum_{n=1}^{\infty} \frac{6\alpha(\alpha+1)\exp(-Dq_n^2 t/a^2)}{9 + 9\alpha + q_n^2\alpha^2}\right] \quad (3)$$

where F_{total} is the calculated uptake of ^{18}O in the dolomite grain at the end of the experiment, and F_{∞} is the F value for the whole system at infinite time. For an approximate average oxygen diffusion coefficient value of $D = 5.0\times10^{-14}$ cm^2/s for the Traverse A–C data, this calculation results in a total uptake value of $F_{\text{total}} = 0.009$. This

value is nearly one-tenth the value of $F = 0.08$ calculated by mass balance, indicating that the assumption of equilibrium between the fluid and reaction products made in the mass balance calculation cannot be correct. Using the mass balance uptake value of $F = 0.08$ to solve equation (1) results in a $D \approx 2.0\times10^{-11}$ cm^2/s. This value of D is two to three orders of magnitude greater than the measured values from Traverses A–C, affirming an isotopic disequilibrium between the neomorphic minerals and the fluid.

Recalculation of the mass balance using the original fractional extent of reaction of 0.19 and $F = 0.14$ for calcite and periclase but using the diffusion calculation value for total uptake of $F_{total} = 0.009$ yields a value for the final experimental fluid of $F = 0.32$. Even if the determined fractional extent of reaction was incorrect by as much as ± 50% the original 0.19 estimate, the mass balance recalculation would yield a final experimental fluid F range (F = 0.22–0.38) significantly higher than the value of the reaction products. In addition, the F value calculated from equation (1) at the sphere edge (i.e. $a = r$) can also provide an estimate of the final fluid F value, since the edge of the sphere should be close to equilibrium with the fluid. Using the average $D = 5.0\times10^{-14}$ cm^2/s determined for Traverses A–C indicates a sphere edge value of $F = 0.37$, a value similar to the final experimental fluid value determined by the mass balance recalculation.

The implication of these calculations is that the periclase and calcite did not crystallize in equilibrium with the fluid; the lower F value of these minerals must reflect a mixing of oxygen derived from both the fluid and the dolomite. Given that the breakdown of dolomite must result in release of dolomite-derived oxygen, it seems

reasonable that a portion of the oxygen in the reaction products should have an *F* value reflective of, in part, the original dolomite.

4.3. Oxygen isotope distribution in recrystallized dolomite

The oxygen isotope spot analyses in Traverses D–G (see Figure II-3c) were collected to examine the distribution of ^{18}O in an area containing recrystallized dolomite near the edge of the core. Traverse D was collected in the unreacted portion of this dolomite grain and has a diffusive exchange profile comparable with Traverses A–C. Despite being adjacent to areas of dolomite recrystallization, the values measured here are similar to the values measured for the other traverses in unreacted dolomite near the center of the core. Spots 4-6 in Traverse F and spots 4-6 in Traverse G are both through unreacted dolomite and also have similar *F* exchange profiles.

The oxygen isotope spot analyses collected in the recrystallized portions of the dolomite (Traverse E) are elevated over the values measured in the adjacent original dolomite and show a large step from the average recrystallized dolomite value of $F = 0.02 \pm 0.002$ (n=3) to the value of *F* for the unreacted dolomite ($F \approx 0.002$). This isotopic step is concomitant with the sharp boundary observed in X-ray images between the Fe-rich, recrystallized dolomite and original dolomite. Though there may be a slight decreasing *F* trend from rim to core in Traverse E, these data remain elevated throughout the recrystallized portion of this dolomite. These elevated *F* values, and the step to much smaller *F* values after crossing the boundary between the recrystallized and original dolomite, suggest that exchange in this zone is primarily coupled with recrystallization and that diffusive exchange here is only a minor process.

4.4. Implications for natural settings

This experiment was performed at conditions far from equilibrium to promote reaction and isotopic exchange over the relatively short duration of the experiment. While the duration of the experiment may be short compared with the amount of time available for reaction and exchange in a natural contact metamorphic aureole, the initial isotopic disequilibrium of this experiment reflects the far-from-equilibrium condition that prevail at the onset of reaction in some natural settings. During the initial stages of fluid infiltration into a new rock matrix, fluids are confined to grain boundaries and fractures and can have ^{18}O concentrations greatly different from the surrounding dolomite.

Measurements of F in the reaction products of this experiment have similar values despite coming from different areas of the rock core. These values indicate that fluid infiltration along grain boundaries was extremely fast and reflect a similar process of isotope mixing of dolomite-derived and fluid-derived oxygen despite having occurred in different parts of the core. Mass balance and diffusion calculations indicate that ^{18}O was not in equilibrium between the fluid and neomorphic crystals.

These measurements and calculations also show that ^{18}O exchanged with the dolomite and that the amount of exchange is not insignificant. Measurable diffusion coefficients are not as easily attainable from country rock in natural contact metamorphic environments because the amount of time available for exchange in those environments is generally much longer and the concentration differences in ^{18}O between the fluid and country rock are smaller. Given the long periods of time during which pluton emplacement, fluid infiltration, and isotopic exchange occur in contact metamorphic aureoles, the cumulative contribution of isotopic exchange with the host dolomite and

neomorphic minerals may be relevant to modeling of overall fluid transport and isotope distributions.

Acknowledgments

This manuscript is a portion of M.T. DeAngelis's dissertation work at the University of Tennessee, Knoxville. Many thanks to Allan Patchen at the University of Tennessee for help with EPMA analyses, and to Sharon Hull, Brandi Shabaga and Rong Liu at the University of Manitoba for help with SIMS analyses. Funding for this work was provided by the National Science Foundation grant EAR-0087553 and the Division of Chemical Sciences, Geosciences, and Biosciences, Office of Basic Energy Sciences, U.S. Department of Energy. Oak Ridge National Laboratory is managed and operated by UT-Battelle for the U.S. Department of Energy under contract DE-AC05-00OR22725.

References Cited

Anderson, T.F. (1972) Self-diffusion of Carbon and Oxygen in Dolomite. *Journal of Geophysical Research*, **77**(5), 857-861.

Bowman, J.R., Valley, J.W., Kita, N.T. (2008) Mechanisms of oxygen isotopic exchange and isotopic evolution of $^{18}O/^{16}O$-depleted periclase zone marbles in the Alta aureole, Utah: insights from ion microprobe analysis of calcite. *Contributions to Mineralogy and Petrology*, **157**(1), 77-93.

Cook, S.J. and Bowman, J.R. (1992) Contact metamorphism surrounding the Alta stock: thermal constraints and evidence of advective heat transport from calcite-dolomite geothermometry. *American Mineralogist*, **79**, 513-525

Crank, J. (1975) The mathematics of diffusion, 414 p. Clarendon Press, Oxford.

DeAngelis, M.T., Labotka, T.C., Cole, D.R., Fayek, M., Anovitz, L.M. (2007) Experimental investigation of the breakdown of dolomite in rock cores at 100 MPa, 650-750 °C. *American Mineralogist*, **92**(4), 510-517

Ferry, J.M. (1991) Dehydration and decarbonation reactions as a record of fluid infiltration. In D.M. Kerrick, Ed., Contact Metamorphism, 26, 351-391. Reviews in Mineralogy, Mineralogical Society of America, Washington, DC.

Labotka, T.C., Cole, D.R., Fayek, M.J., Chacko, T. (2011) An experimental study of the diffusion of C and O in calcite in mixed CO_2-H_2O fluid. *American Mineralogist*, in press.

Labotka, T.C., DeAngelis, M.T., Cole, D.R., Fayek, M., Riciputi, L.R., Ushikubo, T., Kita, N.T., Valley, J.W. (2007) O isotope exchange during the breakdown of dolomite: An experimental study. *Geochimica et Cosmochimica Acta Supplement*,

71(15), Supplement 1, Goldschmidt Conference Abstracts 2007, A534.

Moore, J.N. and Kerrick, D.M. (1976) Equilibria in siliceous dolomites of the Alta aureole, Utah. *American Journal of Science*, **276**, 502-524

Nabelek, P.I. (1991) Stable Isotope Monitors, In D.M. Kerrick, Ed., Contact Metamorphism, 26, 395-435. Reviews in Mineralogy, Mineralogical Society of America, Washington, DC.

Nabelek, P.I., Labotka, T.C., O'Neil, J.R., and Papike, J.J. (1984) Contrasting fluid/rock interaction between the Notch Peak granitic intrusion and argillites and limestones in western Utah: Evidence from stable isotopes and phase assemblages. *Contributions to Mineralogy and Petrology*, **86**, 25-34.

Richards, I.J., Labotka, T.C., and Gregory, R.T. (1996) Contrasting stable isotope behavior between calcite and dolomite marbles, Lone Mountain, Nevada. *Contributions to Mineralogy and Petrology*, **123**, 202-221.

Roselle, G.T., Baumgartner, L.P., Valley, J.W. (1999) Stable isotope evidence of heterogeneous fluid infiltration at the Ubehebe Peak contact aureole, Death Valley National Park, California. *American Journal of Science*, **299**, 93-138.

Souza, P. and Labotka, T.C (2011) Coupled mineral reaction and isotope exchange in regionally metamorphosed dolomite, Death Valley, California. *Contributions to Mineralogy and Petrology*, in press.

Valley, J.W. (1986) Stable isotope geochemistry of metamorphic rocks. In J.W. Valley, H.P. Taylor, J.R. O'Neil, Eds., Stable isotopes in high temperature geological processes, 16, 445-490. Reviews in Mineralogy, Mineralogical Society of America, Washington, DC.

Valley, J.W. (2001) Stable isotope thermometry at high temperatures: In: J.W. Valley, D.R. Cole Eds., Stable isotope geochemistry., 43, 365-414. Reviews in Mineralogy and Geochemistry, Mineralogical Society of America, Washington, DC.

Appendix II

Table II-1. Sample MR6 oxygen isotope spot analyses

Spot Name	Mineral Type	Location	Average ^{16}O counts	Average ^{18}O counts	*F*
cc1	reaction-produced calcite	Figure 2 - Reaction zone	27372	5048	0.1557
cc2	reaction-produced calcite	Figure 2 - Reaction zone	34736	5061	0.1272
cc3	reaction-produced calcite	Figure 3 - Reaction zone	31536	5779	0.1549
cc4	reaction-produced calcite	Figure 3 - Reaction zone	36372	6623	0.1540
cc5	reaction-produced calcite	Figure 3 - Reaction zone	35094	5258	0.1303
A1	unreacted dolomite	Figure 2 - Traverse A - grain rim	221477	917	0.0041
A2	unreacted dolomite	Figure 2 - Traverse A	227659	546	0.0024
A3	unreacted dolomite	Figure 2 - Traverse A	229025	453	0.0020
A4	unreacted dolomite	Figure 2 - Traverse A	53180	103	0.0019
A5	unreacted dolomite	Figure 2 - Traverse A	50775	99	0.0019
B1	unreacted dolomite + reaction products	Figure 2 - Traverse B - grain rim	47335	7733	0.1404
B2	unreacted dolomite	Figure 2 - Traverse B	49181	398	0.0080
B3	unreacted dolomite	Figure 2 - Traverse B	49581	97	0.0020
B4	unreacted dolomite	Figure 2 - Traverse B	49224	92	0.0019
C1	unreacted dolomite	Figure 2 - Traverse C - grain rim	86361	1361	0.0155
C2	unreacted dolomite	Figure 2 - Traverse C	70818	317	0.0045
C3	unreacted dolomite	Figure 2 - Traverse C	61600	151	0.0024
C4	unreacted dolomite	Figure 2 - Traverse C	58521	115	0.0020
D1	unreacted dolomite	Figure 3 - Traverse D - grain rim	205401	10540	0.0488
D2	unreacted dolomite	Figure 3 - Traverse D	224180	462	0.0021
D3	unreacted dolomite	Figure 3 - Traverse D	224670	441	0.0020
E1	recrystallized Fe-rich dolomite	Figure 3 - Traverse E - grain rim	177845	4360	0.0239
E2	recrystallized Fe-rich dolomite	Figure 3 - Traverse E	218095	5033	0.0226
E3	recrystallized Fe-rich dolomite	Figure 3 - Traverse E	222613	4659	0.0205
F1	recrystallized Fe-rich dolomite + reaction products	Figure 3 - Traverse F - graim rim	23550	1680	0.0666
F2	recrystallized Fe-rich dolomite	Figure 3 - Traverse F	44868	150	0.0033
F3	recrystallized Fe-rich dolomite + reaction products	Figure 3 - Traverse F	42925	1669	0.0374
F4	unreacted dolomite	Figure 3 - Traverse F	49407	99	0.0020
F5	unreacted dolomite	Figure 3 - Traverse F	44099	104	0.0023
F6	unreacted dolomite	Figure 3 - Traverse F	39495	2325	0.0556
G1	reaction products	Figure 3 - Traverse G - grain rim	37906	5818	0.1331
G2	recrystallized Fe-rich dolomite	Figure 3 - Traverse G	39580	978	0.0241
G3	recrystallized Fe-rich dolomite	Figure 3 - Traverse G	43578	600	0.0136
G4	unreacted dolomite	Figure 3 - Traverse G	45146	114	0.0025
G5	unreacted dolomite	Figure 3 - Traverse G	41896	358	0.0085
G6	unreacted dolomite + reaction products	Figure 3 - Traverse G	42298	662	0.0154

Table II-2. Oxygen mass balance calculation results*

Phase	Start		Finish	
	^{18}O (mmol)	^{16}O (mmol)	^{18}O (mmol)	^{16}O (mmol)
fluid	0.95	0.95	0.34	2.06
dolomite	0.00	7.74	0.48	5.79
calcite	n.a.	n.a.	0.10	0.63
periclase	n.a.	n.a.	0.03	0.21
totals	0.95	8.69	0.95	8.69

* fractional extent of reaction = 0.19 (see DeAngelis et al., 2007 for details)

Table II-3. Spherical diffusion calculation parameters

Parameter	Description	Value(s)	Units
$F_t(r)$	F value at the end of the experiment and a diffusive radius of interest	varies (see Fig. 4)	-
$^{18}O_\infty$	total moles of ^{18}O in the system at infinite time	0.95	mol
O_∞	total moles of oxygen in the system at infinite time	9.64	mol
F_∞	$^{18}O_\infty$ / O_∞	0.099	-
F_0	F value of unreacted dolomite	0.00194	-
D	oxygen diffusion coefficient	1×10^{-11} – 1×10^{-14}	cm^2/s
a	radius of a dolomite grain	0.05	cm
r	diffusive radius of interest	0.05 – 0.025	cm
O_{fluid}	moles of oxygen in fluid after experiment*	2.39	mol
O_{solid}	moles of oxygen in solids after experiment*	7.25	mol
α	O_{fluid} / O_{solid}	0.33	-
t	duration of the experiment	2505600	s
q_n	positive, non-zero roots of equation 2 (see text)	varies (see text)	-

* based on fractional extent of reaction = 0.19

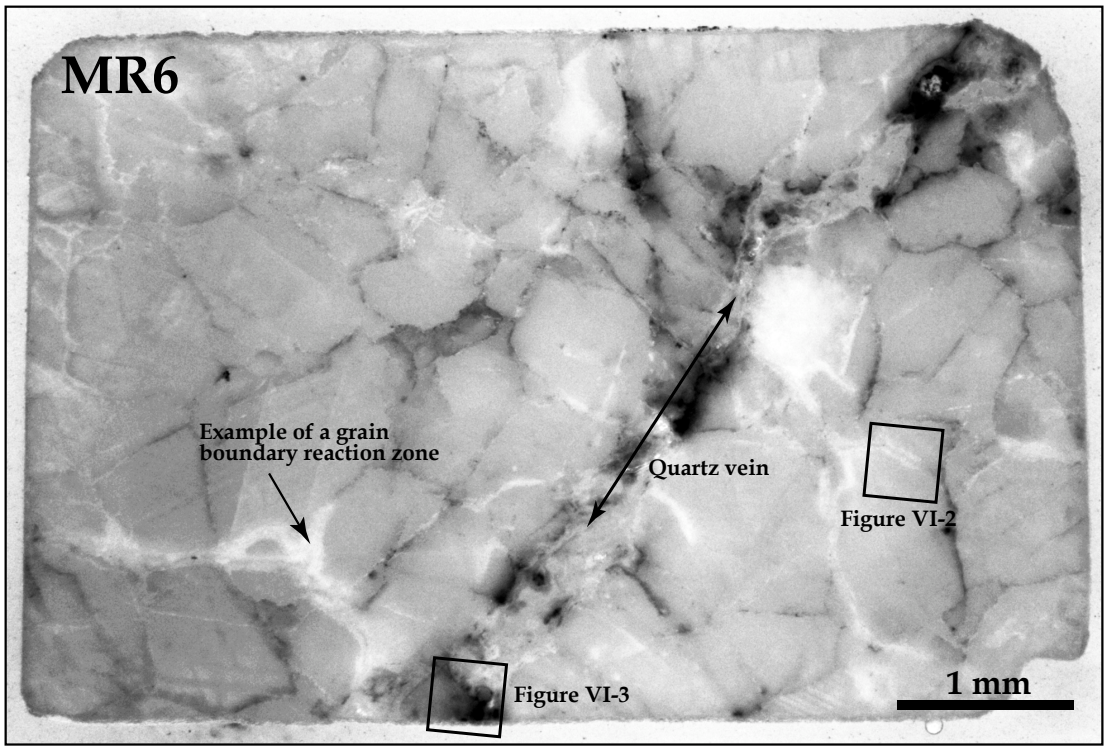

Figure II-1. Photomicrograph of sample MR6. Boxed areas show X-ray and SIMS analysis locations in Figure II-2 and Figure II-3.

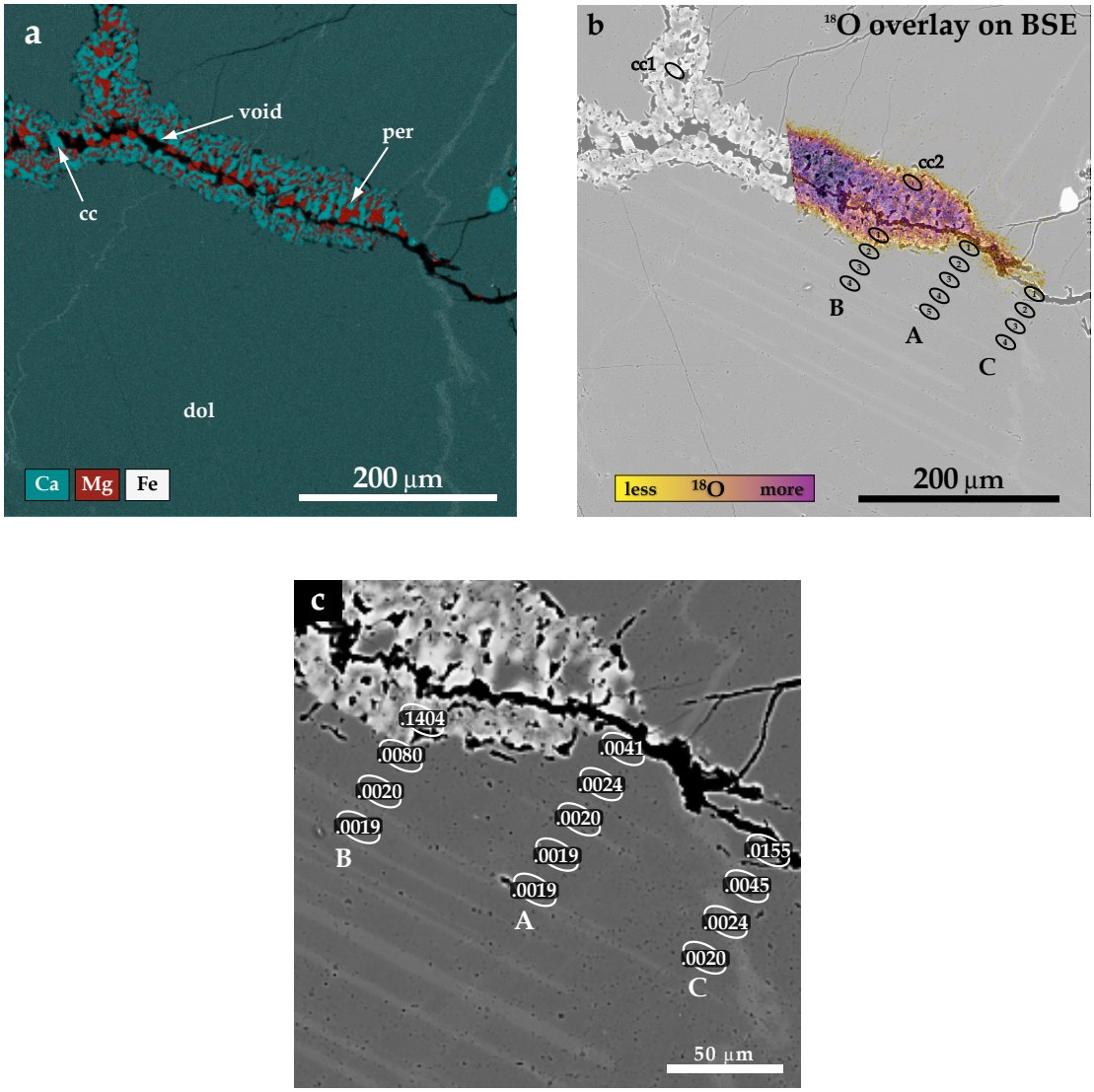

Figure II-2. Images of analysis location near the center of the dolomite core that has unreacted dolomite with adjacent grain boundary reaction and reaction-free zones. (**a**) Composite X-ray image showing the distribution of Ca (aqua), Mg (red), and Fe (light gray) (**b**) ^{18}O ion image overlay on a BSE image showing the qualitative distribution of ^{18}O. The location of ion probe analyses on two calcite grains (cc1, cc2) and dolomite traverses A, B, and C are also labeled (**c**) *F* values of oxygen isotope ratio spots analyzed along traverses A, B, and C.

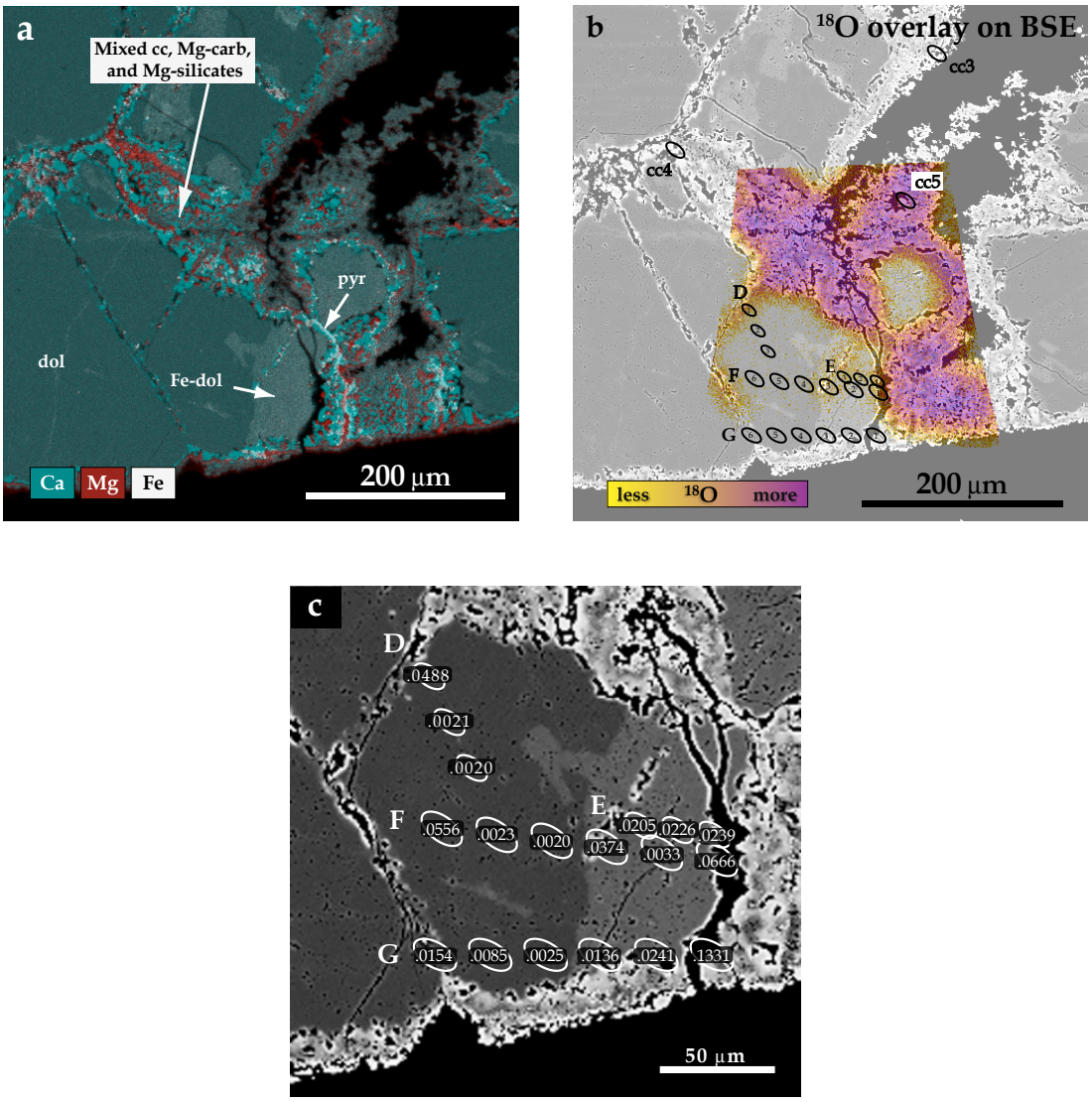

Figure II-3. Images of analysis location near the edge of the dolomite core that has unreacted dolomite, recrystallized dolomite, and abundant reaction products. (**a**) Composite X-ray image showing the distribution of Ca (aqua), Mg (red), and Fe (light gray) (**b**) ^{18}O ion image overlay on a BSE image showing the qualitative distribution of ^{18}O. The locations of ion probe analyses on three calcite grains (cc3, cc4, cc5) and dolomite traverses D, E, F, and G are also labeled (**c**) *F* values of oxygen isotope ratio spots analyzed along traverses D, E, F, and G.

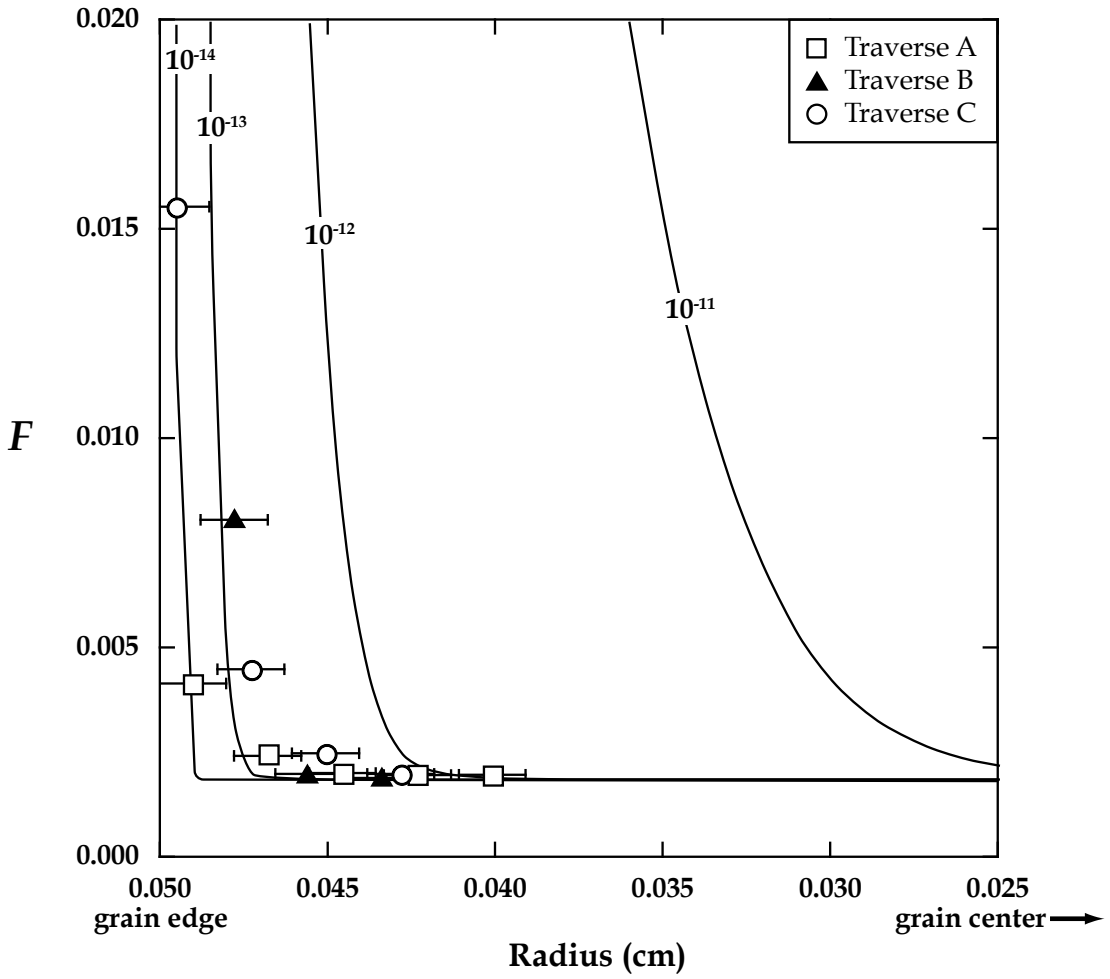

Figure II-4. Four calculated oxygen diffusion profiles in unreacted dolomite for the range $D = 10^{-11}$–10^{-14} cm^2/s determined using the equation for spherical diffusion from a well-stirred solution of limited volume (modified from Crank, 1975). Measured oxygen isotope spot analyses from Traverses A, B, and C in Figure II-2 have also been plotted, and suggest a range in D between 1.0×10^{-14} and 5.0×10^{-12} cm^2/s. The error bars on plotted points represent the ≤10 μm diameter of the ion analysis spot.

Part III.
Sol-gel Synthesis of Nanocrystalline Fayalite (Fe_2SiO_4)

This part is a reformatted version of a paper, by the same name, submitted to American Mineralogist by Michael T. DeAngelis, Adam J. Rondinone, Michelle D. Pawel, Theodore C. Labotka and Lawrence M. Anovitz.

DeAngelis, M.T., Rondinone, A.J., Pawel, M.D., Labotka, T.C., and Anovitz, L.M. Sol-gel synthesis of Nanocrystalline Fayalite (Fe_2SiO_4). 2011. *Submitted.*

Abstract

Fayalite (Fe_2SiO_4), and other Fe-rich olivine, is often found in the reducing environments of the Moon, Mars, and other extraterrestrial bodies, but the oxidation state of the terrestrial mantle restricts the amount of Fe found in olivine on Earth. For this reason, synthetic fayalite is needed for use in planetary-analog and other studies. Here we present a method for the synthesis of nanocrystalline fayalite (nanofayalite) using a sol-gel technique. Iron(II) chloride, sodium ethoxide, and tetraethyl orthosilicate (TEOS) were reacted to produce a precursor gel, which was subsequently calcined under reducing conditions to crystallize nanofayalite. Powder X-ray diffraction analyses indicate that the produced nanofayalite is nearly pure, with minor amounts (0.5–3%) of metallic Fe in some batches. Scanning electron microscope images of nanofayalite crystals show euhedral to subhedral crystals that range in size between 100 and 150 nm. Estimates of specific surface area were determined by both the Brunauer-Emmett-Teller (BET) and Langmuir adsorption methods and indicate average surface areas of 27.7 m^2/g and 45.3 m^2/g, respectively. Regulation of the redox environment was the critical challenge for this synthesis, but careful control of oxygen fugacity during reactant addition and mixing, sol-gel drying, and calcination ensured fayalite crystallization.

1. Introduction

Olivine, $(Mg,Fe)_2SiO_4$, is one of the most prevalent silicate minerals in the solar system. It composes a major portion of the mantle of the Earth and is found on the Moon, Mars, asteroids (e.g. Vesta), and a variety of other extraterrestrial bodies such as meteorites, comets, and interplanetary dust particles (IDPs). There is a complete solid-solution series between the olivine end-members forsterite (Mg_2SiO_4) and fayalite (Fe_2SiO_4), with nearly all naturally occurring olivine containing variable amounts of both iron and magnesium. Most terrestrial mantle-derived olivine has a Mg-rich ($\sim Mg_{1.8}Fe_{0.2}SiO_4$) composition due, in part, to the relatively higher oxygen fugacity (fO_2) in Earth's upper mantle as compared to crystallization environments on the Moon and Mars (Figure III-1). Crystallization of magnetite ($Fe^{2+}Fe^{3+}{}_2O_4$) and quartz (SiO_2) is favored over fayalite in the terrestrial mantle, leading to a scarcity of Fe-rich olivine at the surface of the Earth. The redox environments of the Moon, Mars, and other extraterrestrial bodies are generally more reducing than that of the Earth (Frost, 1991; Herd, 2008; Wadhwa, 2008), so Fe-rich olivine, including pure fayalite, is commonly found in rocks from those places.

Because there is a limited supply of fayalite available on Earth, studies involving fayalite commonly rely on the use of synthesized material (Redfern et al., 2000; Dyar et al., 2009; Hamilton, 2010). For many studies, large crystals (micron size or greater) are acceptable, and so minimal effort has been made to synthesize nanofayalite. However, there is an increasing need for nanocrystalline materials, because various spectroscopic (Hofmeister, 1987; Fabian et al., 2001; Hofmeister and Pitman, 2007; Dyar et al., 2009;

Hamilton, 2010), neutron scattering (Cole et al., 2006; Mamontov et al., 2007), and other studies depends on the use of high surface-area materials.

Presented here is a sol-gel synthesis method for the production of nanofayalite. Several studies have used the sol-gel method for the synthesis of forsterite (Park et al., 1993; Yeager et al., 1993; Wang and Luo, 1994; Douy, 2002; Tsai, 2002; Tsai, 2003; Afonina et al., 2005), but, to our knowledge, this is the first description of sol-gel synthesis for fayalite. Our synthesis method has its basis in the xerogel technique first described by Park et al. (1993) for the synthesis of chromium-doped forsterite. Though the experimental setup for nanofayalite and nanoforsterite syntheses are similar, there are significant differences in the starting chemicals, hydrolyzing reagents, sol-gel processing, and control of fO_2 that are unique to the synthesis of nanofayalite.

2. Experimental Section

2.1. Chemicals

Iron(II) chloride ($FeCl_2$, 99.5% metals basis, Alfa Aesar), sodium ethoxide ($NaOC_2H_5$, 96%, ACROS, stored at 2-5°C), tetraethyl orthosilicate {$Si(OC_2H_5)_4$ [TEOS], 98%, ACROS}, methanol (certified ACS, Fisher), and toluene (HPLC grade, Fisher) were used as received. A sodium hydroxide (NaOH, reagent, ACS) dilute solution was prepared from pellets, manufactured by BDH for VWR. Deionized (DI) water was generated by a Millipore water purification system.

2.2. Synthesis method

The experimental setup began by suspending a 1 L, three-neck flask in a high temperature silicon oil bath placed on a magnetic stirrer/hot plate (Figure III-2). A magnetic stir bar was added to the flask, and a large paper clip was used to continuously stir the silicon oil bath. The right port of the flask was sealed with a rubber septum, which was removed as needed to add solvents, reactants, and hydrolyzing reagents. A condenser was connected to the center port of the flask, sealed at the top with a septum, and a re-circulating cooling bath was attached to the condenser. A tube was connected from a gas/vacuum manifold to a stopcock in the left neck of the flask so that the assembly could be repeatedly evacuated and purged with argon. After drying out the assembly completely, argon continuously flowed through the flask assembly for the duration of the synthesis. A syringe needle was pushed through the center septum to vent excess argon.

Fayalite synthesis began by adding 375 mL of toluene and 175 mL of methanol to the flask. To remove any dissolved oxygen, the solvents refluxed (hotplate at 250 °C, condenser at 10 °C) for about 30 minutes. After removing the dissolved oxygen and cooling the solvents, the reactants were added to the flask. The ferrous iron component needed for the synthesis was obtained by reacting sodium ethoxide with iron(II) chloride to produce sodium chloride and iron(II) ethoxide by the following reaction (Caillot et al., 2002):

$$2\ NaOC_2H_5 + Fe^{2+}Cl_2 \rightarrow 2\ NaCl + Fe^{2+}(OC_2H_5)_2$$

The order of addition for reactants was 8.7 g of iron(II) chloride followed by 9.3 g of sodium ethoxide, which yielded ~10 g of iron(II) ethoxide in solution. The sodium ethoxide rapidly reacted with the iron(II) chloride, and the solution color changed from a

nearly-translucent light tan after addition of the iron(II) chloride to an opaque, grayish-green color after addition of the sodium ethoxide. Next, the hotplate was set to 150 °C and condenser to 10 °C, and 7.9 g of TEOS was added during heating. After the solution continuously refluxed for ~20-30 minutes, ~10 mL of 0.2 M NaOH was slowly dripped into the solution with a syringe to hydrolyze the iron(II) ethoxide and TEOS. The solution was then left to reflux for at least 12 hours (generally overnight). After 12 hours, the heat was turned off and the solution was cooled.

Since the formation of fayalite is redox sensitive, several steps were taken to maintain reducing conditions during synthesis and calcination. Argon was continuously pumped through the flask throughout the additions, mixing, and the reflux period. Once cooled, the solution was transferred to a rotary evaporator to remove solvents and to dry the gel. The rotary evaporator was determined to be the fastest and best method of solvent removal and drying, because other attempts at drying the gel in a vacuum oven resulted in some oxidation and the production of magnetite. The dried gel powder was calcined in a tube furnace under flowing N_2 gas for 4 hours (2 h ramp, 2 h hold) at 800 °C. After calcination, the nanofayalite crystals were rinsed and spun in a centrifuge repeatedly with hot (~80 °C), deionized H_2O to remove NaCl. The post-calcine rinse was determined to be the best option for removing NaCl, since attempts at rinsing the powder prior to calcination also resulted in some sample oxidation. After removing all of the NaCl, the fayalite crystals were rinsed with methanol and dried with a rotary evaporator.

2.3. Characterization

Phases were identified by powder X-ray diffraction (PXRD) using a PANalytical X'pert PRO 2-circle X-ray diffractometer with Cu $K\alpha_{1,2}$ incident radiation (λ = 1.54Å)

operating at 45 keV and 40 mA. PXRD data were collected at room temperature between 15 and 100° 2θ with a step size of 0.02° and count time of 100 s per step. A diffracted beam monochromator was used to filter fluorescence generated by interaction of the incident Cu $K\alpha_{1,2}$ radiation with Fe in the fayalite crystals. PXRD pattern analysis and Rietveld structure refinements were performed using the HighScore Plus program from PANalytical.

All synthesis batches were examined for trace element contamination using a Shimadzu MicroXRF X-ray fluorescence spectrometer. Excitation X-rays were generated using a non-monochromated rhodium tube operated at 50 kV. X-ray fluorescence was measured with a lithium-drifted silicon detector. The samples were analyzed as dry powders. The data were analyzed for trace contaminants with the built-in Shimadzu Micro-XRF software, which scans for known major lines of all elements from sodium to uranium.

Nanofayalite crystal morphology was examined with a Zeiss Merlin field emission scanning electron microscope (FE-SEM) with an accelerating voltage of 20 kV. FE-SEM mounts were prepared by dispersing small amounts of fayalite in methanol and placing a drop of the dispersed fayalite on a carbon coated copper grid (300 mesh). The grid was dried before measurement.

Specific surface areas were determined by standard N_2 multipoint Brunauer-Emmett-Teller (BET) and Langmuir adsorption methods using a Micromeritics Gemini 2375 surface area analyzer.

3. Results and Discussion

3.1. Composition

PXRD analysis of multiple synthesis batches match well with library fayalite (PDF# 96-900-0561; Hazen, 1977) and indicate the production of nearly pure fayalite with good synthesis repeatability (Figure III-3). Low intensity peaks at 44.9°, 65.2°, 82.6° and 99.2° 2θ are a result of the presence of minor amounts of reduced Fe (PDF# 96-900-2672; Fjellvag et al., 2002), but Rietveld structure refinement estimated the amount of Fe in any batch to be 3% or less. The probable explanation for this small amount of Fe is from errors in reactant weighing and addition, but additional factors, such as reduction of surface iron or the incomplete hydrolysis of iron(II) ethoxide or TEOS, may be possible.

Elemental analysis of multiple fayalite synthesis batches indicate trace amounts of Mn^{2+} but compose less than 0.3% of the total cation wt % in the fayalite. This trace impurity is found in all batches of fayalite, and analysis of the starting material indicates that it is inherited from the iron(II) chloride.

3.2. Color and morphology

Though the color of large, natural crystals of fayalite generally ranges from greenish-brown to black (Hazen, 1977; Deer et al., 1992), synthesized nanofayalite crystals are medium to light gray in color. This color also differs significantly from the white color observed for synthesized nanoforsterite and the green color commonly associated with most natural, Mg-rich olivine (Deer et al., 1992).

Rietveld refinement of PXRD data indicates an estimated average nanofayalite crystal size of ~100 nm. FE-SEM imaging of these crystals corroborate this estimate, and

show crystals to be 100–150 nm in size and euhedral to subhedral in shape (Figure III-4). Despite their small size, some of the nanofayalite crystals show corner facets commonly seen in larger, well-formed fayalite crystals. These crystals are clumped together initially but can be separated by sonication and modest grinding with a mortar and pestle. Space between clumped grains was likely filled with NaCl, which was removed during rinsing.

Measurements of the specific surface area for synthesized fayalite range between 12.6 to 77.4 m^2/g depending on the determination method and synthesis batch (Table III-1). Average measurement values from the BET and Langmuir methods are 27.7 m^2/g and 45.3 m^2/g, respectively. Since the Langmuir method assumes monolayer adsorption only, the BET method is likely a more accurate measure of the surface area of silicates, like fayalite, where both chemisorption and physisorption are known to occur. Average synthesis yields are ~6.7 g of fayalite material per batch (see Table III-1). Estimates of the number of crystals per batch can be calculated by assuming an approximate spherical shape for these crystals (radius=75 nm) and by using the average surface area of 27.7 m^2/g determined by BET analysis. This calculation yields an estimated 2.6×10^{16} nanofayalite crystals per batch.

3.3. Controlling redox

The most significant challenge in producing nanofayalite was controlling the redox environment during gel formation and calcination. Lack of redox control can easily result in the formation of magnetite ($Fe^{2+}Fe^{3+}{}_2O_4$) and hematite ($Fe^{3+}{}_2O_3$) in more oxidizing environments, or wüstite ($Fe^{2+}O$) and metallic iron (Fe^0) in more reducing environments (see Figure III-1). Previous studies that have produced large, Fe-bearing olivine crystals by Czochralski (Finch et al., 1980) and floating-zone image furnace

(Hanson et al., 1991; Tsai et al., 1996a; Tsai et al., 1996b) methods have used a variety of inert gases (e.g. Ar, Ar + 4% H_2, N_2, CO/CO_2) and oxygen getters (e.g. Ni, Ti, or Fe shavings) to help regulate fO_2 conditions during crystal growth.

To reduce oxygen infiltration, Ar was continuously pumped through the setup until the end of the gel formation stage. Synthesis batches in which the gel was dried slowly in a vacuum oven (both with and without heat) overnight prior to calcine resulted in mixtures of fayalite and magnetite. Solvent removal and sol-gel drying using a rotary evaporator was the preferred method for maintaining a reduced environment and drying the gel quickly. During calcination, various oxygen getters (Ni and Ti shavings) and gases (Ar + 4% H_2, N_2) were tried. However, after resolving the oxidation issues during the gel formation and drying stages, the flow of N_2 without any oxygen getter was found to be sufficient to regulate fO_2 during calcination.

Another important control on redox was regulating solution pH during reactant mixing and subsequent hydrolysis. A solution pH too far from neutral can promote oxidation, but a solution pH too near neutral will not catalyze hydrolysis and can prevent gel formation. Early synthesis attempts using either concentrated HCl or H_2O_2 as the hydrolyzing reagent resulted in the formation of hematite. Instead, adding approximately 10 mL of 0.2 M NaOH changed the total solution pH to a value near 9; basic enough to catalyze hydrolysis, but not so extreme as to promote oxidation.

4. Conclusions

The sol-gel technique presented here is a simple, fast, and reproducible synthesis method for the production of nanofayalite. Because ferrous iron is required to form

fayalite, the major challenge during this synthesis development and implementation was controlling fO_2. This technique provides an abundant quantity of nanofayalite for use in a variety of future planetary science, material science, energy storage science and other geochemical studies.

Acknowledgments

This manuscript is a portion of M.T. DeAngelis's dissertation work at the University of Tennessee, Knoxville. Many thanks to Andrew Payzant and Chengdu Liang in the Center for Nanophase Materials Sciences at Oak Ridge National Laboratory for help with PXRD and BET analyses, and to David Cole and David Wesolowski in the Geochemistry and Interfacial Sciences group for financial support. This research was conducted at the Center for Nanophase Materials Sciences, which is sponsored at Oak Ridge National Laboratory by the Office of Basic Energy Sciences, U.S. Department of Energy. Additional funding for this work was provided by the Division of Chemical Sciences, Geosciences, and Biosciences, Office of Basic Energy Sciences, U.S. Department of Energy. Oak Ridge National Laboratory is managed and operated by UT-Battelle for the U.S. Department of Energy under contract DE-AC05-00OR22725.

References Cited

Afonina, G. A., Leonov, V. G., and Popova, O. N. (2005) Production of forsterite powder using sol-gel technology. *Glass and Ceramics* **62**, 248-252.

Caillot, T., Aymes, D., Stuerga, D., Viart, N., and Pourroy, G. (2002) Microwave flash synthesis of iron and magnetite particles by disproportionation of ferrous alcoholic solutions. *Journal of Materials Science* **37**, 5153-5158.

Cole, D. R., Herwig, K. W., Mamontov, E., and Larese, J. Z. (2006) Neutron scattering and diffraction studies of fluids and fluid-solid interactions. *Neutron Scattering in Earth Sciences* **63**, 313-362.

Deer, W. A., Howie, R. A., and Zussman, J. (1992) *An introduction to the rock-forming minerals (2nd ed.)*. Longman Scientific and Technical.

Douy, A. (2002) Aqueous syntheses of forsterite (Mg_2SiO_4) and enstatite ($MgSiO_3$). *Journal of Sol-Gel Science and Technology* **24**, 221-228.

Dyar, M. D., Sklute, E. C., Menzies, O. N., Bland, P. A., Lindsley, D., Glotch, T., Lane, M. D., Schaefer, M. W., Wopenka, B., Klima, R., Bishop, J. L., Hiroi, T., Pieters, C., and Sunshine, J. (2009) Spectroscopic characteristics of synthetic olivine: An integrated multi-wavelength and multi-technique approach. *American Mineralogist* **94**, 883-898.

Fabian, D., Henning, T., Jager, C., Mutschke, H., Dorschner, J., and Wehrhan, O. (2001) Steps toward interstellar silicate mineralogy - VI. Dependence of crystalline olivine IR spectra on iron content and particle shape. *Astronomy & Astrophysics* **378**, 228-238.

Finch, C. B., Clark, G. W., and Kopp, O. C. (1980) Czochralski Growth of Single-Crystal Fayalite under Controlled Oxygen Fugacity Conditions. *American Mineralogist* **65**, 381-389.

Fjellvag, H., Hauback, B. C., Vogt, T., and Stolen, S. (2002) Monoclinic nearly stoichiometric wustite at low temperatures. *American Mineralogist* **87**, 347-349.

Frost, B. R. (1991) Introduction to Oxygen Fugacity and Its Petrologic Importance In: Lindsley, D. H. Ed., *Oxide Minerals: Petrologic and Magnetic Significance*. Mineralogical Society of America, Washington, D.C.

Hamilton, V. E. (2010) Thermal infrared (vibrational) spectroscopy of Mg-Fe olivines: A review and applications to determining the composition of planetary surfaces. *Chemie Der Erde-Geochemistry* **70**, 7-33.

Hanson, D. R., Young, M., and Ryerson, F. J. (1991) Growth and Characterization of Synthetic Iron-Bearing Olivine. *Physics and Chemistry of Minerals* **18**, 53-63.

Hazen, R. M. (1977) Effects of Temperature and Pressure on Crystal-Structure of Ferromagnesian Olivine. *American Mineralogist* **62**, 286-295.

Herd, C. D. K. (2008) Basalts as Probes of Planetary Interior Redox State. In: Rosso, J. J. Ed., *Oxygen in the Solar System, Reviews in Mineralogy and Geochemistry*. Mineralogical Society of America, Washington, D.C.

Hofmeister, A. M. (1987) Single-Crystal Absorption and Reflection Infrared-Spectroscopy of Forsterite and Fayalite. *Physics and Chemistry of Minerals* **14**, 499-513.

Hofmeister, A. M. and Pitman, K. M. (2007) Evidence for kinks in structural and thermodynamic properties across the forsterite-fayalite binary from thin-film IR absorption spectra. *Physics and Chemistry of Minerals* **34**, 319-333.

Mamontov, E., Vlcek, L., Wesolowski, D. J., Cummings, P. T., Wang, W., Anovitz, L. M., Rosenqvist, J., Brown, C. M., and Sakai, V. G. (2007) Dynamics and structure of hydration water on rutile and cassiterite nanopowders studied by quasielastic neutron scattering and molecular dynamics simulations. *Journal of Physical Chemistry C* **111**, 4328-4341.

Park, D. G., Burlitch, J. M., Geray, R. F., Dieckmann, R., Barber, D. B., and Pollock, C. R. (1993) Sol-Gel Synthesis of Chromium-Doped Forsterite. *Chemistry of Materials* **5**, 518-524.

Redfern, S. A. T., Artioli, G., Rinaldi, R., Henderson, C. M. B., Knight, K. S., and Wood, B. J. (2000) Octahedral cation ordering in olivine at high temperature. II: an in situ neutron powder diffraction study on synthetic $MgFeSiO_4$ (Fa50). *Physics and Chemistry of Minerals* **27**, 630-637.

Tsai, M. T. (2002) Synthesis of nanocrystalline forsterite fiber via a chemical route. *Materials Research Bulletin* **37**, 2213-2226.

Tsai, M. T. (2003) Preparation and crystallization of forsterite fibrous gels. *Journal of the European Ceramic Society* **23**, 1283-1291.

Tsai, T. L., Markgraf, S. A., and Dieckmann, R. (1996a) Floating-zone growth and characterization of Fe_2SiO_4 single crystals. *Journal of Crystal Growth* **169**, 759-763.

Tsai, T. L., Markgraf, S. A., Higuchi, M., and Dieckmann, R. (1996b) Growth of $(Fe_xMg_{1-x})_2SiO_4$ single crystals by the double pass floating zone method. *Journal of Crystal Growth* **169**, 764-772.

Wadhwa, M. (2008) Redox conditions on small bodies, the Moon and Mars. In: Rosso, J. J. Ed., *Oxygen in the Solar System, Reviews in Mineralogy and Geochemistry*. Mineralogical Society of America, Washington, D.C.

Wang, J. P. and Luo, H. L. (1994) Preparation and properties of pure nanocomposite Fe-SiO_2 using the sol-gel method. *Journal of Magnetism and Magnetic Materials* **131**, 54-60.

Yeager, K. E., Burlitch, J. M., and Loehr, T. M. (1993) Intermediates in the Sol-Gel Synthesis of Forsterite. *Chemistry of Materials* **5**, 525-534.

Appendix III

Table III-1. Synthesis yields and surface areas

Batch Name	Yield (g)	Multipoint BET (m^2/g)	Langmuir (m^2/g)
FS21	6.6	21.2	34.4
FS22	6.7	12.6	21.2
FS23	6.2	47.0	77.4
FS24	6.6	27.2	44.5
FS25	7.0	30.2	48.9
FS26	6.8	28.0	45.5
Averages	**6.7**	**27.7**	**45.3**

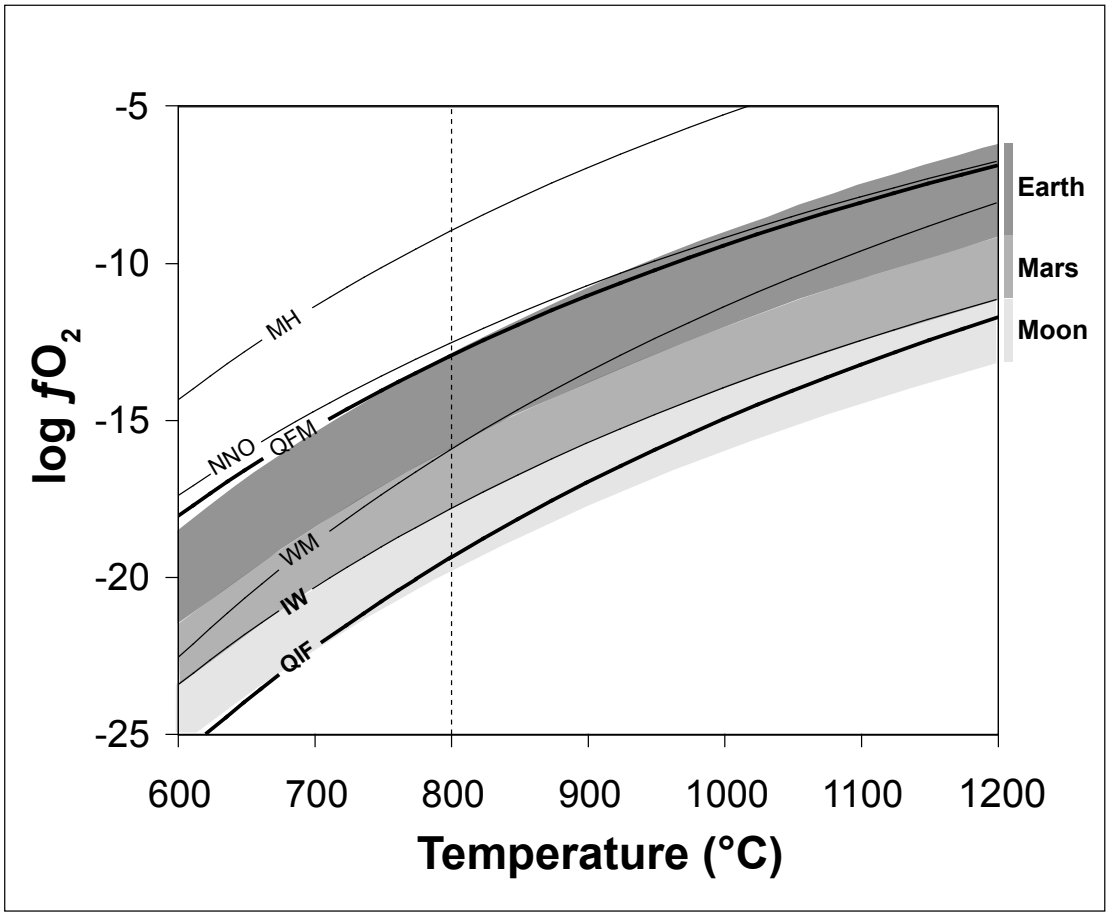

Figure III-1. Log oxygen fugacity vs. temperature at 1 bar pressure showing some common oxygen buffers (MH, magnetite–hematite; NNO, nickel–nickel oxide; FMQ, fayalite–magnetite–quartz; WM, wüstite–magnetite; IW, iron–wüstite; QIF, quartz-iron-fayalite) (Frost, 1991). The area between the darker FMQ and QIF curves is the range of stability for fayalite. The shaded areas represent estimated ranges for the redox conditions on the Moon, Mars, and Earth (Frost, 1991; Herd, 2008; Wadhwa, 2008). The vertical dashed line at 800 °C shows the calcination temperature.

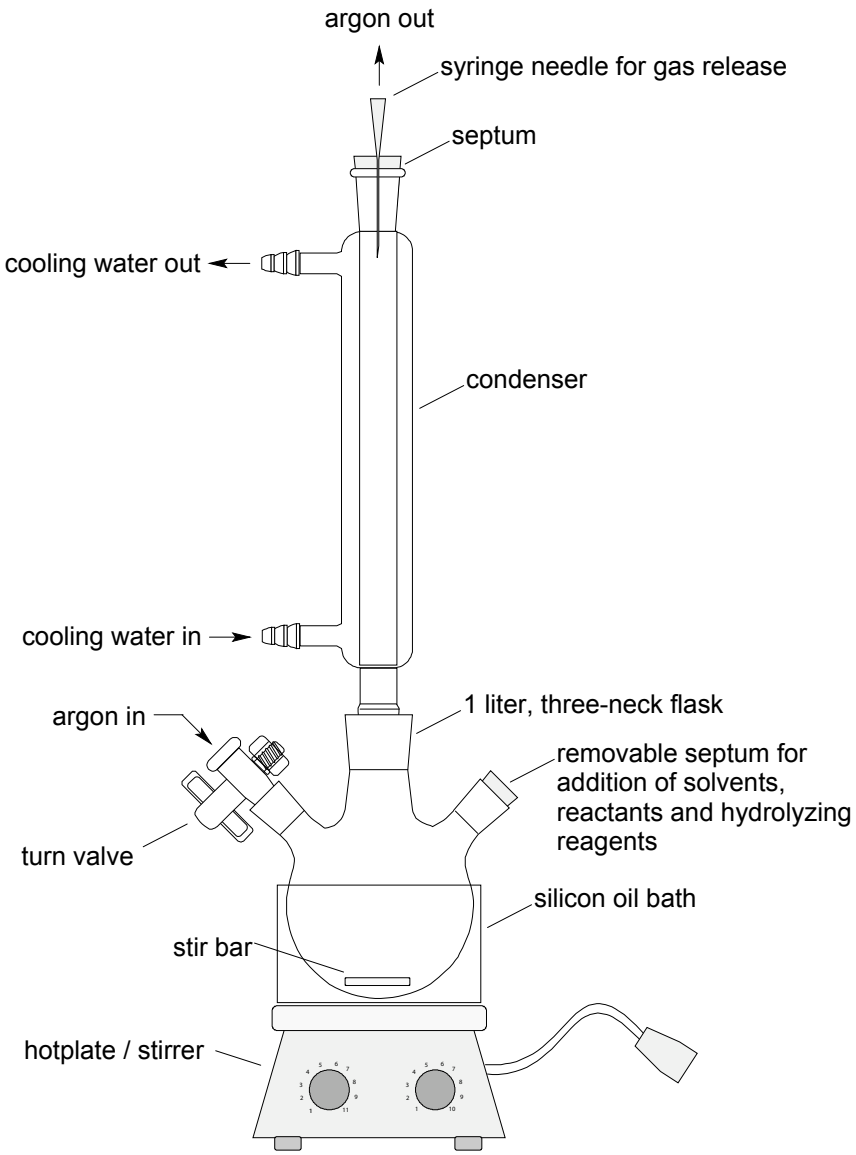

Figure III-2. Experimental setup for nanofayalite synthesis.

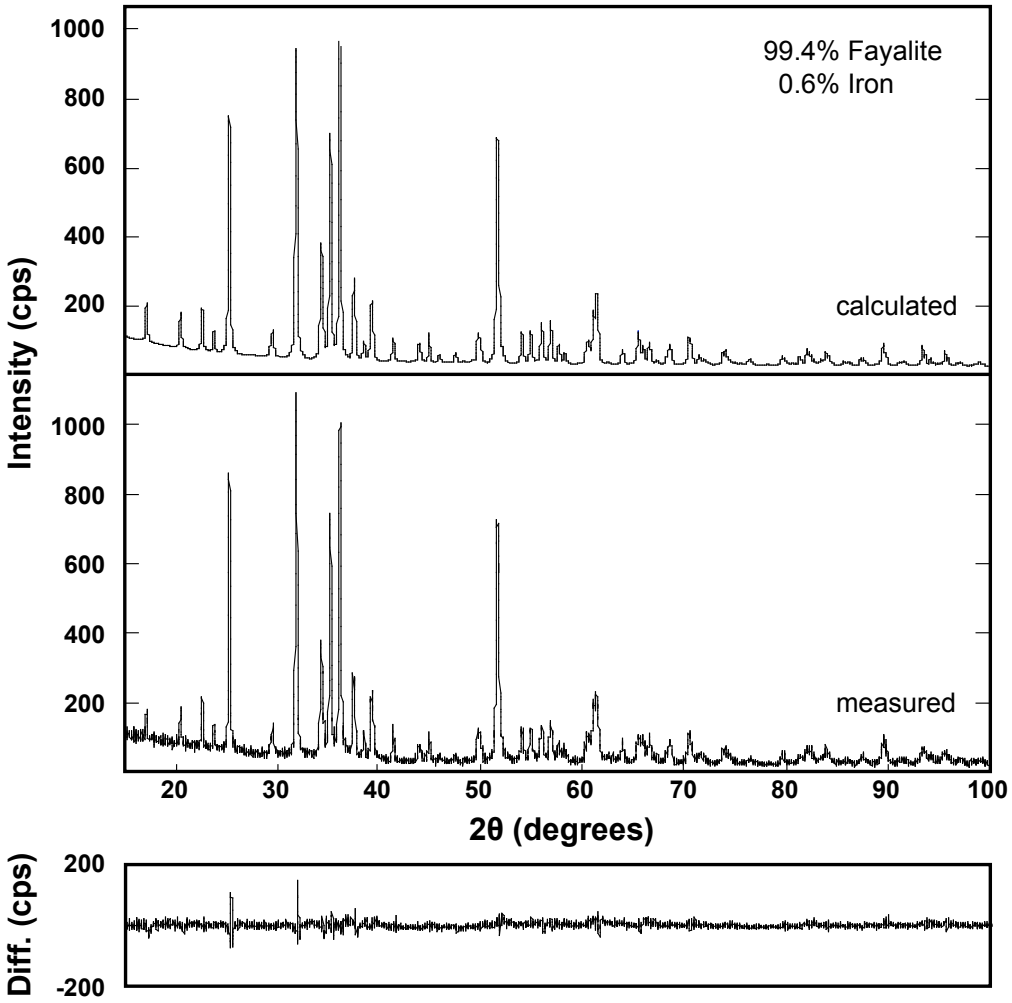

Figure III-3. Measured and calculated powder X-ray diffraction patterns of nanofayalite batch FS22. Rietveld structure refinement indicates 99.4% fayalite and 0.6% iron calculated using library patterns for both fayalite (PDF# 96-900-0561; Hazen, 1977) and iron (PDF# 96-900-2672; Fjellvag et al., 2002). Differences between the measured and calculated intensities are shown at the bottom.

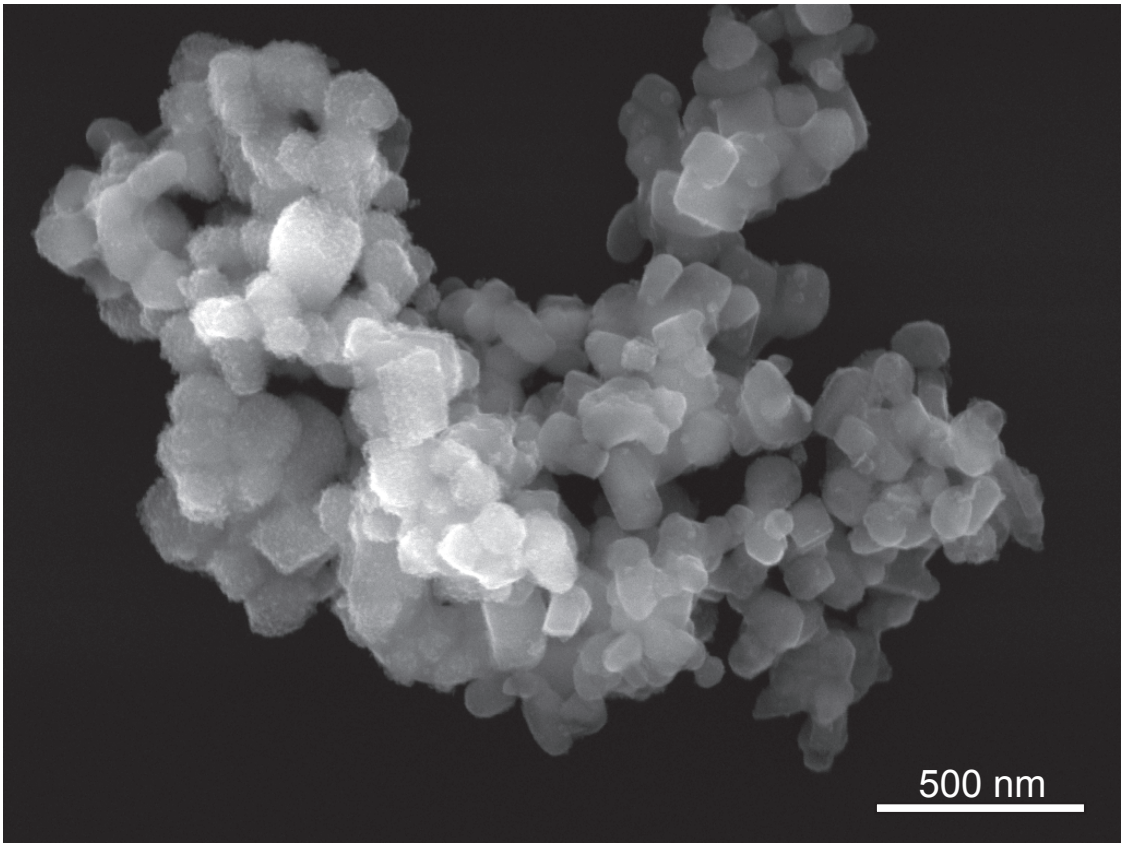

Figure III-4. FE-SEM image of nanofayalite crystals from batch FS21. Crystals are generally euhedral to subhedral in shape, and range in size from 100–150 nm.

Part IV.
Growth of Intermediate Composition Olivine [$(Mg_xFe_{1-x})_2SiO_4$] Using a Lithium Borate Flux

This part is a reformatted version of a paper, by the same name, to be submitted to American Mineralogist by Michael T. DeAngelis, Lawrence M. Anovitz, Theodore C. Labotka, D. Alan Frederick, Mostafa Fayek, and David R. Cole

DeAngelis, M.T., Anovitz, L.M., Labotka, T.C., Frederick, D.A., Fayake, M. and Cole, D.R. Growth of intermediate composition olivine [$(Mg_xFe_{1-x})_2SiO_4$] using a lithium borate flux. 2011. *To be submitted*.

Abstract

Olivine crystals with an intermediate composition, $(Mg_xFe_{1-x})_2SiO_4$ (x=0.4-0.6), were grown using a coupled decarbonation and flux growth method. A starting mixture of magnesium carbonate, iron (II) carbonate, and colloidal silica powders were mixed with a lithium borate flux and heated under vacuum to 1100 °C for three days. The resulting crystals are generally small (< 1 mm), euhedral to subhedral in form, and are compositionally zoned with Mg-rich cores grading to Fe-rich rims. Analysis by secondary ion mass spectrometry (SIMS) showed that minor amounts of lithium and boron are present in the olivine crystals and that they are compositionally zoned with Li- and B-rich cores grading to Li- and B-poor rims. The advantage of growing crystals by this method is that the components for growth can be dissolved and crystals can be grown at temperatures significantly below solidus temperatures. The high fO_2 conditions in the terrestrial mantle generally result in crystallization of natural olivine with Mg-rich compositions; therefore, this crystal growth method may be particularly beneficial to experimental investigators requiring intermediate composition olivine crystals for use in extraterrestrial analog experiments.

1. Introduction

The mineral olivine, $(Mg,Fe)_2SiO_4$, is one of the most volumetrically significant silicate minerals in the solar system, composing a major portion of the mantle of the Earth, the surface and mantle of the Moon and Mars, asteroids (e.g. Vesta), and a variety of other extraterrestrial materials such as meteorites and interplanetary dust particles (IDPs). The existence of olivine in these various locations and environmental conditions has encouraged extensive and continued experimental investigation of its physical and chemical properties. Beginning with the $MgO\text{-}FeO\text{-}SiO_2$ equilibrium studies of Bowen and Schairer (Bowen and Schairer, 1935), a large community of olivine experimental investigators now exists, with example studies ranging from the experimental dissolution of olivine under ambient conditions (Brantley, 2008), mid-ocean ridge hydrothermal alteration experiments (Seyfried et al., 2007), high pressure and temperature terrestrial mantle studies (Ringwood, 1975), a variety of extraterrestrial analog experiments (Hurowitz et al., 2006), and many others. A necessity for all these experimental investigations is the acquisition and use of well-characterized starting material. Although natural olivine such as the San Carlos olivine from San Carlos, Arizona, has been often used in experimental studies, this and other natural olivine crystals contain impurities, inclusions, and crystal structure defects that can adversely affect experimentation. Stringent experimental design requirements, therefore, often necessitate the use of texturally and compositionally controlled starting material.

For this study, the goal was to develop a method for the production of olivine single crystals with an intermediate composition, $(Mg_xFe_{1-x})_2SiO_4$ (x=0.4–0.6). This composition is present on both the Moon and Mars, but is limited to only a few locations

(e.g. Kiglapait layered mafic intrusion in Labrador) on Earth. The high fO_2 conditions within th(McSween et al., 2006)e terrestrial mantle generally limit the olivine to more Mg-rich (forsterite) compositions. The conditions in the mantles of both the Moon and Mars do not have this limitation allowing for a wider range of olivine compositions to crystallize (Figure IV-1). Spectroscopic data obtained with the Thermal Emission Spectrometer (TES) onboard Mars Global Surveyor, martian meteorite analyses, and examination of Gusev crater basalts with the Spirit rover, for example, indicate a global distribution of olivine on the martian surface that is more Fe-rich than terrestrial olivine (McSween et al., 2006). Since the presence of olivine within the intermediate solid-solution range found on the Moon and Mars is not common on Earth and since significant amounts of olivine from either location have not yet been acquired, any experimentation with this type of olivine requires that the starting material be produced synthetically.

Previous growth of olivine crystals has been accomplished by sol-gel synthesis (Park et al., 1993; Yeager et al., 1993; Douy, 2002; Tsai, 2002; Tsai, 2003; Afonina et al., 2005), the floating-zone (FZ) image furnace (Inoue et al., 1981; Takei and Hosoya, 1982; Takei et al., 1984; Hanson et al., 1991; Tsai et al., 1996a; Tsai et al., 1996b), the Czochralski (CZ) pulling method (Finch et al., 1980; Takei et al., 1984; Ito et al., 2003a; Ito et al., 2003b; Kanazawa et al., 2007), the Bridgman method (Jordan and Naughton, 1964; Wilson, 1965; Smyth, 1975), the micro-pulling-down method (Ganschow and Klimm, 2005; Klimm and Ganschow, 2005; Talik et al., 2006), the Verneuil flame-fusion method (Shankland and Hemmenway, 1963; Shankland, 1966), and the flux growth method (Grodkiewicz and Vanuitert, 1963; Vutien et al., 1971; Ozima, 1976; Wanklyn, 1977; Takei et al., 1984). Each of these methods has advantages and disadvantages

depending on the available time, operational budget, and physical requirements for the crystal(s) to be grown. White (White, 1965), Takei and Hosoya (Takei and Hosoya, 1982), and Takei et al. (Takei et al., 1984) contain useful reviews of many of these previously used olivine growth techniques.

The method selected for this study was the flux growth method, because it is relatively inexpensive and does not require a great deal of time to produce crystals. The methods and results of our $Mg_xFe_{1-x}SiO_4$ growth experiments using a lithium borate flux are presented here.

2. Experimental Procedures

2.1. Starting material

The starting material was an equimolar mixture of magnesium carbonate ($4MgCO_3 \cdot Mg(OH)_2 \cdot nH_2O$, Baker Chemical Co.), iron (II) carbonate ($FeCO_3$, Strem Chemicals, Inc.), and colloidal silica (98.5 wt% SiO_2, MIN-U-SIL 5, U.S. Silica) powder that was ground in a mortar until thoroughly mixed. The advantage of using iron (II) carbonate is that the iron is already present in a reduced, ferrous (Fe^{2+}) form, which is required for the formation of olivine. The presence and amount of any adsorbed water was determined for each of the powders prior to their use in the crystal growth experiment by heating a small amount (~1 g) of each powder to 700 °C overnight. By observing the weight difference before and after the heating, the amount of adsorbed water was calculated and the mixture was adjusted slightly to ensure that it was equimolar. This was found to be especially critical for determining an appropriate

amount of magnesium carbonate to use. A deficiency in the Mg component resulted in silica oversaturation of the mixture, and the flux growth process yielded pyroxene and olivine instead of only the desired olivine. Upon heating and decarbonation, this mixture represents a bulk composition of $FeMgSiO_4$ (Fo50) olivine. A lithium borate flux (Spectroflux ® 100B, Alfa Aesar, lithium metaborate [$LiBO_2$] 80% - lithium tetraborate [LiB_4O_7] 20%) was then added to the starting material mixture so that the final mixture was 50% starting material and 50% flux by weight. This mineral–flux powder mixture was again ground in a mortar until thoroughly mixed.

2.2. Flux growth method

Approximately 3 grams of this mineral–flux powder mixture was placed in a platinum crucible and loosely covered with platinum foil. This use of a platinum cover was to ensure that the flux–mineral powder mixture remained in the crucible during heating, but it was loosely covered to ensure that any generated CO_2 could escape. The platinum crucible was heated to 1100 °C in a vacuum furnace for three days. The use of a vacuum furnace ensured that conditions remained reducing during crystal growth. After the three day run, the crucible was cooled under vacuum, removed from the vacuum furnace and the grown crystals were removed by scraping the crucible. The crystals were mounted in epoxy and a grain mount was polished for analysis.

2.3. Analytical methods

The composition of the flux grown crystals was examined using a Siemens D5005 θ-θ X-ray powder diffractometer (XRD) and a CAMECA SX-100 electron microprobe (EMP). Compositional information was obtained by XRD analysis using a Cu Kα tube at

40 kV and 30 mA, from 5 to 70° 2θ, with a 0.2° step, a 2 s counting time per step, and a graphite monochrometer. For generation of back-scattered electron (BSE) and Mg, Si, and Fe X-ray images, the EMP had an accelerating voltage potential of 15 kV, a beam current of 4 nA, and a beam size of 1 µm. Images were generated by rastering over the area of interest, generally 256 x 256 µm using a 2 µm step with a counting time of 1 ms per step. Quantitative mineral analyses were also collected with the EMP. For these analyses, the EMP had an accelerating voltage potential of 15kV, a beam current of 6 nA, a beam size of 1 µm, and a counting time of 40 seconds for most elements. A natural forsterite standard was used for calibration.

Quantitative analyses of $^{7}Li^{+}$, $^{11}B^{+}$, $^{24}Mg^{+}$, $^{30}Si^{+}$, and $^{54}Fe^{+}$ were obtained using the CAMECA ims 7f Geo secondary ion mass spectrometer (SIMS) located in the Manitoba Regional Materials and Surface Characterization Facility at the University of Manitoba. The sample was prepared by applying a thin gold coat (~15 seconds of sputtering time) to the grain mount. Spot analyses of the sample and a NIST 610 glass standard were measured using a 1 nA $^{16}O^{-}$ primary beam accelerated at +10 kV. Spots on the sample and standard were pre-sputtered for ~30 seconds to achieve stable count rates.

3. Results and discussion

3.1. Olivine crystal characteristics

The three day heating at 1100 °C in a vacuum furnace of the powdered mixture resulted in the growth of olivine crystals that are generally small (< 1 mm in length), dark in color, and have euhedral to subhedral crystal form. Initial compositional examination

by XRD analysis indicates that the olivine crystals have an approximate Fo60 ($Mg_{1.2}Fe_{0.8}SiO_4$) bulk composition (Figure IV-2). The intensities of diffraction peaks for the flux-grown crystals vary somewhat from those in the ICDD library, probably because of the presence of small amounts of unreacted starting material; however, the locations of 2θ peak locations for both the library pattern and the flux-grown crystals pattern are identical.

3.2. Compositional zoning of olivine

After mounting the sample in epoxy, the sample was analyzed using the SX-100 electron microprobe at the University of Tennessee. Back-scattered electron (BSE) images of the sample show a matrix surrounding olivine crystals consisting of minor amounts of flux glass and unreacted starting powder material (Figure IV-3). This glass is presumed to have formed during the quench of the crystal growth experiment. The presence of unreacted material may have influenced initial XRD estimates of the bulk composition; therefore, both X-ray compositional maps and detailed spot analyses were collected on several crystals. A qualitative examination of these crystals from the X-ray image (Figure IV-3) indicates that these crystals are zoned in both Fe and Mg, with growth zoning transitioning from Mg-rich cores to Fe-rich rims. Two olivine crystals (C1 and C2) were selected for further quantitative analyses. Olivine crystal C1 is sliced through the core and has a complete range in growth zoning, whereas olivine crystal C2 has been obliquely sliced and has more detail of zoning near the crystal rim (Figure IV-3). A quantitative EMP analysis profile of C1 (Figure IV-4) shows that the core is Mg-rich with a Fo68 ($Mg_{1.38}Fe_{0.66}SiO_4$) composition that grades to a Fe-rich rim with a Fo55 ($Mg_{1.08}Fe_{0.90}SiO_4$) composition (Table IV-1). A quantitative EMP analysis profile of C2

(Figure IV-4) shows a similar trend, but the oblique slice through this crystal means that the high Mg values observed in the core of crystal C1 are not seen here (Table IV-2). The growth zoning in both of these examples represents an expected heterogeneity because of olivine growth from a finite reservoir of starting material; the incorporation of Fe during olivine crystallization increased as the amount of available magnesium in solution decreased.

3.3. Flux and olivine interaction

An expectation when using the flux method for crystal growth is that the flux acts only as a solvent for dissolving the growth components and that the flux material itself does not interact with the crystals during growth. To determine if there was any interaction between the lithium borate flux used in this experiment and the crystals, detailed compositional information was collected by the secondary ion mass spectrometer (SIMS) located at the University of Manitoba. Quantitative ion probe spot analyses (n=6) of $^{7}Li^{+}$, $^{11}B^{+}$, $^{24}Mg^{+}$, $^{30}Si^{+}$, and $^{54}Fe^{+}$ were collected along a line traverse in the C1 crystal (Figure IV-3). The measured $^{7}Li^{+}/^{30}Si^{+}$, $^{11}B^{+}/^{30}Si^{+}$, $^{24}Mg^{+}/^{30}Si^{+}$, and $^{54}Fe^{+}/^{30}Si^{+}$ ratios were converted to concentrations in parts per million Li, B, Mg, and Fe using standard values determined from measurement of a NIST 610 glass standard (Table IV-3). The Mg–Fe zoning profile that was observed with the EMP along the semi-minor axis of crystal C1 is also observed along the semi-major axis from data collected using the SIMS (Figure IV-5). The distribution of Li and B appears to be concomitant with Mg zoning, showing a nearly symmetrical enrichment of Li and B in the core of the crystal grading to depletion of both elements toward the rim. The large, positive deviation of the sixth point for B concentration is likely a result of the spot overlapping the grain

boundary, thus including material from both the olivine grain and the matrix in the analysis and indicating that boron is still abundant in the matrix.

The SIMS analyses of crystal C1 indicate that some amount of Li and B are present within the olivine crystal, however, the precise crystallographic site occupancy and mechanism for zoning of lithium and boron are unknown. Olivine has an orthorhombic structure in which Mg^{2+} and Fe^{2+} occupy distinct M1 and M2 octahedral sites located between isolated silicon–oxygen tetrahedra. The distribution of Mg^{2+} and Fe^{2+} between octahedral sites is generally disordered; however, intermediate composition olivine has a slight preference for Fe^{2+} occupation within the smaller M1 site (Brown, 1982). The ionic radius of Li^{+} in octahedral coordination ($^{VI}Li^{+}$ radius=0.90; (Shannon, 1976)) is similar to the radii of Fe^{2+} ($^{VI}Fe^{2+}$ radius=0.92; (Shannon, 1976)) and Mg^{2+} ($^{VI}Mg^{2+}$ radius=0.86; (Shannon, 1976)), therefore, there should be no preference for Li^{+} to occupy one site over the other. Previous studies of some lithium silicate and lithium phosphate olivines, however, have shown that Li^{+}, and other monovalent cations, also preferentially occupy the M1 site (Geller and Durand, 1960; Finger and Rapp, 1970). This shared preference of both Li^{+} and Fe^{2+} for the M1 site suggests that the decrease of Li^{+} from core to rim may be crystallographically related to the increase in Fe^{2+} from core to rim. Though it may be reasonable for Li^{+} to occupy an octahedral site based on its size, a charge imbalance remains. Vacancies in the structure may be required to accommodate Li^{+}, which could explain why the total amount of Li^{+} in this crystal remains small.

Boron is more abundant than lithium in crystal C1, however, interpreting its site occupancy and zoning mechanism is equally challenging. The most common boron-

bearing mineral with an olivine structure is the mineral sinhalite, $MgAlBO_4$ (Claringbull and Hey, 1952; Fang and Newnham, 1965; Hayward et al., 1994; Anovitz and Grew, 1996). The relatively small B^{3+} cation ($^{IV}B^{3+}$ radius=0.25; (Shannon, 1976)) is bound to oxygen to form BO_4 tetrahedra analogous to the SiO_4 tetrahedra present in silicate olivines. The boron may be located in these tetrahedral sites, however, the silicon values in both the SIMS and EMP line traverses across crystal C1 are fairly constant and do not reflect the zoning that would be required to accommodate the observed zoning of boron.

Another possibility to consider is that the boron may reside within an octahedral site. The ionic radius of the B^{3+} cation in octahedral coordination is larger ($^{VI}B^{3+}$ radius=0.41; (Shannon, 1976)) than in tetrahedral coordination; however, it is still nearly half the size of the Fe^{2+} or Mg^{2+} that normally fill these sites. Despite this size imbalance, it may be tempting to envision a coupled substitution scenario in which $^{VI}B^{3+} + {}^{VI}Li^{+} \leftrightarrow 2(^{VI}Mg^{2+}, {}^{VI}Fe^{2+})$. Unfortunately, both the ionic radius difference and the large difference between the amount of lithium and boron measured in crystal C1 also make this unlikely.

The exact nature of boron and lithium incorporation and zoning in these crystals remains unanswered. Regardless, lithium and boron are relatively minor components that do not significantly affect the bulk chemical properties of these olivine crystals.

3.4. Advantages of the flux growth method

The primary advantage of the flux growth method is that the use of a flux allows for the rapid growth of olivine crystals under subsolidus conditions. Because the olivine structure has complete solid solution between forsterite (Mg_2SiO_4) and fayalite (Fe_2SiO_4), the solidus curve is continuous from the melting point of pure forsterite at 1890 °C to the

lower melting point of fayalite at 1205 °C. A bulk mixture of intermediate composition olivine would normally melt at temperatures exceeding 1500 – 1600 °C before they could be cooled and crystallized. The addition of the lithium borate flux allowed for dissolution of the starting components and crystallization of the olivine crystals at 1100 °C, well below the melting point for an intermediate composition olivine. This lower temperature is advantageous because it falls within the heating range of many commercially available furnaces, so there is a reduced need for expensive specialized equipment.

Another important advantage of the flux growth method is that crystals grown by this method generally remain small. Many experimental studies require the use of starting material with moderate to high surface areas. To create these high surface area powders, large samples are often crushed and sieved to obtain the desired size. The process of crushing and grinding crystalline samples can generate numerous crystal structure defects. These defects could adversely affect the outcome of experiments in which powdered samples are used. The flux growth of crystals, however, allows for the growth of crystals to a known size, and removes the need for additional mechanical processing. This is of particular importance when the starting material is used in experiments intended to mimic natural processes occurring in natural materials (e.g. diffusion studies).

4. Conclusions

The intent of this study was to develop a simple and straightforward method for the growth of intermediate composition olivine crystals. These experiments and analyses

demonstrate that a coupled decarbonation and flux growth method can be used to grow subhedral to anhedral olivine crystals that are within the objective compositional range of $Mg_{1.2}Fe_{0.8}SiO_4$ (Fo60) – $Mg_{0.8}Fe_{1.2}SiO_4$ (Fo40).

The temperature of 1100 °C was chosen to assure complete dissolution of the flux and starting material while maintaining a temperature significantly below the solidus curve for intermediate composition olivine. Variation in temperature and duration of growth would allow for controlled modification to the size and compositional range of grown crystals. With continued refinement of this flux growth technique, it may be possible to develop a specific composition versus time of growth curve for a known sample amount and experimental setup.

Acknowledgments

The authors wish to thank Dr. Zhili Feng in the Materials Science and Technology Division at ORNL for the use of the vacuum furnace. We also wish to thank Mr. Allan Patchen at the University of Tennessee for assistance with EMP analyses, and Dr. Rong Liu at the University of Manitoba for assistance with SIMS analyses. Funding for this work was provided by the Division of Chemical Sciences, Geosciences, and Biosciences, Office of Basic Energy Sciences, U.S. Department of Energy. Oak Ridge National Laboratory is managed and operated by UT-Battelle for the U.S. Department of Energy under contract DE-AC05-00OR22725.

References Cited

Afonina, G. A., Leonov, V. G., and Popova, O. N. (2005) Production of forsterite powder using sol-gel technology. *Glass and Ceramics* **62**, 248-252.

Anovitz, L. M. and Grew, E. S. (1996) Mineralogy, petrology and geochemistry of boron: An introduction. *Boron* **33**, 1-40.

Bowen, N. L. and Schairer, J. F. (1935) The system MgO-FeO-SiO2. *American Journal of Science* **29**, 151-217.

Brantley, S. L. (2008) Kinetics of Mineral Dissolution. In: Brantley, S. L., Kubicki, J. D., and White, A. F. Eds., *Kinetics of water-rock interaction*. Springer Verlag, New York.

Brown, G. E. (1982) Olivines and silicate spinels. In: Ribbe, P. H. Ed., *Orthosilicates*. Mineralogical Society of America, Washington, D.C.

Claringbull, G. F. and Hey, M. H. (1952) Sinhalite (MgAlBO4) a new mineral. *Mineralogical Magazine and Journal of the Mineralogical Society* **29**, 841-849.

Douy, A. (2002) Aqueous syntheses of forsterite (Mg2SiO4) and enstatite (MgSiO3). *Journal of Sol-Gel Science and Technology* **24**, 221-228.

Fang, J. H. and Newnham, R. E. (1965) Crystal Structure of Sinhalite. *Mineralogical Magazine and Journal of the Mineralogical Society* **35**, 196-199.

Finch, C. B., Clark, G. W., and Kopp, O. C. (1980) Czochralski Growth of Single-Crystal Fayalite under Controlled Oxygen Fugacity Conditions. *American Mineralogist* **65**, 381-389.

Finger, L. W. and Rapp, G. R., Jr. (1970) Refinement of the crystal structure of Triphylite, *Carnegie Institute Washington Year Book*.

Frost, B. R. (1991) Introduction to Oxygen Fugacity and Its Petrologic Importance In: Lindsley, D. H. Ed., *Oxide Minerals: Petrologic and Magnetic Significance*. Mineralogical Society of America, Washington, D.C.

Ganschow, S. and Klimm, D. (2005) Growth of olivine single crystals by the micro-pulling-down method. *Crystal Research and Technology* **40**, 359-362.

Geller, S. and Durand, J. L. (1960) Refinement of the Structure of Limnpo4. *Acta Crystallographica* **13**, 325-331.

Grodkiewicz, W. H. and Vanuitert, L. G. (1963) Synthesis of Forsterite, Diopside, Akermanite, and Wollastonite from Molten Pbo. *Journal of the American Ceramic Society* **46**, 356-356.

Hanson, D. R., Young, M., and Ryerson, F. J. (1991) Growth and Characterization of Synthetic Iron-Bearing Olivine. *Physics and Chemistry of Minerals* **18**, 53-63.

Hayward, C. L., Angel, R. J., and Ross, N. L. (1994) The Structural Redetermination and Crystal-Chemistry of Sinhalite, Mgalbo4. *European Journal of Mineralogy* **6**, 313-321.

Herd, C. D. K. (2008) Basalts as Probes of Planetary Interior Redox State. In: Rosso, J. J. Ed., *Oxygen in the Solar System, Reviews in Mineralogy and Geochemistry*. Mineralogical Society of America, Washington, D.C.

Hurowitz, J. A., McLennan, S. M., Tosca, N. J., Arvidson, R. E., Michalski, J. R., Ming, D. W., Schroder, C., and Squyres, S. W. (2006) In situ and experimental evidence for acidic weathering of rocks and soils on Mars. *Journal Of Geophysical Research-Planets* **111**.

Inoue, T., Komatsu, H., Hosoya, S., and Takei, H. (1981) Defect Structures of Synthetic Olivine. *Journal of Crystal Growth* **55**, 307-316.

Ito, K., Sato, H., Kanazawa, H., Kawame, N., Tamada, O., Miyazaki, K., Uehara, S., Iio, Y., Takei, H., Kitazawa, T., Koike, M., Matsushita, Y., and Ito, Y. (2003a) First synthesis of olivine single crystal as large as 250 carats. *Journal of Crystal Growth* **253**, 557-561.

Ito, K., Sato, H., Takei, H., Tamada, O., and Kitazawa, T. (2003b) Synthesis of large high-quality forsterite single crystals to 200 mm length and its significance. *Geochemistry Geophysics Geosystems* **4**.

Jordan, W. and Naughton, J. J. (1964) Growth of Forsterite Crystals in a Reactive Crucible. *American Mineralogist* **49**, 806-808.

Kanazawa, H., Ito, K., Sato, H., Kumatoriya, M., Miyazaki, K., Uehara, S., Tsuda, H., Kuzawa, K., Kawame, N., Kitazawa, T., Tamada, O., Boisen, M. B., and Takei, H. (2007) Synthesis and absorption spectra of large homogeneous single crystals of forsterite doped with manganese. *Journal of Crystal Growth* **304**, 492-496.

Klimm, D. and Ganschow, S. (2005) The control of iron oxidation state during FeO and olivine crystal growth. *Journal of Crystal Growth* **275**, e849-e854.

McSween, H. Y., Wyatt, M. B., Gellert, R., Bell, J. F., Morris, R. V., Herkenhoff, K. E., Crumpler, L. S., Milam, K. A., Stockstill, K. R., Tornabene, L. L., Arvidson, R. E., Bartlett, P., Blaney, D., Cabrol, N. A., Christensen, P. R., Clark, B. C., Crisp, J. A., Des Marais, D. J., Economou, T., Farmer, J. D., Farrand, W., Ghosh, A., Golombek, M., Gorevan, S., Greeley, R., Hamilton, V. E., Johnson, J. R., Joliff, B. L., Klingelhofer, G., Knudson, A. T., McLennan, S., Ming, D., Moersch, J. E.,

Rieder, R., Ruff, S. W., Schroder, C., de Souza, P. A., Squyres, S. W., Wanke, H., Wang, A., Yen, A., and Zipfel, J. (2006) Characterization and petrologic interpretation of olivine-rich basalts at Gusev Crater, Mars. *Journal Of Geophysical Research-Planets* **111**.

Ozima, M. (1976) Growth of Nickel Olivine Single-Crystals by Flux Method. *Journal of Crystal Growth* **33**, 193-195.

Park, D. G., Burlitch, J. M., Geray, R. F., Dieckmann, R., Barber, D. B., and Pollock, C. R. (1993) Sol-Gel Synthesis of Chromium-Doped Forsterite. *Chemistry of Materials* **5**, 518-524.

Ringwood, A. E. (1975) *Composition and petrology of the earth's mantle*. McGraw-Hill, New York.

Seyfried, W. E., Foustoukos, D. I., and Fu, Q. (2007) Redox evolution and mass transfer during serpentinization: An experimental and theoretical study at 200 degrees C, 500 bar with implications for ultramafic-hosted hydrothermal systems at Mid-Ocean Ridges. *Geochimica Et Cosmochimica Acta* **71**, 3872-3886.

Shankland, T. J. (1966) Synthesis and optical properties of forsterite, Tech. Rept. HP-16, Harvard University.

Shankland, T. J. and Hemmenway, K. (1963) Synthesis of Forsterite Crystals. *American Mineralogist* **48**, 200.

Shannon, R. D. (1976) Revised Effective Ionic-Radii and Systematic Studies of Interatomic Distances in Halides and Chalcogenides. *Acta Crystallographica Section A* **32**, 751-767.

Smyth, J. R. (1975) High-Temperature Crystal-Chemistry of Fayalite. *American Mineralogist* **60**, 1092-1097.

Takei, H. and Hosoya, S. (1982) Growth and properties of olivine singel crystals by the floating-zone method. In: Akimoto, S. and Manghani, M. H. Eds., *High-pressure research in geophysics, (Proc. 2nd U.S.-Japan seminar on high-pressure research applications, Hakone 1981)*. Center for Academic Publications Japan / D. Reidel, Tokyo / Dordrecht.

Takei, H., Hosoya, S., and Ozima, M. (1984). In: Sunagawa, I. Ed., *Materials Science of the Earth's Interior*. Terra Scientific Publishing Co., Tokyo.

Talik, E., Zarek, W., Kruczek, M., Ganschow, S., Skrzypek, D., and Popiel, E. (2006) Characterization of olivine single crystals grown by the micropulling-down method and terrestrial olivine by XPS, Mossbauer, magnetic and EPR methods. *Crystal Research and Technology* **41**, 979-987.

Tsai, M. T. (2002) Synthesis of nanocrystalline forsterite fiber via a chemical route. *Materials Research Bulletin* **37**, 2213-2226.

Tsai, M. T. (2003) Preparation and crystallization of forsterite fibrous gels. *Journal of the European Ceramic Society* **23**, 1283-1291.

Tsai, T. L., Markgraf, S. A., and Dieckmann, R. (1996a) Floating-zone growth and characterization of Fe2SiO4 single crystals. *Journal of Crystal Growth* **169**, 759-763.

Tsai, T. L., Markgraf, S. A., Higuchi, M., and Dieckmann, R. (1996b) Growth of (FexMg1-x)(2)SiO4 single crystals by the double pass floating zone method. *Journal of Crystal Growth* **169**, 764-772.

Vutien, L., Anthony, A. M., Gabis, V., and A.G., D. (1971) Improvement of Flux Methods, Synthesis and Purification of Natural Mineral - Forsterite. *Journal of Crystal Growth* **13**, 601.

Wadhwa, M. (2008) Redox conditions on small bodies, the Moon and Mars. In: Rosso, J. J. Ed., *Oxygen in the Solar System, Reviews in Mineralogy and Geochemistry*. Mineralogical Society of America, Washington, D.C.

Wanklyn, B. M. (1977) Growth of Silicate and Germanate Crystals from Pbo-Sio2(Geo2)Fluxes. *Journal of Crystal Growth* **37**, 51-56.

White, E. A. D. (1965) Recent Advances in Crystal Growing Techniques. *British Journal of Applied Physics* **16**, 1415-1428.

Wilson, J. (1965) Optical and electrical properties of synthetic olivine crystals. Thesis, Univ. Newcastle Upon Tyne.

Yeager, K. E., Burlitch, J. M., and Loehr, T. M. (1993) Intermediates in the Sol-Gel Synthesis of Forsterite. *Chemistry of Materials* **5**, 525-534.

Appendix IV

Table IV-1. Electron microprobe line traverse across crystal C1

Location	Spot 1	Spot 2	Spot 3	Spot 4	Spot 5	Spot 6	Spot 7	Spot 8	Spot 9	Spot 10
SiO_2	35.0	35.8	35.4	34.9	34.9	35.9	35.5	35.4	35.2	35.0
Al_2O_3	<0.03	<0.03	<0.03	0.04	<0.03	<0.03	<0.03	<0.03	0.03	<0.03
MgO	28.8	32.2	34.0	33.8	31.9	29.9	28.0	27.3	27.1	25.6
CaO	<0.03	<0.03	<0.03	<0.03	<0.03	<0.03	<0.03	<0.03	<0.03	<0.03
MnO	1.29	1.03	0.96	0.88	1.02	1.21	1.30	1.46	1.48	1.59
FeO	34.4	30.7	29.0	29.1	31.4	33.4	35.3	35.8	36.6	38.0
Oxide Total	99.55	99.78	99.47	98.71	99.19	100.4	100.1	100.0	100.4	100.3
Si	0.981	0.979	0.965	0.961	0.966	0.987	0.990	0.992	0.987	0.991
Al	0.001	0.001	0.000	0.001	0.001	0.001	0.001	0.001	0.001	0.001
Mg	1.201	1.315	1.384	1.387	1.315	1.227	1.166	1.141	1.132	1.079
Ca	0.000	0.000	0.000	0.000	0.001	0.001	0.000	0.000	0.000	0.000
Mn	0.031	0.024	0.022	0.020	0.024	0.028	0.031	0.035	0.035	0.038
Fe	0.805	0.703	0.662	0.669	0.728	0.769	0.823	0.840	0.856	0.899
Cation Total	3.019	3.021	3.034	3.039	3.034	3.012	3.010	3.008	3.012	3.009
Fo Number	60	65	68	67	64	61	59	58	57	55

Table IV-2. Electron microprobe line traverse across crystal C2

Location	Spot 1	Spot 2	Spot 3	Spot 4	Spot 5	Spot 6	Spot 7	Spot 8	Spot 9	Spot 10
SiO_2	29.4	30.4	30.7	31.2	31.6	32.4	33.4	34.7	35.1	35.0
Al_2O_3	0.05	0.03	0.03	0.03	0.04	0.04	0.02	0.00	0.01	0.00
MgO	11.7	12.5	13.4	15.5	17.0	18.3	21.2	24.8	26.6	26.1
CaO	0.03	0.01	0.01	0.02	0.02	0.00	0.02	0.02	0.00	0.00
MnO	2.24	2.15	2.15	2.01	1.98	1.98	1.78	1.63	1.59	1.53
FeO	53.8	53.0	52.2	49.9	48.1	46.3	43.3	38.9	37.3	37.3
Oxide Total	97.19	98.09	98.52	98.63	98.78	98.97	99.74	100.1	100.6	99.97
Si	0.955	0.967	0.968	0.968	0.969	0.977	0.981	0.988	0.986	0.990
Al	0.002	0.001	0.001	0.001	0.001	0.002	0.001	0.000	0.000	0.000
Mg	0.565	0.594	0.630	0.714	0.777	0.825	0.928	1.055	1.112	1.100
Ca	0.001	0.000	0.000	0.001	0.001	0.000	0.001	0.001	0.000	0.000
Mn	0.062	0.058	0.057	0.053	0.051	0.051	0.044	0.039	0.038	0.037
Fe	1.459	1.412	1.375	1.294	1.231	1.168	1.063	0.929	0.877	0.883
Cation Total	3.044	3.032	3.032	3.031	3.031	3.022	3.018	3.012	3.014	3.010
Fo Number	28	30	31	36	39	41	47	53	56	55

Table IV-3. Ion microprobe spot analyses across crystal C1

Location	Lithium		Boron		Magnesium		Iron		Mg Normalized Ratios		
	Conc. (ppm)	% error	Conc. (ppm)	% error	Conc. (ppm)	% error	Conc. (ppm)	% error	Fe/Mg	B/Mg	Li/Mg
Spot 1	3.1	4.2%	935.4	1.4%	331325.3	4.8%	8367.7	5.0%	2.5×10^{-2}	2.8×10^{-3}	9.5×10^{-6}
Spot 2	5.3	11.6%	1158.4	2.6%	375548.8	3.4%	8080.9	3.8%	2.2×10^{-2}	3.1×10^{-3}	1.4×10^{-5}
Spot 3	9.2	5.7%	2445.3	3.6%	446649.8	2.3%	8490.1	3.0%	1.9×10^{-2}	5.5×10^{-3}	2.1×10^{-5}
Spot 4	9.1	6.7%	939.3	2.4%	405704.6	2.3%	8959.7	2.9%	2.2×10^{-2}	2.3×10^{-3}	2.2×10^{-5}
Spot 5	5.3	3.3%	842.9	22.6%	371743.3	2.0%	9493.2	3.3%	2.6×10^{-2}	2.3×10^{-3}	1.4×10^{-5}
Spot 6	2.2	0.2%	24687.0	7.4%	279713.2	0.7%	10310.0	2.5%	3.7×10^{-2}	8.8×10^{-2}	7.8×10^{-6}

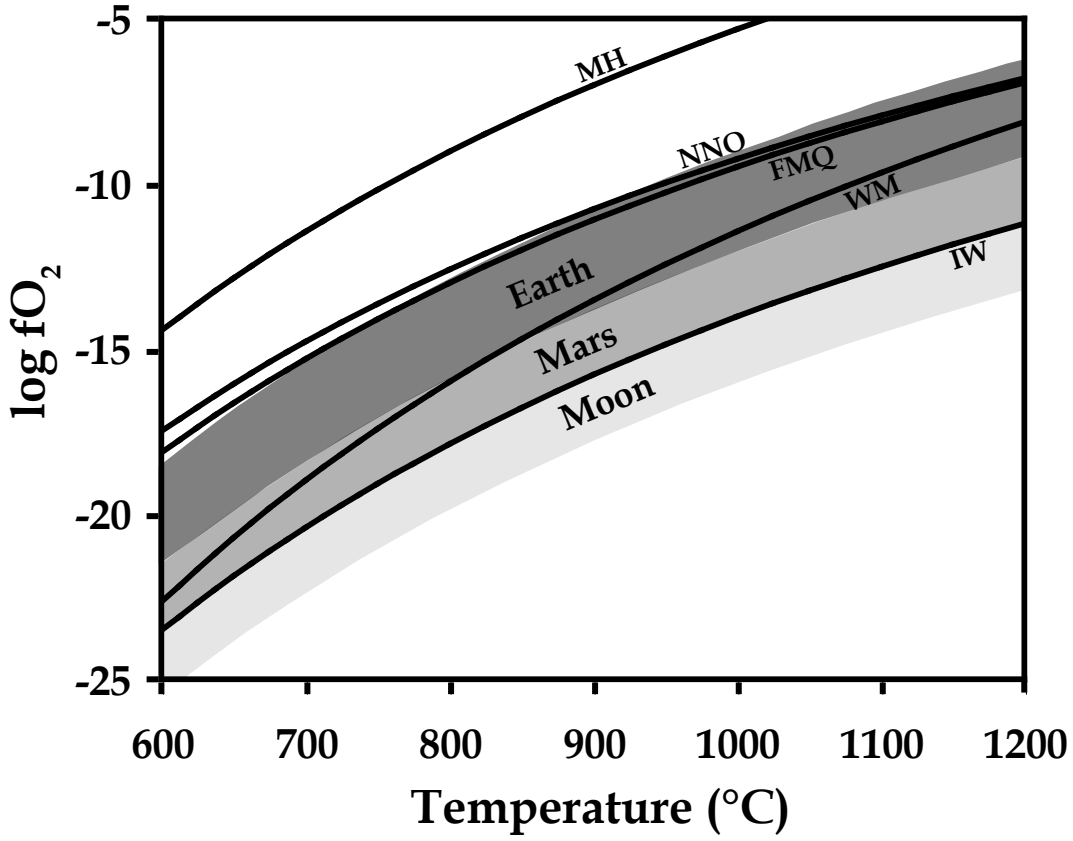

Figure IV-1. Log fO_2 versus temperature diagram showing some common oxygen buffers. Shaded areas represent estimated ranges for the redox conditions for the Moon, Mars, and Earth adapted from (Frost, 1991; Herd, 2008; Wadhwa, 2008). The higher fO_2 conditions within the mantle of the Earth typically restrict the crystallization of olivine to the Mg-rich endmember, while the lower fO_2 conditions in the lunar and martian mantles result in a wider Mg/Fe solid-solution compositional range.

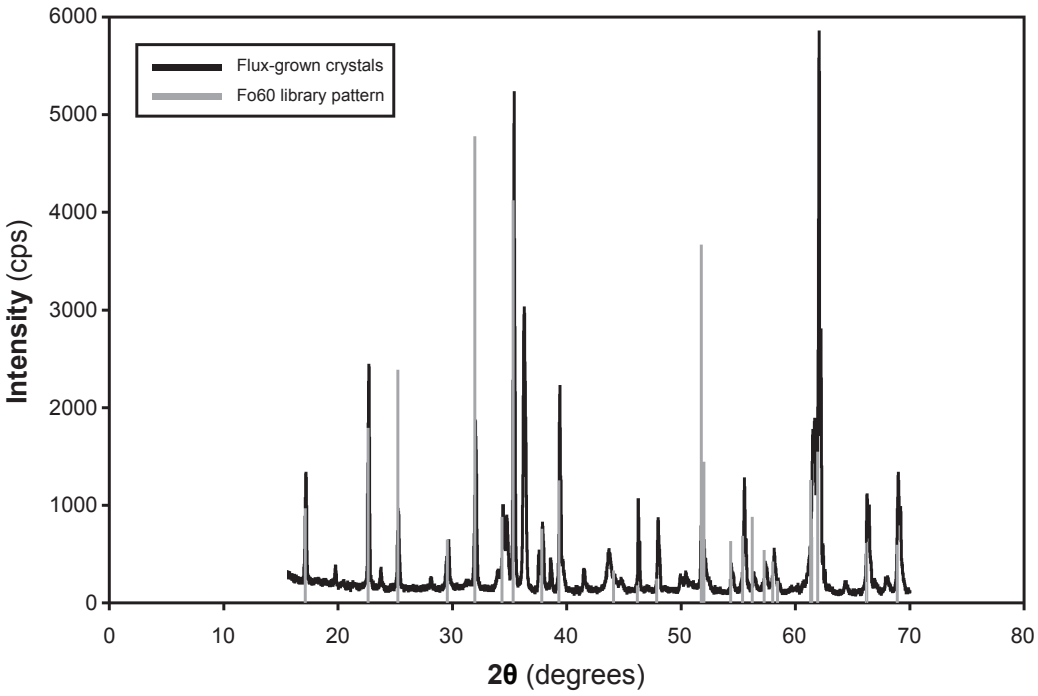

Figure IV-2. X-ray diffraction pattern for flux grown olivine crystals showing an approximate Fo60 ($Mg_{1.2}Fe_{0.8}SiO_4$) bulk composition. A library pattern of a Fo60 olivine is also included for comparison.

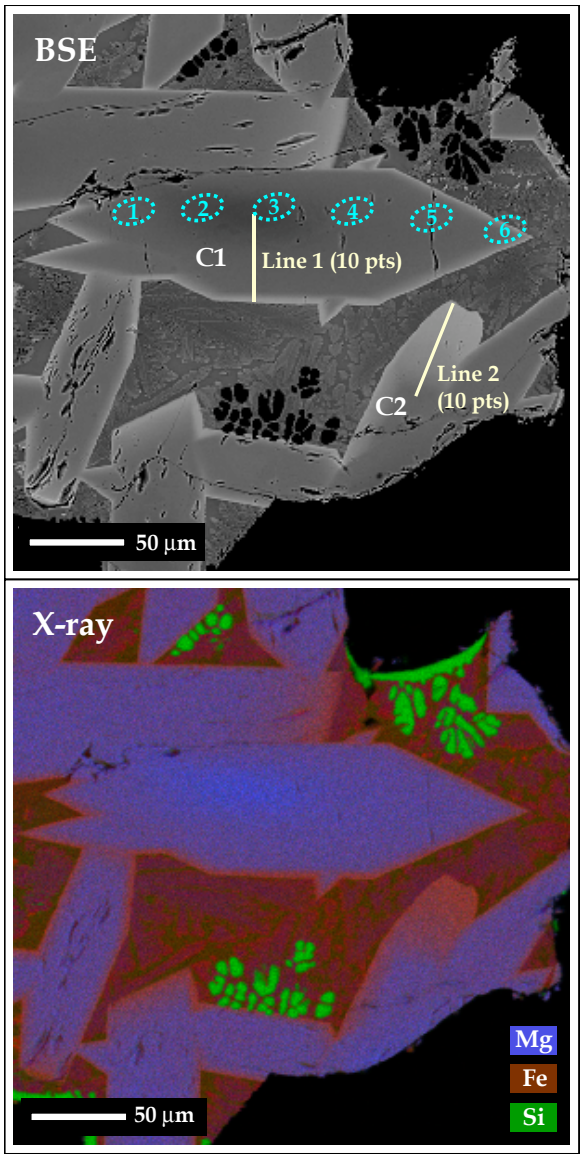

Figure IV-3. BSE and X-ray images of flux grown olivine crystals (C1 and C2). Lines 1 and 2 indicate the location of EMP line traverses. Spots 1-6 indicate the location of SIMS spot analyses. A qualitative view of the X-ray image shows that the olivine crystals are compositionally zoned with Mg-rich (red) cores and Fe-rich (blue) rims.

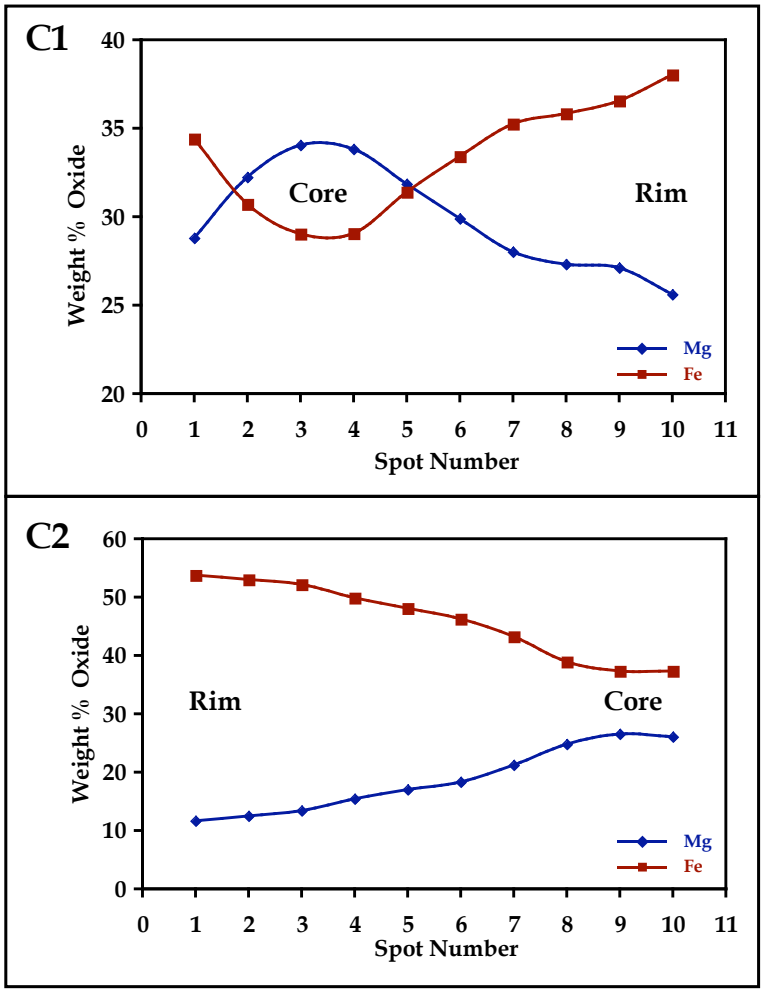

Figure IV-4. Weight percent oxide versus spot number zoning profiles for EMP line traverses across crystals C1 and C2. The profile for crystal C1 gradates from a Mg-rich core (spots 3 & 4) to an Fe-rich rim (spot 10), while the profile for crystal C2 gradates from an Fe-rich rim (spot 1) to a Fe-depleted, Mg-enriched core (spot 10).

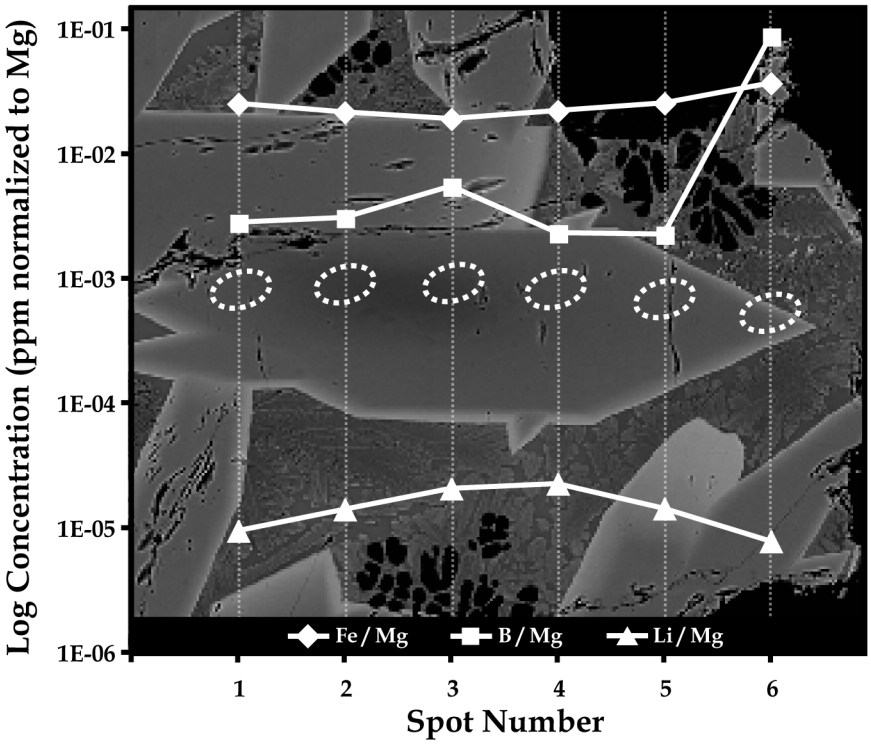

Figure IV-5. Log concentration in ppm normalized to Mg versus spot number for SIMS analyses across crystal C1. The crystal is zoned in Li and B, with an enriched core gradating to depleted rims. The sixth analysis spot shows a marked increase in B due to the analysis overlapping the rim of the crystal and including some matrix material.

Part V.
An Experimental Investigation of Olivine–Fluid Interaction as a function of pH and Surface Area

This part is a reformatted version of a paper, by the same name, to be submitted to Geochemica et Cosmochimica Acta by Michael T. DeAngelis, Theodore C. Labotka, David B. Finkelstein, and David R. Cole.

DeAngelis, M.T., Labotka, T.C., Finkelstein, D.B., and Cole, D.R. Olivine–fluid interaction as a function of pH and surface area. 2011. *To be submitted*.

Abstract

The mineral olivine, $(Mg,Fe)_2SiO_4$, is not thermodynamically stable at low temperature and pressure, and readily dissolves in the presence of water. To investigate this process, we mixed San Carlos olivine powders with low pH (pH 2) solutions of composition 0.005 M H_2SO_4 or 0.01 M HCl at different fluid–mineral ratios, and allowed pH and solution composition to change with continued dissolution over time. The common result from all experiments was an increase in pH from pH 2 to values near pH 10. The shape of pH–log *t* curves show initial exponential-shaped increase from pH 2 to pH 6, limited duration linearity at pH 6, and ending with logarithmic-shaped increase from pH 6 to pH 10. These curves are displaced in time depending on both surface area of the powders and the fluid–mineral ratio of the experiment. Attempts to normalize the data with respect to surface area or fluid–mineral ratio provide mixed results, with some portions of the curves below pH 6 becoming congruent while other portions of the curves above pH 6 do not. Modeling with Geochemist's Workbench (GW) suggest the overall shape of pH–log *t* curves results from the precipitation and dissolution of various mineral species as pH increases. This modeling also suggests that the changes observed represent less than 0.1% reaction progress in the experiments. Powder X-ray diffraction analysis of after experiment suspended material indicates the presence of forsterite only. No other

model-predicted phases (e.g. quartz, talc, antigorite, brucite) have been identified, but model-based calculations indicate that the concentrations of any newly precipitated phases would likely be too low to observe. Calculation of dissolution rate with use of sample weight loss data indicate an average dissolution rate of 3.46×10^{-7} mol/m^{2}s; two orders of magnitude faster than dissolution rates calculated with use of the measured dissolved Mg in solution (1.4×10^{-9} to 1.7×10^{-8} mol/m^{2}s) or diffusion rates values calculated using empirical rate equations (1×10^{-8}–1×10^{-10} mol/m^{2}s). These experiments are intended to be analogous to the natural interaction of olivine with acidic solutions where the time of interaction is limited. The results of this study can be used along with careful examination of naturally weathered samples to help interpret the fluid–mineral interaction history of those samples.

1. Introduction

The physical and chemical weathering of olivine, $(Mg,Fe)_2SiO_4$, has significant impact on chemical cycling on Earth. Olivine is more susceptible to weathering than most other silicate minerals because the divalent cations occupying M1 and M2 octahedral sites between isolated silicon-oxygen tetrahedra are readily released by surface dissolution at low temperature and pressure, particularly at low pH (see Brantley, 2008; Rimstidt et al., in press for discussion).

Many workers have performed experiments to determine the rate of forsterite dissolution under various temperature, pressure, and solution pH conditions (Luce et al., 1972; Sanemasa et al., 1972; Bailey, 1976; Grandstaff, 1978; Eriksson, 1982; Siegel and Pfannkuch, 1984; Blum and Lasaga, 1988; Vanherk et al., 1989; Wogelius and Walther, 1991; Wogelius and Walther, 1992; Jonckbloedt, 1998; Awad et al., 2000; Chen and Brantley, 2000; Pokrovsky and Schott, 2000b; Rosso and Rimstidt, 2000; Oelkers, 2001; Giammar et al., 2005; Hanchen et al., 2006; Olsen, 2007; Olsen and Rimstidt, 2008). Most of these experiments kept the solution buffered at a specific pH value, because the release of divalent cations is coupled with surface protonation that results in a solution pH increase. Rate data from these forsterite dissolution studies have been compiled and compared (Olsen, 2007; Brantley, 2008; Rimstidt et al., in press) and indicate faster dissolution rates at low pH (10^{-8} mol/m^{2}s at pH 2) and slower dissolution rates at high pH (10^{-11} mol/m^{2}s at pH 12). The rate of olivine dissolution has also been found to be temperature dependent, with faster rates of dissolution occurring with increasing temperature (Vanherk et al., 1989; Brady and Walther, 1992; Wogelius and Walther,

1992; Chen and Brantley, 2000; Oelkers, 2001; Hanchen et al., 2006). Activation energies have also been determined from many studies, and the range varies between 25 and 125 kJ/mol (see Hanchen et al., 2006 for review).

Our study focuses on the physical and chemical changes to both solid and solution that result from mixing olivine powders with low pH solutions in non-buffered experiments where both physical and chemical weathering occur simultaneously. The experiments are intended to be analogous to the reaction of olivine in strongly acidic (e.g. acid mine drainage or naturally acidic hydrothermal) environments. These experiments may also have some implications for the reaction of olivine with transient low pH waters on the surface of Mars (Stopar et al., 2006; Hurowitz and McLennan, 2007), though Martian olivine is typically more Fe-rich than the terrestrial starting material used in these experiments.

2. Methods

2.1. Materials

Grains of olivine ($Mg_{1.8}Fe_{0.2}SiO_4$) (Thomas et al., 2008) from San Carlos, Arizona were crushed and sieved into four size groups: 125–250 μm, 250–500 μm, 500–1000 μm, and 1000–2000 μm (hereafter we refer only to the nominal sieve size opening for naming of these different groups, e.g. 125 μm for the 125-250 μm group). The olivine grains were elutriated and dried to remove any superfine, potentially highly reactive material. Solutions used in experiments included 0.005 M H_2SO_4 (pH ≈ 2) and 0.01 M HCl (pH ≈ 2). The fluid–mineral ratio used in these experiments was 1:1, 4:3, or 2:1 measured by

mass (Table V-1). All experiments were performed at room temperature (T_{exp} = 293–298K).

2.2. Experimental techniques

For each experiment, the desired amount of forsterite powder was weighed and placed in a 10 mL Erlenmeyer flask. The solution of interest was weighed to match the fluid–mineral ratio of interest (FR_{exp}), and then the solution was added to the flask. A stir bar and a pH probe were quickly added, and the top of the flask was sealed with Parafilm. The pH was measured and recorded each minute for the duration of each experiment. The total time to complete each experiment varied, but continued until the solution pH reached and maintained a value between pH 9 and 10.

After each experiment was completed, the solution and any suspended materials were poured off of the remaining olivine crystals. The olivine crystals were then dried in a vacuum oven at 50 °C overnight, and the solution was vacuum filtered with a 0.2 μm Teflon filter. The olivine crystals, filtered solutions, and suspended materials were retained for analysis.

2.3. Analytical techniques

All pH measurements were performed using a Thermo Scientific Orion Ross Combination pH electrode (Part #8103BN) attached to a Thermo Orion 920A Benchtop pH Meter connected via RS-232 to a computer running a custom LabView program designed to measure and record pH. The pH meter and electrode were manually calibrated before each experiment using a standard three-pH (pH 4, pH 7, pH 10) solution calibration technique.

Concentrations of magnesium and silicon in solution were determined with a Perkin Elmer 3110 flame emission atomic absorption spectrometer (AA). Mg concentrations were analyzed at 285.2 nm using an air-acetylene flame and a 10 cm burner head, with a linear response over a range from 5 to 500 ppb. Si concentrations were analyzed at 251.6 nm using a nitrous oxide-acetylene flame and a 5 cm burner head, with a linear response over a range from 5 to 150 ppm. Because the concentration of Mg was anticipated to be >200 ppm for each experimental solution sample, each sample was diluted by a factor of ~1000 with deionized water to bring them into the linear range. Conversely, because the concentration of Si was expected to be low for each sample, dilution was not required for these analyses. The concentration value of Mg and Si in samples and standards were determined by an average of three or more analyses per value (see Table V-1).

To examine the surface of olivine powders after experiment, 3D back-scattered electron (BSE) images were collected using a Hitachi S-3400 Variable Pressure Scanning Electron Microscope (SEM). The SEM had an accelerating voltage potential of 20 kV and working distance of 12 mm. Images were collected at a range of magnifications.

After the suspended material was dried and filtered, it was examined by powder X-ray diffraction (PXRD) using a PANalytical X'pert PRO 2-circle X-ray diffractometer with Cu $K\alpha_{1,2}$ incident radiation (λ = 1.54 Å) operating at 45 keV and 40 mA. PXRD data were collected at room temperature between 15 and 100° 2θ with a step size of 0.02° and count time of 100 s per step. PXRD pattern analysis and Rietveld structure refinements were performed using the HighScore Plus program from PANalytical.

3. Results

3.1. Solution pH over time

The solution pH of all experiments, regardless of olivine surface area or fluid–mineral ratio, immediately increased upon mixing olivine with either 0.005 M H_2SO_4 or 0.01 M HCl. The starting pH of each experiment was near pH 2 and continued to rise until reaching a maximum value near pH 10 before beginning to drop slightly in pH toward experiment termination. The general shape of pH–log *t* curves are similar for all experiments, with initial exponential-shaped change between pH 2 and pH 6, limited duration linearity at pH 6, and ending with logarithmic-shaped change between pH 6 and pH 10 (Figures V-1–V-3). The amount of time required to proceed to higher pH values varied, resulting in curves with similar shapes displaced in time. Comparison of experiments having fixed a fluid–mineral ratio but different powder sizes showed that overall pH increase was slower for low surface area olivine and faster for high surface area olivine (Figure V-1). At fixed grain size but different fluid–mineral ratios, the pH increase was delayed for higher fluid–mineral ratios (2:1) compared with lower fluid–mineral ratios (4:3 and 1:1) (Figure V-2). Experiments for which both fluid–mineral ratio and powder size were constant but the acid type was varied had almost identical pH versus log time curves (Figure V-3).

3.2. Dissolution and weathering of olivine powders

The olivine powders used in this study were crushed from larger crystals (>2 mm diameter) to acquire a range of smaller sizes. This crushing process produced smaller crystals with sharp edges and corners. Because the olivine and solution were stirred throughout the duration of the experiment, these sharp edges and corners were abraded by

constant contact with other olivine crystals. SEM images of after-experiment material show the results of this abrasion, which is characterized by pitting and rounding of edges and corners (Figure V-4).

Weathering of olivine surfaces also resulted in the generation of ultrafine powders that either were suspended in solution or floated to the top of solution. This suspended material was filtered, dried, and analyzed by PXRD to determine composition (Figure V-5). Comparison with library spectra (PDF# 96-900-0540; Hazen, 1976) and Rietveld structure analysis from matched patterns confirmed the presence of forsteritic olivine only.

The concentration of Mg and Si in solution after experiment was measured using the AA (see Table V-1). Mg concentrations ranged from 229–525 ppm and Si concentration ranged from 15–42 ppm. The disparity in concentration between Mg and Si in all experiments may reflect the result of the chemical dissolution processes described earlier that initially remove Mg over Si from the olivine surface at low pH. The concentration of Mg, in particular, is observed to vary with grain size and fluid–mineral ratio (Figure V-6). The histogram in Figure V-6 shows that final Mg concentrations are generally higher for larger grain sizes and lower for smaller grain sizes. There is also variation with fluid–mineral ratio, observed for the 500 μm sieve size experiments, where the largest fluid–mineral ratio (2:1) has the lowest Mg concentration and the smaller fluid–mineral ratio (1:1) experiments have the highest concentration of Mg. This relationship with fluid-mineral ratio is somewhat expected, since the smallest fluid–mineral ratio is the least diluted of the experiments. However, the relationship with grain size (i.e. surface area) is not understood. Perhaps physical abrasion of olivine grains was

a dominant process for the larger grain size experiments, and the result was more fine grained pieces of olivine, but less Mg^{2+} cations, in solution. Grinding of the samples during sample preparation may also have produced more high energy edges and steps that made these grains more susceptible to surface dissolution.

4. Discussion

4.1. Shape of pH–log *t* curves

The changes in shape of the pH–log *t* curves is the result of competing processes. Because no components are being added or removed during experiment, the observed overall pH increase must be the result of relocating H^+ ions in solution to either olivine or newly formed phases. Protonation of vacated octahedral sites has been previously observed in olivine dissolution studies (see Brantley, 2008 for discussion), and is the most likely explanation for the change in pH seen here. The measured concentration increases of Mg^{2+} in solution indicate that dissolution processes are occurring. This removal of Mg^{2+} from olivine surfaces provides the needed vacant octahedral sites necessary for protonation and pH increase.

If removal of one Mg^{2+} ion by dissolution and filling the vacant octahedral site with two H^+ ions by protonation was the only process occurring, the resultant pH–*t* curves would not be expected to have multiple inflections and changes in direction. Previous studies of olivine dissolution show a significant inflection in the slope of dissolution rate–pH curves near pH 6, and ascribe this inflection in slope to changes in reaction mechanism where Si^{4+} begins to be preferentially removed over Mg^{2+} at higher pH values (Pokrovsky and Schott, 2000a; Pokrovsky and Schott, 2000b; Olsen, 2007;

Rimstidt et al., in press). This change in reaction mechanism may be, in part, an explanation for the major change in curve shape observed in all of our experiments near pH 6. However, the low concentration of Si relative to Mg in solution again indicates that dissolution coupled with protonation is not the only process occurring here.

The presence of suspended material at the end of experiment may be the missing variable. Precipitation of newly formed mineral phases may help to explain the shapes of these pH curves. However, PXRD analysis of this suspended material detected no new mineral phases. Still, these new mineral phases may exist but may be at concentrations too low to be detectable by PXRD. The possibility of low concentrations of newly formed mineral phases is discussed in greater detail in the geochemical modeling section below.

4.2. Normalizing the pH–log *t* curves

Inspection of the pH–log *t* curves in Figures V-1–V-3 suggests that the curves are similar in shape but displaced in time. The spacing between the curves may depend on surface area of the olivine powders or on the fluid–mineral ratio of the experiments. To investigate these possibilities, the data must be normalized to surface area and fluid–mineral ratio and then re-plotted. After normalization, the curves should become congruent if the spacing of the curves depends on either surface area or fluid–mineral ratio.

The geometric surface areas of olivine powders used in this study were calculated using the method first described by Tester et al. (1994), used by Brantley and Mellott (2000) for determination of surface areas of silicate minerals in general, and later

specifically applied to forsterite powders by Olsen (2007) and Rimstidt et al. (in press). The equation that describes the geometric surface area calculation is the following:

$$A_{geo} = \frac{6V_m}{W_m D_{avg}} \quad (1)$$

where A_{geo} is the geometric surface area in m^2/g, V_m is the molar volume of forsterite in m^3/mol (Robie and Hemingway, 1995), and W_m is the molar mass of forsterite in g/mol. Each experiment used a range of grain sizes, so an area-averaged diameter was calculated using the following equation:

$$D_{avg} = \frac{D_{\max} - D_{\min}}{\ln\left(\frac{D_{\max}}{D_{\min}}\right)} \quad (2)$$

where D_{avg} is the area-averaged diameter, D_{max} is the maximum grain diameter, and D_{min} is the minimum grain diameter (Tester et al., 1994). These equations assume that the grains are approximately spherical in shape and that there is an equal population density distribution between $D_{\min}$ and $D_{\max}$ within each group. The calculated D_{avg} and A_{geo} values for each of the four sieve ranges are shown in Table V-2, and the total surface area (A_{tot}) of olivine powders used in each experiment is shown in Table V-3. These A_{tot} values were then multiplied by the time values in each experiment, divided by the fluid-mineral ratio for each experiment (hereafter referred to as 'normalized time'), and the resultant data plotted versus pH (Figure V-5).

Normalization of experimental data in which the fluid–mineral ratio was constant but powder size varied resulted in curves that overlay each other (except SApH06) at pH < 6, but then had changing slopes grouped by powder size at pH > 6 (Figure V-7).

Experiment SApH06, which has the largest powder size at 1000 μm, has a different normalized curve than the rest of the constant fluid–mineral ratio experiments. Interestingly, the plotted curve from this experiment has a flat portion between pH 4 and pH 6 that is not observed in the other constant fluid–mineral ratio experiments. This suggests that despite using the same starting material, same solution, and same fluid–mineral ratio, the difference in surface areas between the ≤ 500 μ m and 1000 μm experiments resulted in an observable change in dissolution mechanism. A change in dissolution mechanism related to surface area is also apparent at pH > 6, where the largest surface area powders (125 μm experiment) appear to take more time to increase in pH than smaller surface area powders (250 μm experiments next slowest followed by 500 μm experiments). These results seem counterintuitive, given the available surface area for dissolution in the small starting powder size experiments, but this may be the latent result of more prominent physical abrasion in the larger starting powder size experiments producing both ultrafine material and as yet unreacted surfaces.

Plotting the normalized data from experiments with constant grain size and different fluid–mineral ratios had very slight difference from the original data (Figure V-8). The curves with lower fluid–mineral ratios (4:3 and 1:1) became more overlaid in pH–log *t* plots. However, the SApH02 experiment with a higher fluid–mineral ratio (2:1) had a very different curve than the lower fluid–mineral ratios. This again suggests that there is some fundamental difference in the dissolution response when a higher fluid proportion is used, or it may be that the response is no different except that is more observable for these experiments compared with the lower fluid–mineral ratio experiments.

Normalized data from experiments where both fluid–mineral ratio and powder size were constant but the acid type was varied had almost identical pH versus log time curves (Figure V-9). This result is the same from the plot using the original data, and confirms that the change in pH with time is independent of the proton source (HCl versus H_2SO_4), as long as the activity of H^+ in the starting solution is the same.

4.3. Geochemical modeling

To help interpret the results of our experiments, a series of reaction path calculations were performed with Geochemist's Workbench Release 7.0 (GW). Starting conditions for the GW model were the same as experiment SApH03 (see Table V-1). The oxide composition of olivine used in the model was from the electron probe microanalysis of San Carlos olivine described in Thomas et al. (2008; Table 1) and was set as reactants to be titrated into the system. The intended purpose of the modeling was to predict changes to the concentrations of Mg^{2+}, SiO_2 (aq), and OH^- species in solution, potential minerals precipitated and consumed, and overall pH as the interaction of H_2SO_4 and olivine powder progressed toward complete equilibration (Figure V-10).

The first observation made from the model was that the pH should continue to increase to final value near pH 12 if all of the olivine were able to equilibrate with all the H_2SO_4 solution (see inset in Figure V-10). Since all the experiments showed a maximum pH near 10, this indicates that the duration of the experiments was not sufficient to bring the system close to equilibrium. Examination of the modeled pH change for very limited reaction progress (<0.01) showed a pH change curve similar in shape to the pH versus log time curve from experiments. This stepped shaped curve can be correlated with increases in aqueous OH^-, decreases in aqueous SiO_2, and mineral reactions that both precipitate

and consume different mineral phases (quartz, talc, antigorite, brucite) as reaction proceeds. These steps have been divided into four zones labeled A, B, C, and D, and their corresponding mineral reactions are listed in Table V-4.

Though it may be difficult to precisely correlate reaction progress in the model with reaction time in the SApH03 experiment, the disparity of measured concentrations of Mg (452 ppm) and Si (19 ppm) and a final experiment pH near 10 suggest that the termination of the experiment may have occurred near the step from antigorite only to antigorite and brucite precipitation at approximately 0.0025% reaction progress (see middle panel in Figure V-10). At this point in the experiment, any quartz or talc that previously precipitated had been consumed in the formation of antigorite. Calculation of antigorite concentration at 0.0025% reaction progress yields a results of slightly less than 3 mg of antigorite. Given that both the model and experiment used 7 g of olivine total, it is unlikely that detection of this small amount of antigorite by PXRD would be possible. Instead, the pH curves in both the experiments and model must be used as a proxy for mineralization that is undetectable by more macro-scale analytical techniques.

The sharp steps in the reaction model versus smoother curves in the experimental data show the limitations of the model to completely reflect experimental results. The curvature of pH versus log time curves likely reflects the affect of various kinetic parameters (e.g. activation energies, changing dissolution rates, etc.) that have not been fully incorporated into the model. Still, modeling coupled with these experiments has confirmed that the activity of H^+ changes greatly, and suggests that the various inflections in experiment curves may result from the production and consumption of new mineral species.

4.4. Dissolution rates

Olsen (2007) and Rimstidt et al. (in press) have compiled data from 22 separate studies of low temperature olivine dissolution and have used those data in multiple linear regression models to derive empirical olivine dissolution rate expressions as a function of surface area, temperature ($0° < T < 150°C$) and pH (1–12). Upon recognizing a change in the slope of the regression curves near pH 5.6 (for 25°C data), they established two rate law expressions; one for dissolution at pH < 5.6 and one for dissolution at pH > 5.6 (Rimstidt et al., in press). The observed change in slope at this pH is suggested to reflect a change in reaction mechanism (Olsen, 2007; Rimstidt et al., in press), and may correspond with a change in the preferential release of Mg at low pH to release of Si at high pH (Pokrovsky and Schott, 2000a; Olsen, 2007).

Our data agree with a major shift in the pH versus time curves near pH 6. However, the non-linearity in the shape of the pH–log *t* curves with increasing pH suggest that the changes affecting both the solids and solutions in our experiments are due to factors in addition to dissolution. The mass of starting olivine at the beginning of experiment and the mass of non-suspended olivine at the end of experiment were measured and then plotted versus normalized time (Figure V-11). The slopes of these curves provide an average rate of olivine removal during the experiments with an average value of 3.46×10^{-7} (1.81×10^{-7}) mol/m^{2}s. This rate is at least two to three orders of magnitude faster than what would be expected for removal by dissolution only (Brantley, 2008; Rimstidt et al., in press).

The amount of Mg in solution may be a better proxy for determining olivine dissolution rate. If the Mg in solution represents the amount of dissolution that has occurred, a dissolution rate can be calculated by converting the concentration to moles and dividing the amount by the total surface area of the samples and the amount of time per experiment (Table V-5). The rate values determined by this method range from 1.4×10^{-9} to 1.7×10^{-8} mol/m^{2}s. These values are slower than those determined by the weight loss method described above, but are closer to the values for dissolution rate (10^{-8}–10^{-10} mol/m^{2}s) the empirical rate models of Rimstidt et al. (in press) calculate for the pH range of these experiments.

The agreement of the solution and empirical rate model rates suggest that the faster dissolution rates determined by weight loss are incorrect and actually reflect more Mg loss than can be accounted for by dissolution only. The likely location of this missing Mg is the olivine in the suspended material identified by X-ray diffraction, and suggests that the sample weight losses may have resulted from a combination of physical abrasion and chemical dissolution.

4.5. Implications

The weathering of olivine is a complex combination of many process, all of which occur simultaneously but to varying degrees in natural environments. At low temperatures and pressures, dissolution of olivine surfaces appears to be the primary chemical response to interaction with fluids. In semi-closed system environments where fluids are not completely transient, there may also be some amount of protonation of olivine surfaces. In the more closed system environments found in nature where finite amounts of material react with finite amounts of fluid, these processes of dissolution,

protonation, and solution precipitation are in constant competition. The experiments performed were analogous to this last type of environment, and observations and modeling indicated that all three processes had occurred. The measure of pH in these experiments is a more sensitive measure of reaction progress than identification of secondary phases, because at the limited amount of reaction progress of these experiments the amount of precipitated phases is predicted to be very low. The pH increase in these experiments result in slower dissolution rate, and the mechanism of dissolution changes from primary Mg dissolution at low pH to primary Si dissolution at higher pH. The chemical responses observed in these experiments to different starting solution pH, fluid–mineral ratio, and surface areas can be used along with careful analytical observations of naturally weathered olivine to provide a way to interpret and understand its history of fluid–mineral interactions.

Acknowledgments

This manuscript is a portion of M.T. DeAngelis' dissertation work at the University of Tennessee, Knoxville. Many thanks to Kinga Unocic and Larry Walker at Oak Ridge National Laboratory's SHaRE User Facility for help with SEM analyses, Leslie Wilson with AA analyses, and Juske Horita, Larry Anovitz, and Jorgen Rosenqvist for help with experiment preparation. Special thanks to Dave Wesolowski and other members of the Geochemistry and Interfacial Sciences group at Oak Ridge National Laboratory for their support of this research. This research was supported in part by Oak Ridge National Laboratory's SHaRE User Facility, which is sponsored by the Scientific User Facilities Division, Office of Basic Energy Sciences, U.S. Department of Energy. Funding for this

work was provided by the Division of Chemical Sciences, Geosciences, and Biosciences, Office of Basic Energy Sciences, U.S. Department of Energy. Oak Ridge National Laboratory is managed and operated by UT-Battelle for the U.S. Department of Energy under contract DE-AC05-00OR22725.

References Cited

Awad, A., van Groos, A. F. K., and Guggenheim, S. (2000) Forsteritic olivine: Effect of crystallographic direction on dissolution kinetics. *Geochimica et Cosmochimica Acta* **64**, 1765-1772.

Bailey, A. (1976) Effects of temperature on the reaction of silicates with aqueous solutions in the low temperature range. In: Cadek, J. and Paces, T. Eds.*Proceedings of the International Symposium on Water-Rock Interaction*. Geological Survey Prague, Prague.

Blum, A. and Lasaga, A. (1988) Role of Surface Speciation in the Low-Temperature Dissolution of Minerals. *Nature* **331**, 431-433.

Brady, P. V. and Walther, J. V. (1992) Surface-Chemistry and Silicate Dissolution at Elevated-Temperatures. *American Journal of Science* **292**, 639-658.

Brantley, S. (2008) Kinetics of mineral dissolution. In: Brantley, S., Kubicki, J. D., and White, A. F. Eds.*The Kinetics of Water-Rock Interactions*. Springer, New York.

Brantley, S. L. and Mellott, N. P. (2000) Surface area and porosity of primary silicate minerals. *American Mineralogist* **85**, 1767-1783.

Chen, Y. and Brantley, S. L. (2000) Dissolution of forsteritic olivine at 65 degrees C and $2 < pH < 5$. *Chemical Geology* **165**, 267-281.

Eriksson, E. (1982) On the dissolution rate of forsterite in aqueous solutions. *Vatten* **38**, 409-415.

Giammar, D. E., Bruant, R. G., and Peters, C. A. (2005) Forsterite dissolution and magnesite precipitation at conditions relevant for deep saline aquifer storage and sequestration of carbon dioxide. *Chemical Geology* **217**, 257-276.

Grandstaff, D. E. (1978) Changes in Surface-Area and Morphology and Mechanism of Forsterite Dissolution. *Geochimica et Cosmochimica Acta* **42**, 1899-1901.

Hanchen, M., Prigiobbe, V., Storti, G., Seward, T. M., and Mazzotti, M. (2006) Dissolution kinetics of fosteritic olivine at 90–150 °C including effects of the presence of CO_2. *Geochimica et Cosmochimica Acta* **70**, 4403-4416.

Hazen, R. M. (1976) Effects of temperature and pressure on the crystal structure of forsterite. *American Mineralogist*, 1280-1293.

Hurowitz, J. A. and McLennan, S. M. (2007) A similar to 3.5 Ga record of water-limited, acidic weathering conditions on Mars. *Earth and Planetary Science Letters* **260**, 432-443.

Jonckbloedt, R. C. L. (1998) Olivine dissolution in sulphuric acid at elevated temperatures - implications for the olivine process, an alternative waste acid neutralizing process. *Journal of Geochemical Exploration* **62**, 337-346.

Luce, R. W., Bartlett, R. W., and Parks, G. A. (1972) Dissolution Kinetics of Magnesium Silicates. *Geochimica et Cosmochimica Acta* **36**, 35-50.

Oelkers, E. H. (2001) An experimental study of forsterite dissolution rates as a function of temperature and aqueous Mg and Si concentrations. *Chemical Geology* **175**, 485-494.

Olsen, A. A. (2007) Forsterite dissolution kinetics: applications and implications for chemical weathering. Dissertation, Virginia Polytechnic Institute and State University.

Olsen, A. A. and Rimstidt, J. D. (2008) Oxalate-promoted forsterite dissolution at low pH. *Geochimica et Cosmochimica Acta* **72**, 1758-1766.

Pokrovsky, O. S. and Schott, J. (2000a) Forsterite surface composition in aqueous solutions: A combined potentiometric, electrokinetic, and spectroscopic approach. *Geochimica et Cosmochimica Acta* **64**, 3299-3312.

Pokrovsky, O. S. and Schott, J. (2000b) Kinetics and mechanism of forsterite dissolution at 25 degrees C and pH from 1 to 12. *Geochimica et Cosmochimica Acta* **64**, 3313-3325.

Rimstidt, J. D., Brantley, S., and Olsen, A. A. (in press) Systematic review of forsterite dissolution rate data. *Geochimica et Cosmochimica Acta*.

Robie, R. A. and Hemingway, B. S. (1995) *Thermodynamic Properties of Minerals and Related Substances at 298.15 K and 1 Bar (10^5 Pascals) Pressure and at Higher Temperatures*. U.S. Geological Survey, Washington D.C.

Rosso, J. J. and Rimstidt, J. D. (2000) A high resolution study of forsterite dissolution rates. *Geochimica et Cosmochimica Acta* **64**, 797-811.

Sanemasa, I., Yoshida, M., and Ozawa, T. (1972) Dissolution of Olivine in Aqueous-Solutions of Inorganic Acids. *Bulletin of the Chemical Society of Japan* **45**, 1741-1746.

Siegel, D. I. and Pfannkuch, H. O. (1984) Silicate Mineral Dissolution at pH 4 and near Standard Temperature and Pressure. *Geochimica et Cosmochimica Acta* **48**, 197-201.

Stopar, J. D., Taylor, G. J., Hamilton, V. E., and Browning, L. (2006) Kinetic model of olivine dissolution and extent of aqueous alteration on Mars. *Geochimica et Cosmochimica Acta* **70**, 6136-6152.

Tester, J. W., Worley, W. G., Robinson, B. A., Grigsby, C. O., and Feerer, J. L. (1994) Correlating quartz dissolution kinetics in pure water from 25 to 625°C. *Geochimica et Cosmochimica Acta* **58**, 2407-2420.

Thomas, J. B., Cherniak, D. J., and Watson, E. B. (2008) Lattice diffusion and solubility of argon in forsterite, enstatite, quartz and corundum. *Chemical Geology* **253**, 1-22.

Vanherk, J., Pietersen, H. S., and Schuiling, R. D. (1989) Neutralization of Industrial-Waste Acids with Olivine - the Dissolution of Forsteritic Olivine at 40–70 °C. *Chemical Geology* **76**, 341-352.

Wogelius, R. A. and Walther, J. V. (1991) Olivine Dissolution at 25 °C - Effects of pH, CO_2, and Organic-Acids. *Geochimica et Cosmochimica Acta* **55**, 943-954.

Wogelius, R. A. and Walther, J. V. (1992) Olivine Dissolution Kinetics at near-Surface Conditions. *Chemical Geology* **97**, 101-112.

Appendix V

Table V-1. Experimental data

Name	Starting material	Sieve size	Starting fluid	Duration	Initial sample weight	Final sample weight	Initial fluid weight	Fluid:mineral ratio	Initial fluid pH	Final fluid pH	Mg conc. in fluid after experiment	Si conc. in fluid after experiment
		(um)		(min)	(g)	(g)	(g)	(by mass)			(ppm)	(ppm)
SApH02	San Carlos Olivine	500	0.005 M H_2SO_4	22684	3.5587	3.3193	7.0136	1.971	1.793	8.984	247	42
SApH03	San Carlos Olivine	500	0.005 M H_2SO_4	7162	7.0214	6.3580	7.0062	0.998	2.033	9.988	452	19
SApH04	San Carlos Olivine	500	0.005 M H_2SO_4	9867	5.2510	4.7914	7.0032	1.334	1.880	9.822	291	15
SApH05	San Carlos Olivine	500	0.005 M H_2SO_4	9767	4.9997	4.5473	5.0023	1.001	1.913	9.453	525	19
SApH06	San Carlos Olivine	1000	0.005 M H_2SO_4	31383	7.0218	6.7306	7.0047	0.998	1.845	9.762	523	15
SApH07*	San Carlos Olivine	250	0.005 M H_2SO_4	5093	5.0502	-	5.0499	1.000	2.026	9.756	-	-
SApH08	San Carlos Olivine	125	0.005 M H_2SO_4	11510	7.0103	5.4128	7.0218	1.002	2.018	10.419	245	15
SApH09**	San Carlos Olivine	250	0.005 M H_2SO_4	9890	7.0068	-	7.0619	1.008	2.030	9.929	229	15
SApH10**	San Carlos Olivine	250	0.01 M HCl	18477	7.2463	-	7.2568	1.001	2.045	9.880	239	15

* pH electrode broken during SApH07 experiment; final weights, Mg conc. and Si conc. not collected

** final weights not recorded

Table V-2. Calculated geometric surface areas for starting material

Nominal sieve opening (μm)	D_{min} (μm)	D_{max} (μm)	D_{avg} (μm)	A_{geo} (m^2/g)
125	125	250	180.3	0.0103
250	250	500	360.7	0.0052
500	500	1000	721.3	0.0026
1000	1000	2000	1442.7	0.0013

Table V-3. Experimental surface areas

Name	Nominal sieve opening	Initial sample weight	Geometric surface area (A_{geo})	Total surface area (A_{tot})
	(µm)	(g)	(m^2/g)	(m^2)
SApH02	500	3.5587	0.0026	0.0093
SApH03	500	7.0214	0.0026	0.0183
SApH04	500	5.2510	0.0026	0.0137
SApH05	500	4.9997	0.0026	0.0130
SApH06	1000	7.0218	0.0013	0.0091
SApH07	250	5.0502	0.0052	0.0263
SApH08	125	7.0103	0.0103	0.0722
SApH09	250	7.0068	0.0052	0.0364
SApH10	250	7.2463	0.0052	0.0377

Table V-4. Modeled $MgO+SiO_2+H_2O$ reactions for San Carlos olivine and H_2SO_4 (0.005M) at 20 °C, reaction progress < 0.1

Zone	Modeled reaction*
A	$Mg_2SiO_4 + 4\ H^+ = 2\ H_2O + 2\ Mg^{2+} + SiO_2$
B	$3\ Mg_2SiO_4 + 2\ H_2O + 5\ SiO_2 = 2\ Mg_3Si_4O_{10}(OH)_2$
C	$2\ Mg_2SiO_4 + H_2O + 2\ H^+ = Mg^{2+} + Mg_3Si_2O_5(OH)_4$
D	$2\ Mg_2SiO_4 + 3\ H_2O = Mg(OH)_2 + Mg_3Si_2O_5(OH)_4$

* Mg_2SiO_4 - forsterite; SiO_2 - quartz; $Mg_3Si_4O_{10}(OH)_2$ - talc; $Mg(OH)_2$ - brucite; $Mg_3Si_2O_5(OH)_4$ - antigorite

Table V-5. Dissolution rate determination from Mg concentration in fluid

Experiment name	Mg conc. in fluid after experiment (ppm)	Initial fluid weight (g)	Total dissolved Mg in experiment (10^{-5} mol)	Experiment duration (10^{6} s)	Mass flux (10^{-11} mol/s)	Total surface area (A_{tot}) (m^2)	Dissolution rate (10^{-9} mol/m^2s)
SApH02	247	7.0136	7.2	13.6	5.3	0.0093	5.7
SApH03	452	7.0062	13.2	4.3	30.7	0.0183	16.8
SApH04	291	7.0032	8.5	5.9	14.3	0.0137	10.5
SApH05	525	5.0023	11.0	5.9	18.7	0.0130	14.4
SApH06	523	7.0047	15.2	18.8	8.1	0.0091	8.9
SApH08	245	7.0218	7.2	6.9	10.4	0.0722	1.4
SApH09	229	7.0619	6.7	5.9	11.3	0.0364	3.1
SApH10	239	7.2568	7.2	11.1	6.5	0.0377	1.7

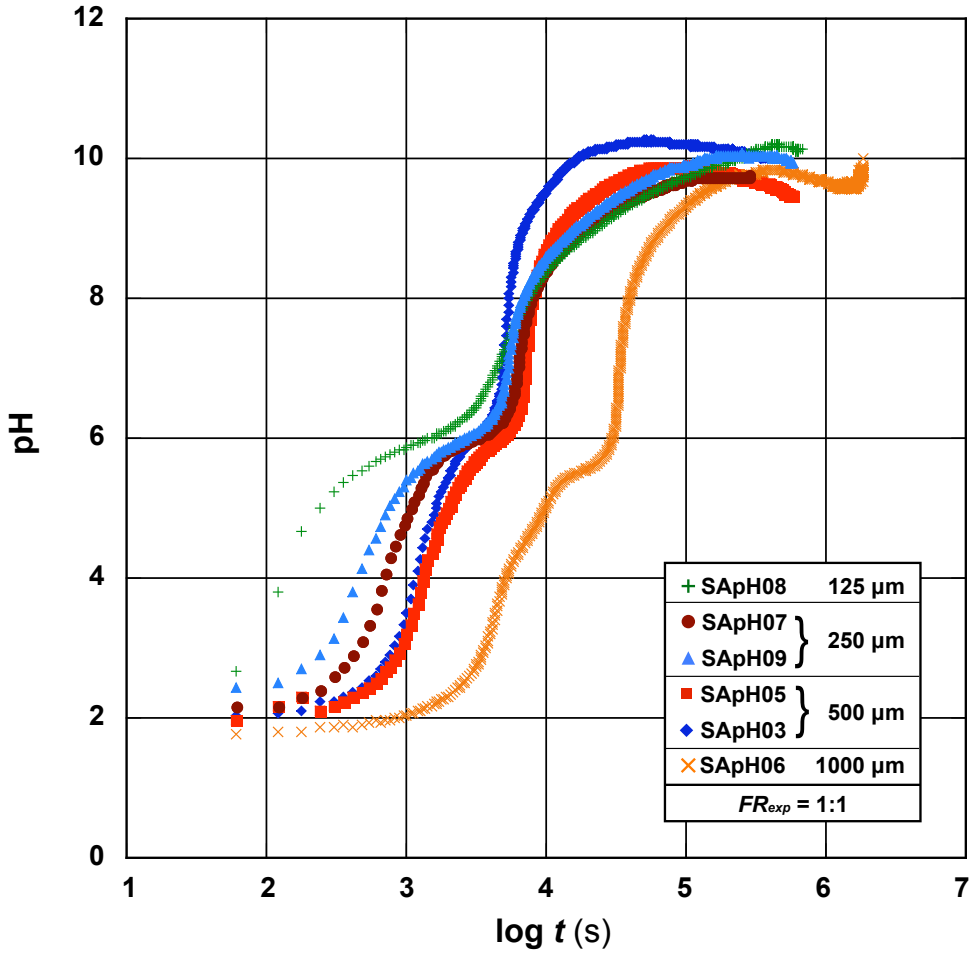

Figure V-1. Plot of pH versus log time for constant fluid–mineral ratio (1:1) and starting solution (0.005 M H_2SO_4) with different powder sizes.

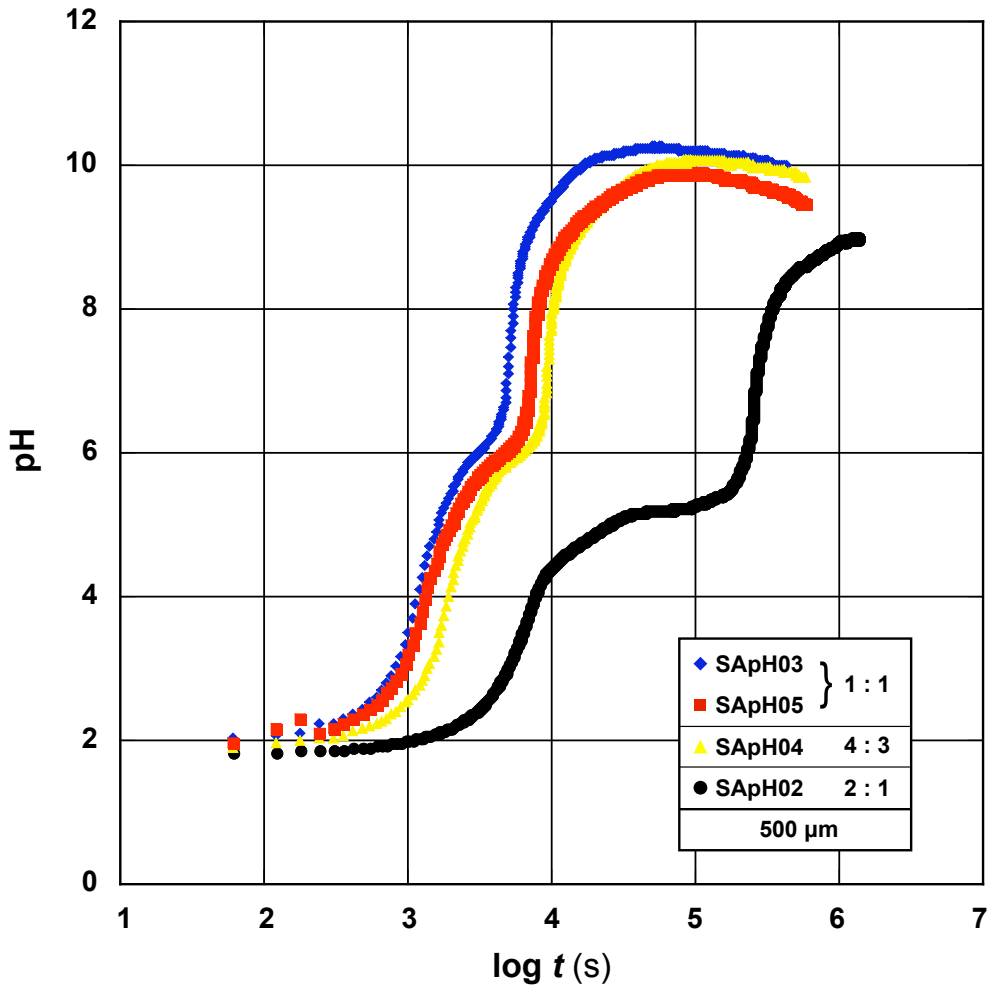

Figure V-2. Plot of pH versus log time for constant powder size (500 µ m) and starting solution (0.005 M H_2SO_4) with different fluid–mineral ratios.

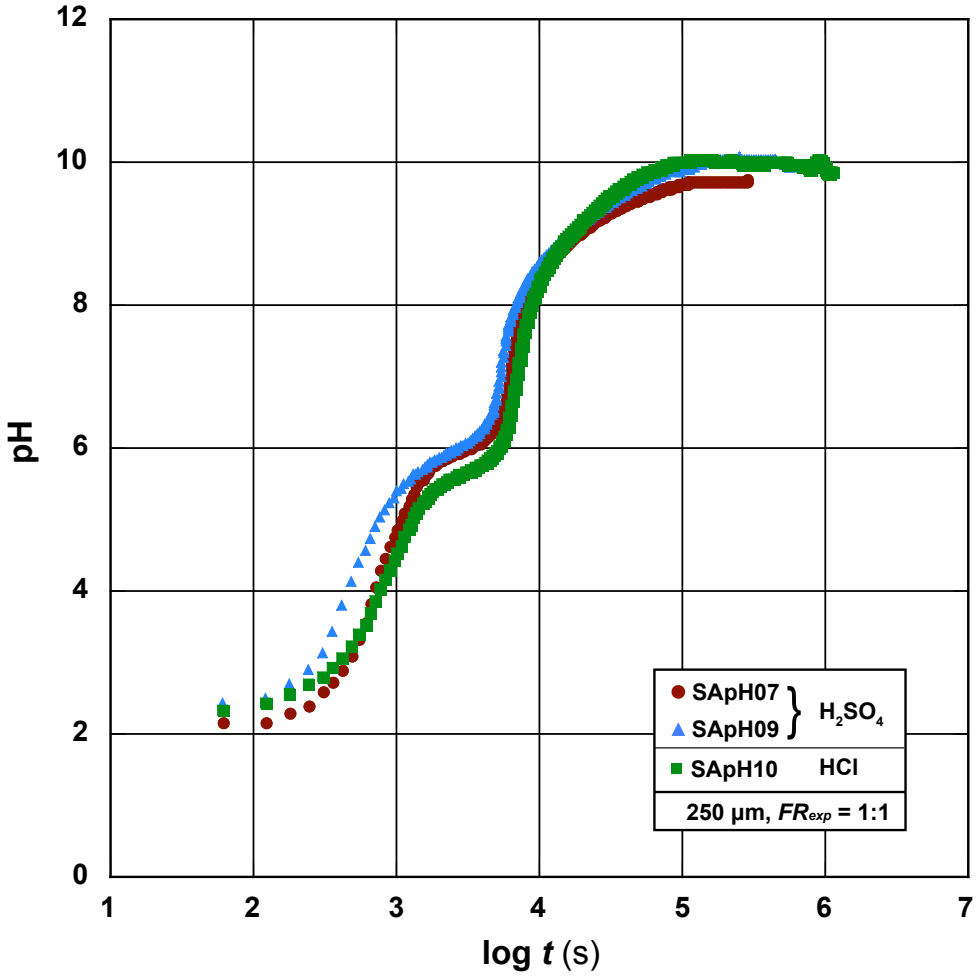

Figure V-3. Plot of pH versus log time for constant powder size (500 µ m) and fluid–mineral ratio (1:1) with different starting solutions.

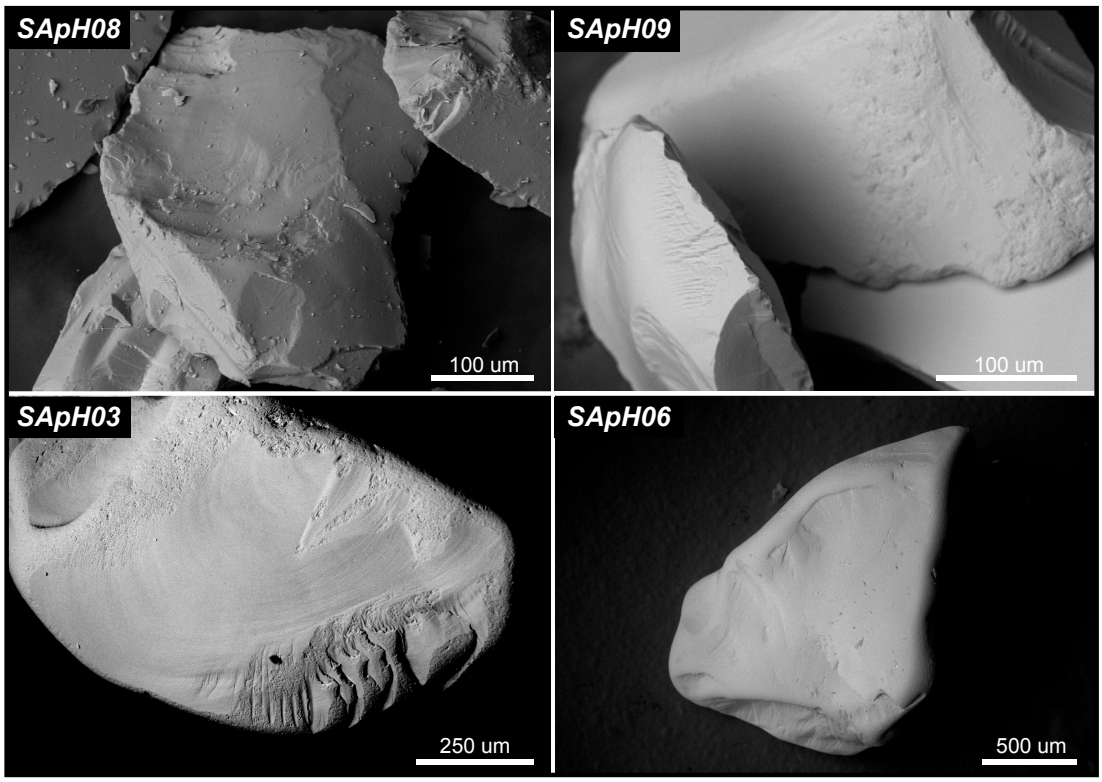

Figure V-4. SEM images of olivine powders after experiment showing rounded and pitted corners for larger powder sizes. Experiments include: SApH08 (125 µm), SApH09 (250 µm), SApH03 (500 µm), and SApH06 (1000 µm).

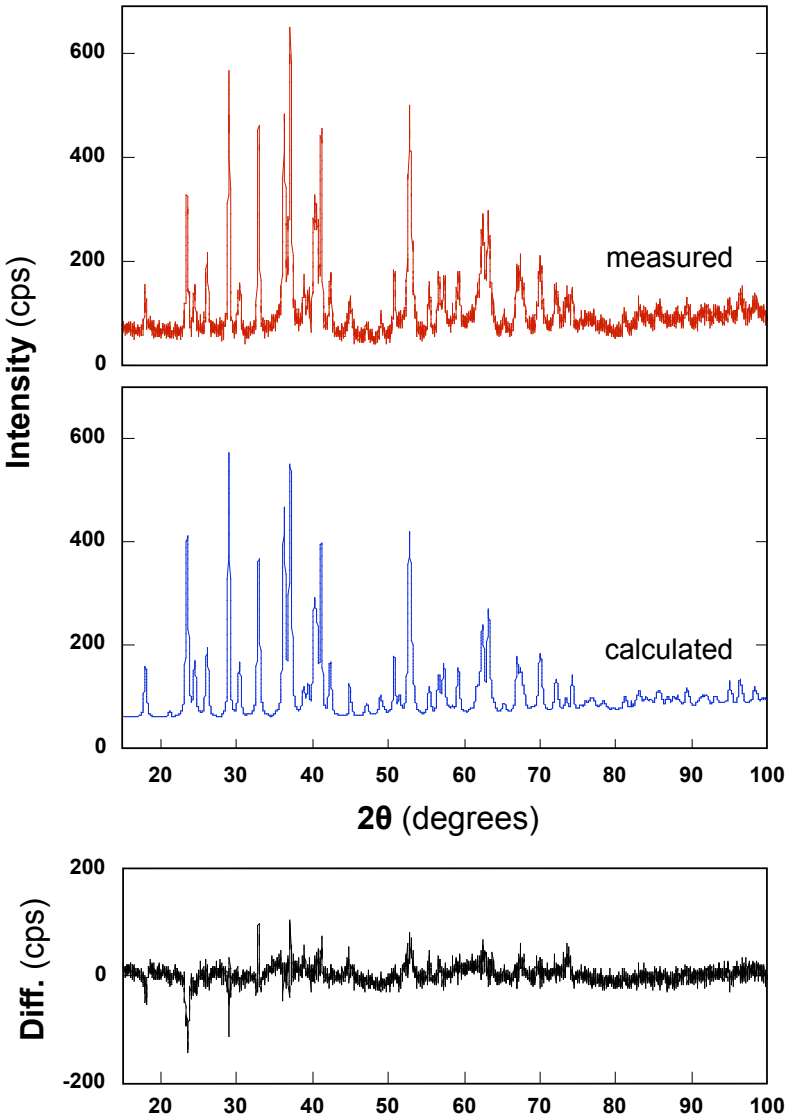

Figure V-5. Measure and calculated PXRD patterns of suspended material from experiment SApH08 showing the presence of forsterite only.

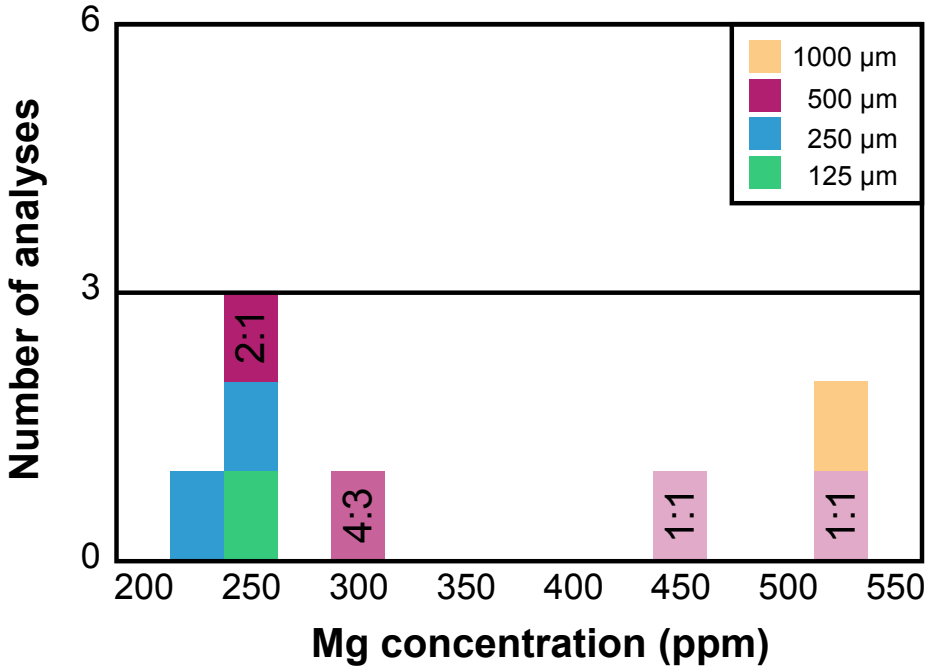

Figure V-6. Histogram showing the relationship of Mg concentration in ppm with both grain size and fluid–mineral ratio at the end of experiments. Larger grain sizes have higher Mg concentration, and smaller grain sizes have lower Mg concentration. The shaded purple boxes for 500 µm experiments show variation in fluid–mineral ratio at one grain size, with more dilute experiments having lower concentrations of Mg. All other experiments have a fluid–mineral ratio of 1:1. The histogram bin size is 25 ppm.

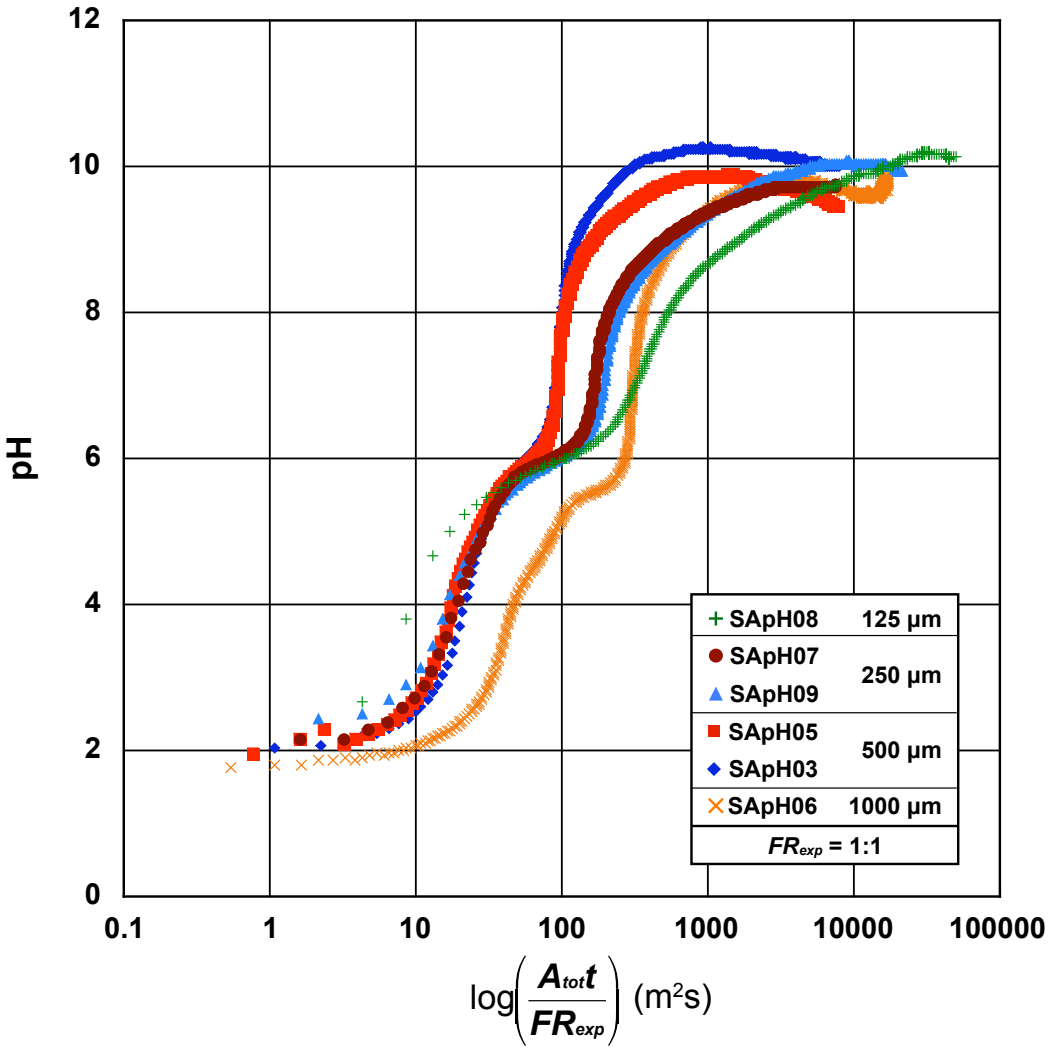

Figure V-7. Plot of pH versus surface area, fluid–mineral ratio normalized log time for constant fluid–mineral ratio (1:1) and starting solution (0.005 M H_2SO_4) with different powder sizes

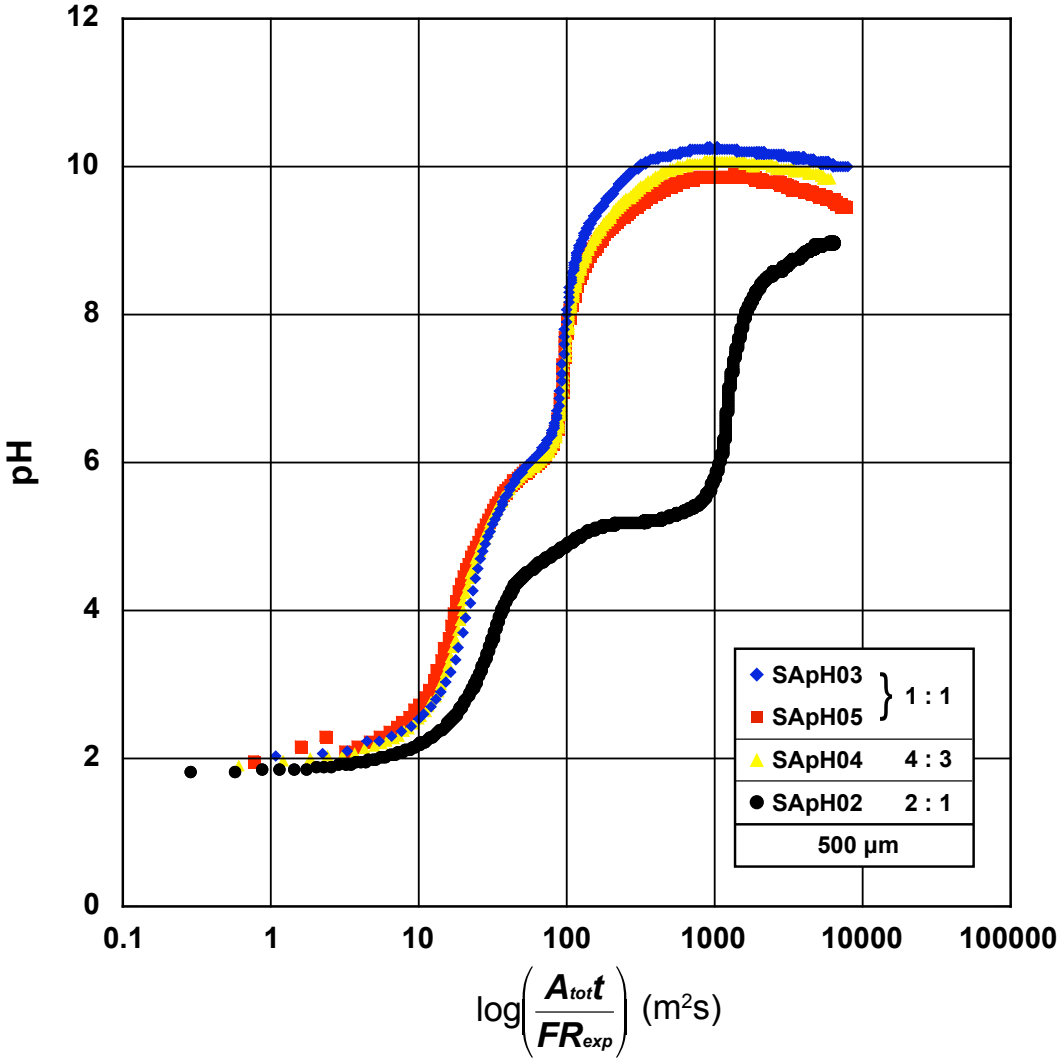

Figure V-8. Plot of pH versus surface area, fluid–mineral ratio normalized log time for constant powder size (500 µ m) and starting solution (0.005 M H_2SO_4) with different fluid–mineral ratios

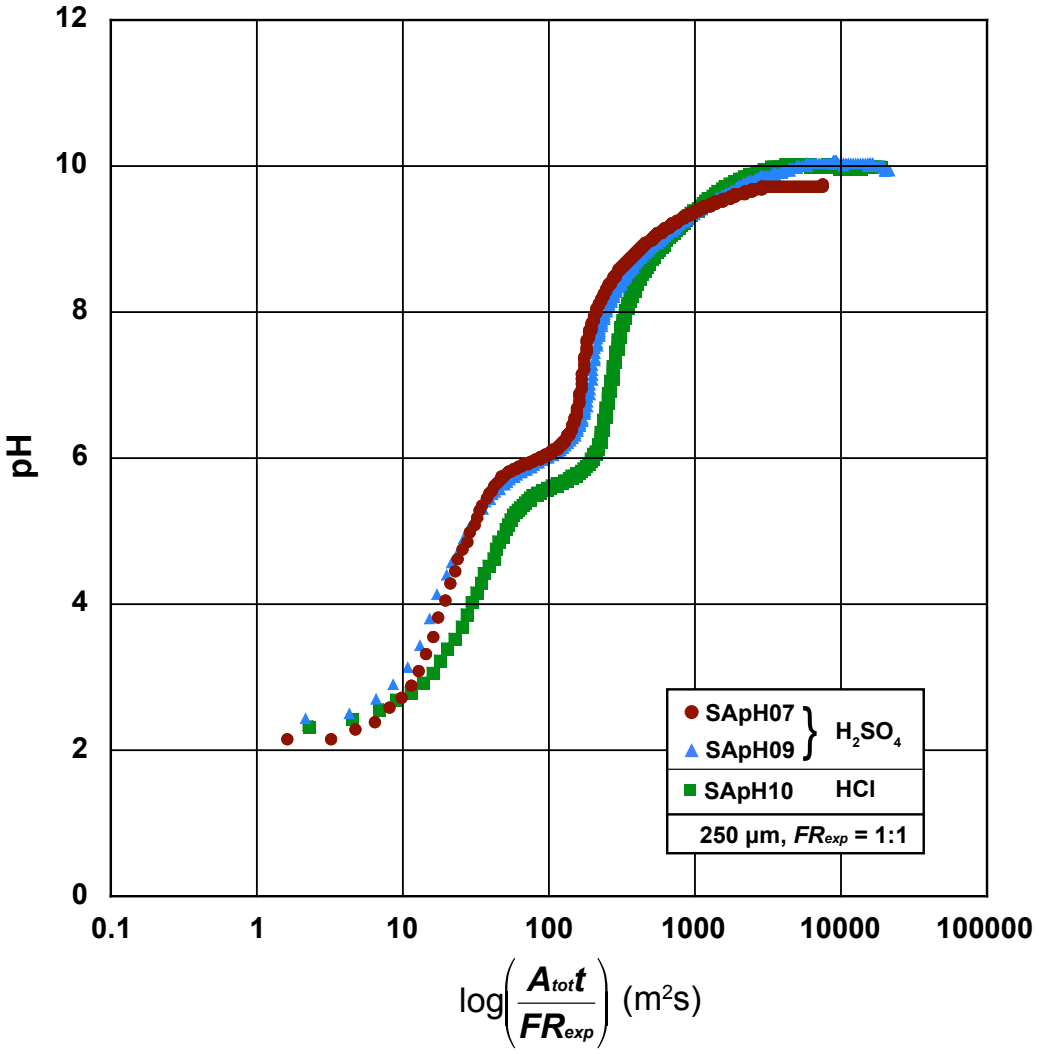

Figure V-9. Plot of pH versus surface area, fluid–mineral ratio normalized log time for constant powder size (500 µm) and fluid–mineral ratio (1:1) with different starting solutions.

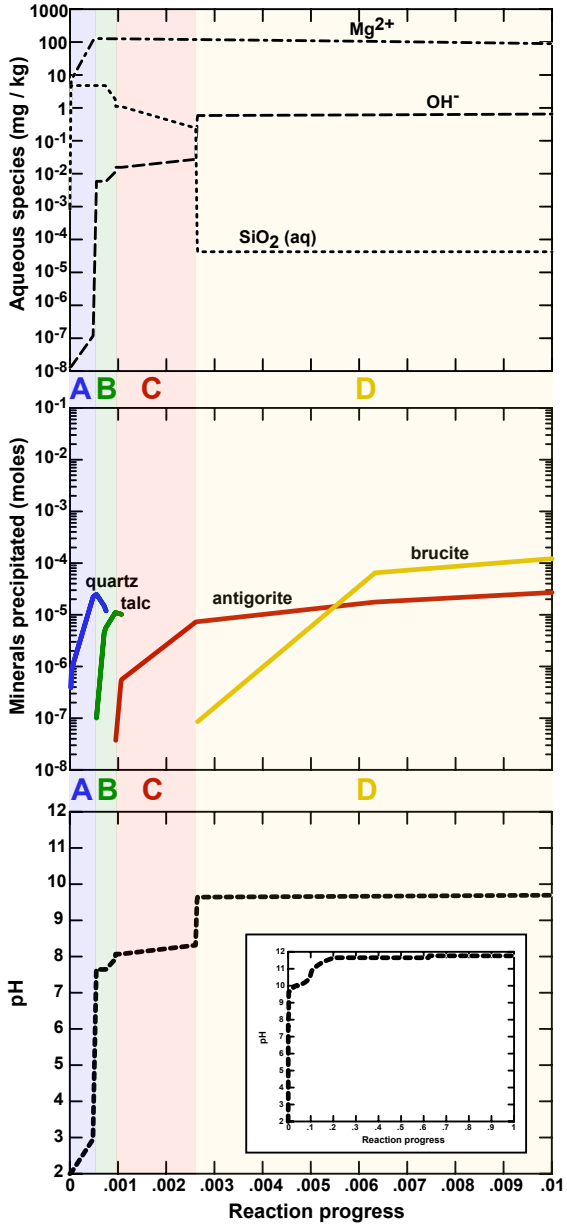

Figure V-10. GW modeled predictions of changes to the concentrations of Mg^{2+}, SiO_2 (aq), and OH^- species in solution, potential minerals precipitated and consumed, and overall pH using the starting conditions of experiment SApH03 (see Table V-1).

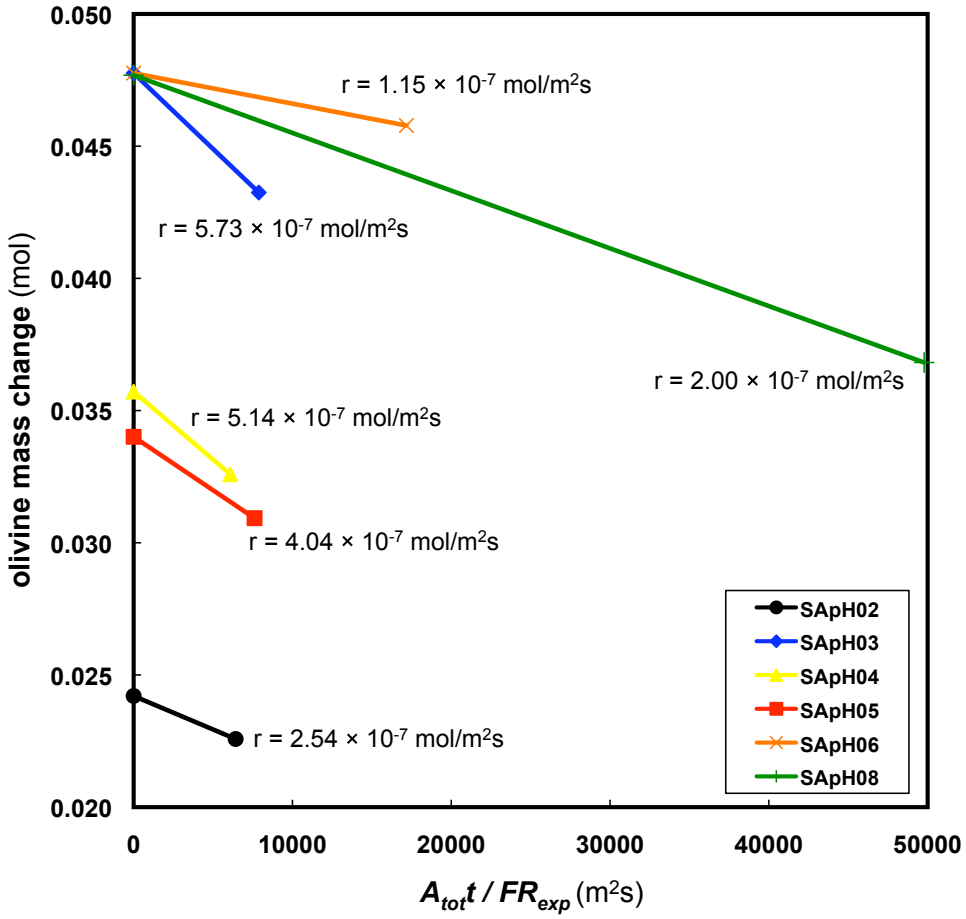

Figure V-11. Plot of olivine removed versus surface area, fluid–mineral ratio normalized time. The removal rate calculated for each experiment is displayed next to each experiment curve. Calculation of an average rate of removal yields 3.46×10^{-7} (1.81×10^{-7}) mol/m^{2}s for all experiments plotted.

Part VI.
Experimental Investigation of Aqueous Dissolution and Alteration of Olivine Crystals at Low Temperature and Pressure

This part is a reformatted version of a paper, by the same name, to be submitted to Geochemica et Cosmochimica Acta by Michael T. DeAngelis, Theodore C. Labotka, Mostafa Fayek, Harry M. Meyer III and David R. Cole.

DeAngelis, M.T., Labotka, T.C., Fayek, M., Meyer III, Harry M. and Cole, D.R. Experimental investigation of aqueous dissolution and alteration of olivine crystals at low temperature and pressure. 2011. *To be submitted*.

Abstract

Single–crystal plates of San Carlos olivine were used in experiments to observe changes to the surface of crystals resulting from reaction at low temperature and pressure with neutral and low-pH solutions. These plates of olivine were cut and polished from larger crystals and were placed in either Pyrex or gold capsules. A fluid composed of H_2O, HCl, or H_2SO_4 was added at the fluid–mineral ratio of interest, and the experimental charge was heated under pressure to a temperature of interest for experiment durations up to 90 days. The olivine plates did not appear to have changed significantly in size or shape after experiment, but nearly all plates had minor (< 1%) weight losses and samples from acidic starting solution experiments showed some color change. The solution pH in all experiments increased from its initial value of pH 2 for low-pH starting solution experiments and pH 7 for neutral starting solution experiments to values as high as pH 7–8 by the end of experiment. Profilometry of sample surfaces indicated significant changes to surface topography, with some samples having increased in surface roughness by over 2000%. X-ray photoelectron spectroscopy (XPS) and secondary ion mass spectrometry (SIMS) depth profiling indicate dissolution of Mg occurred on the surfaces of most experiments to depths between 50–100 nm. SIMS analysis also directly measured the composition of H^+ ions at the surface, and indicated

the protonation of the surface at depths up to 50 nm. The results of the experiments performed here are analogous to the very beginning of both chemical weathering of olivine in surface environments and alteration of olivine in hydrothermal circulation environments. We have shown that neutral and low pH fluids interacting with olivine have the general result of dissolving Mg^{2+} from the surface of olivine grains, protonation of vacant octahedral sites with H^{+} ions from the fluid, and surface roughening that resulted from this transfer of ions and possibly from nucleation of very small (<50 nm) alteration phases.

1. Introduction

The mineral olivine, $(Mg,Fe)_2SiO_4$, is an important constituent of rocks found in a multitude of terrestrial and Martian crustal settings. Much of the ocean crust on Earth is composed of peridotites and basalts that contain primary mantle-derived olivine, as well as serpentinites that resulted from the alteration of olivine. Basalt, ophiolites, metamorphosed carbonate rock, and a variety of other ultramafic bodies also contribute to the collection of olivine-bearing rocks found in the oceans and on the continents. On Mars, geochemical evidence collected from both satellites and various rover missions has confirmed that much of the surface is composed of olivine-bearing rocks (e.g. McSween et al., 2006).

Though olivine presently exists in these various surface or near-surface settings, it is not thermodynamically stable in the presence of water. On both the surface of the Earth and Mars, olivine is constantly subjected to environmental conditions that lead to its dissolution or alteration to more stable phases. Surface weathering experiments with olivine at low temperature (25 °C) and pressure (1 atm) show that olivine dissolves congruently, while hydrothermal experiments with olivine at moderate temperature (150-300 °C) and pressure (25–100 MPa) result in the incongruent reaction of olivine and the formation of secondary phases such as antigorite and brucite. The weathering and alteration of olivine can have a profound impact on seawater composition (Wheat and Mottl, 2000), mantle composition (Hofmann, 1988), and ecosystems that directly rely on byproducts of alteration reactions. The serpentinite-hosted Lost City hydrothermal field,

for example, relies on the interaction between seawater and upper mantle peridotite to provide the high-pH fluids that are used as the primary energy source for many different microorganisms (Kelley et al., 2001; Kelley et al., 2005).

Because of the wide range of environments affected by olivine and olivine alteration and dissolution, a large number of experimental, chemical, and kinetics studies have been undertaken to understand the nature of these processes (see Alt, 1995; Brantley, 2003; Staudigel, 2003; Seyfried et al., 2004; Chevrier and Mathe, 2007 for reviews). These studies have been effective at defining and examining specific objectives, but gaps still remain in understanding the transition from olivine dissolution to alteration. A common aspect to all the previous dissolution studies is that they primarily determined kinetic factors such as dissolution rates and activation energies, which required the pH and composition of the solution to be regulated throughout the experiment. For alteration studies, experiments were generally performed at the higher temperature and pressure conditions that would ensure the formation of secondary alteration phases.

Instead, we performed closed system batch experiments starting with single crystal olivine and either water or low pH solutions of H_2SO_4 or HCl where both the volume of the solution and mineral were fixed. We allowed the pH and solution composition to evolve during experiments with the expectation that continued dissolution of the mineral surface would eventually result in saturation of the solution with Mg^{2+} and Si^{4+} and lead to the formation of secondary phases. The use of a number of surface-specific analytical techniques such as profilometry, X-ray photoelectron spectroscopy (XPS), secondary ion mass spectrometry (SIMS), and scanning electron microscopy

(SEM) has allowed us to examine the physical and chemical changes to the surfaces of our experimental olivine single crystals over a range of scales.

2. Previous Work

2.1. Dissolution of olivine

Much previous work has been done to determine the rates of forsteritic olivine dissolution at low temperature (25–150 °C) under a variety of pH conditions (Luce et al., 1972; Grandstaff, 1978; Siever and Woodford, 1979; Siegel and Pfannkuch, 1984; Berner et al., 1985; Blum and Lasaga, 1988; Brady and Walther, 1989; Vanherk et al., 1989; Wogelius and Walther, 1991; Brady and Walther, 1992; Casey and Westrich, 1992; Wogelius and Walther, 1992; Westrich et al., 1993; Jonckbloedt, 1998; Awad et al., 2000; Chen and Brantley, 2000; Pokrovsky and Schott, 2000a; Pokrovsky and Schott, 2000b; Rosso and Rimstidt, 2000; Oelkers, 2001; Zhao et al., 2001; Hanchen et al., 2006; Liu et al., 2006; Olsen and Rimstidt, 2007; Olsen et al., 2008; Olsen and Rimstidt, 2008; Rimstidt et al., in press). These experiments have shown an increasing dissolution rate with decreasing pH under acidic conditions. The data for neutral to basic conditions are more ambiguous. Some data show an increase in dissolution rate with increasing pH away from neutral (Blum and Lasaga, 1988), while others find no pH dependence on dissolution under basic conditions (Pokrovsky and Schott, 2000a; Pokrovsky and Schott, 2000b; Hanchen et al., 2006). The difference in the dissolution response of forsteritic olivine at ranging pH has been suggested to reflect a change in reaction mechanism at the surface. For acidic conditions, the term ‘proton-promoted dissolution’ has been used to

describe the process by which H^+ is adsorbed onto the olivine surface while Mg^{2+} ions are extracted from the surface. This extraction of cations results in a thin (10-30 Å), but detectable, Mg-depleted layer (Seyama et al., 1996). Under basic conditions, however, Si^{4+} becomes depleted instead of Mg^{2+}. This occurs as SiO_2 is removed from the olivine and surface groups of $MgOH_2$ are formed (Hanchen et al., 2006). It is generally believed that the presence of a leach layer is not rate limiting (see Brantley, 2003 for discussion). Prolonged dissolution is stochiometric, and no secondary minerals have been observed in any of these open system experiments in which the solution is constantly cycled to buffer pH. Experiments have also been performed at elevated temperature up to 150 °C, with the intent of examining the effects of temperature on the kinetics of dissolution. The rate of olivine dissolution has been found to be temperature dependent, with faster rates of dissolution occurring with higher temperature. Activation energies have also been determined, and the range varies between 25 and 125 kJ/mol (Hanchen et al., 2006).

2.2. Alteration of olivine

Hydrothermal alteration adjacent to mid ocean ridge spreading centers is one of the most common methods for altering olivine in the crust of the Earth (Alt, 1995; Staudigel, 2003; Seyfried et al., 2004). This interaction of olivine with continuously convecting fluids adjacent to mid-ocean ridge spreading centers results in large zones of alteration. Alt (1995) divided the convection of circulating hydrothermal fluids in these environments into two main types: active and passive convection.

Active convection is the infiltration and transport of fluid through ocean crust near the ridge axis where the temperature is in excess of 250 °C. The depth of penetration of fluid in active convection zones depends on the type (speed of spreading) of the

spreading center, with deeper penetration within the slower spreading Mid Atlantic Ridge type spreading center than at the faster East Pacific Rise type spreading where fluid penetrate to a limited depth because of the presence of a larger melt lens (Alt, 1995). Most of the fluid entering the system exits at a lower temperature within the upper volcanic (more permeable) zone, with only a small amount of fluid circulating through sheeted dikes before exiting at higher temperature (Rosenberg et al., 1993). Passive convection of fluid occurs off axis, where the temperature does not exceed 200 °C and the rate of circulation is much slower. The depth of penetration of fluid can be one to several kilometers, with most of fluid circulation restricted to the high permeability zones in the uppermost basement (Fisher et al., 1994). In both the active and passive convection zones, olivine becomes hydrated and forms a significant amount of serpentine. Circulation of hydrothermal fluid can continue in ocean crust as the crust move away from the ridge for up to 65 million years (Stein and Stein, 1994). This incorporation of seawater significantly alters the volume and density of ocean crust, and these changes may be a contributing factor to mechanisms of ocean plate tectonic movement.

Previous experiments have been performed to specifically examine the alteration of basalts, peridotites, and olivine under conditions of temperature, pressure, and solution compositions consistent with mid ocean ridge crustal environments (Bowen and Tuttle, 1949; Johannes, 1968; Martin and Fyfe, 1970; Chernosky, 1975; Moody, 1976; Dungan, 1977; Bischoff and Seyfried, 1978; Seyfried and Bischoff, 1979; Seyfried and Dibble, 1980; Seyfried and Bischoff, 1981; Seyfried and Mottl, 1982; Wegner and Ernst, 1983; Janecky and Seyfried, 1986; O'Hanley and Wicks, 1995; Snow and Dick, 1995; Berndt et al., 1996; O'Hanley and Dyar, 1998; McCollom and Seewald, 2001; Normand et al.,

2002; Allen and Seyfried, 2003; Seyfried et al., 2007). These experiments have confirmed the alteration of olivine to serpentine and brucite by the known equilibrium:

$$2\ Mg_2SiO_4 + 3\ H_2O = Mg_3Si_2O_5(OH)_4 + Mg(OH)_2$$
(forsterite + water = serpentine + brucite)

There is considerable debate regarding the predominant nucleating and crystallizing serpentine phase at temperatures between 150 and 300 °C and pressures between 30 and 100 MPa (Evans, 2004). Antigorite is the thermodynamically stable phase at these temperatures, but metastable lizardite and chrysotile are often the observed products of olivine hydration in both natural and experimental settings. Various explanations for the occurrence of these metastable phases have been proposed (Chernosky, 1975; Moody, 1976; Dungan, 1977; O'Hanley and Wicks, 1995; Grauby et al., 1998; O'Hanley and Dyar, 1998; Normand et al., 2002; Evans, 2004). Dungan (1977) suggested that lizardite and chrysotile are preferred over antigorite because of the lower activation energies required for nucleation of these phases. That study asserted that the lower activation energies reflect differences in the crystal structures of the various serpentine phases and that lizardite and chrysotile are more likely to have topotactic growth with olivine. The crystal structure of antigorite is significantly more complex, and this results in sluggish nucleation. Hydrothermal experiments performed by Grauby et al. (1998) at 300 °C and 70 MPa suggested that activation energy and crystal structure are not the only controls on serpentine-phase nucleation, but that supersaturation of dissolving forsterite within the solution can also affect the nucleating phase. Their experiments suggested an order of serpentine formation from chrysotile → polygonal serpentine → lizardite with increasing time of reaction. Many researchers (Chernosky,

1975; Moody, 1976; O'Hanley and Wicks, 1995; O'Hanley and Dyar, 1998; Normand et al., 2002), however, suggested that chrysotile is the higher temperature metastable phase of serpentine based on both experimental and natural studies. O'Hanley and Wicks (1995) suggested that the recrystallization of lizardite and replacement by chrysotile occurs around 250 ± 25 °C at pressures less than 100 MPa.

3. Methods

3.1. Experimental methods

The starting material for all experiments was natural single crystals of San Carlos olivine, $Mg_{1.8}Fe_{0.2}SiO_4$, from San Carlos, Arizona. Thin (~0.5 mm), parallel, doubly polished olivine plates were created by mounting olivine single crystals (~5 mm diameter) in epoxy, making parallel slices of the mounts using a thin blade saw, dissolving the epoxy with methylene chloride, and hand polishing both sides of each olivine plate using 1 μm diamond paste. The olivine crystals were not precisely oriented prior to slicing. However, they were positioned with the long dimension (approximately the b axis) parallel to the slice direction.

The experiments and conditions are given in Table VI-1. Both gold capsules and Pyrex tubes were used to contain experimental charges. Pyrex tubes were generally used for lower temperature and pressure experiments and gold tubes used for higher temperature and pressure experiments, though there was some intentional overlap of experimental conditions using both gold capsules and Pyrex tubes (Table 1).

For gold capsule experiments, a single olivine plate was placed in a 5 mm diameter gold capsule, and a solution of interest was added. Compositions of solutions used in these experiments included: 0.01 M HCl (starting pH 2), 0.005 M H_2SO_4 (starting pH 2), or deionized H_2O (starting pH 7). The fluid–mineral ratio was 5:1 (by mass) for all experiments in gold capsules. The solution was cryogenically frozen and the tube evacuated and sealed with a cold weld crimp. The gold capsule was then placed in a cold-seal hydrothermal vessel, and the pressure and temperature were raised to the experimental conditions of interest (150 or 300 °C, 5 or 20 MPa). These applied external pressures were used to help offset any increases in the internal capsule pressures. The group 11 experiments, however, did not have any added external pressure and were performed by placing the gold capsules in an oven set at 150 °C. Experiment durations ranged from 30 to 90 days.

For Pyrex tube experiments, two plates per experiment were placed in a 3/8" x ~ 8" Pyrex tube, and the solution of interest was added in either a 5:1 or 15:1 fluid–mineral ratio, measured by mass. Compositions of solutions used in these experiments included: 0.01 M HCl (starting pH 2), 0.005 M H_2SO_4 (starting pH 2), or deionized H_2O (starting pH 7). The solution was cryogenically frozen and the tube evacuated and sealed using an acetylene torch. The experiments were evacuated to ensure that there would be no exchange with air and so that the internal pressure upon heating would be approximately known by following the liquid–vapor curve for water. Experiments using Pyrex tubes were performed at 25 and 150 °C using a water bath to regulate the temperature for the 25 °C experiments and an oven to regulate the temperature for the 150 °C experiments.

The liquid–vapor curve pressure for pure water is 0.00317 MPa at 25 °C and .47616 MPa at 150 °C (Lemmon et al., 2011). Experiment durations ranged from 1 day to 9 weeks.

3.2. Analytical techniques

A KLA-Tencor P-16+ Profilometer was used to examine the surface topography of the olivine plates both before and after experiment. Both two dimensional (2D) profile scans and three dimensional (3D) surface scans were performed. The 2D profile scans were performed along a unidirectional line 500 μm long at a rate of 2 μm/s; each line having 24,810 points spaced ~20 nm apart. Each 3D surface scan covered a 100 × 100 μm area and were collected by rastering 100 line scans spaced 1 μm apart; each line having 100 points spaced ~1 μm apart. The location of scans was not the same before and after experiment.

The surfaces were also examined with use of a Hitachi S-3400 Variable Pressure Scanning Electron Microscope (SEM). The SEM had an accelerating voltage potential of 20 kV, a working distance of 12 mm, and images were collected at a range of magnifications. A variable pressure SEM was used for this study because samples did not require carbon coating prior to analysis, helping to limit the contamination on the olivine surface and allowing for subsequent analyses with other analytical techniques.

X-ray photoelectron spectroscopy (XPS) is a surface chemical analysis technique that irradiates a sample with X-rays and detects released photoelectrons from the top few mono-atomic layers. We used the Thermo Scientific K-alpha X-ray Photoelectron Spectrometer at Oak Ridge National Laboratory to monitor element concentration changes with depth. The surfaces of samples were successively sputtered with an Ar^+ beam at a rate of 12 nm/min. Analysis depth was determined by calibrating the sputter

parameters using a standard 100 nm SiO_2 film, and was 400 nm or less for all analyses. Elements and electron shells to be analyzed by depth profile were determined by collecting survey spectra of each sample and included some or all of the following: Al 2p, C 1s, Fe $2p_{3/2}$, Mg 1s, Mg 2p, Na 1s, O 1s, and Si 2p.

Depth profiles of $^{1}H^{+}$, $^{24}Mg^{+}$, $^{30}Si^{+}$, and $^{54}Fe^{+}$ were obtained with the use of the CAMECA ims 7f Geo secondary ion mass spectrometer (SIMS) located in the Manitoba Regional Materials and Surface Characterization Facility at the University of Manitoba. Samples were prepared by applying a gold coat (~30 seconds of sputtering time) to a grain mount. Because analysis using the SIMS requires that the sample be gold coated prior to analysis, this was generally the last analytical technique to be used on sample surfaces. Samples were sputtered with the use of an O^{-} primary ion beam accelerated at 22.5 keV, with analysis of positively charged secondary ions. Primary beam currents were ~ 5 nA, had a diameter of 10-20 μm, and the beam was rastered over a 150 × 150 μm^2 area. Each depth profile consisted of 263 cycles of data. The depth of each crater was measured with the use of a profilometer after analysis, and were determined to generally be 500 nm or less and sputtered at a rate of approximately 0.1–0.2 nm/s.

4. Results and Discussion

4.1. Macroscale observations

The most common observation from all experiments is that there was no noticeable change in the size and shape of the olivine plates. The immediate implication of this is that it seems there were no experiments run under conditions suitable to cause the olivine to significantly alter to secondary phases. Most of the generally expected new

phases that form from alteration of olivine (e.g. talc, serpentine, various phyllosilicates) incorporate water in their structures, resulting in an increase in volume (+ΔV) of those products of reaction. The common textural result of this +ΔV for olivine single crystals should be the development of an alteration "armor" encasing the original crystal. Labotka et al. (2006), for example, performed hydration experiments with dunite core samples and described the presence of serpentine along the outside surfaces of core, with only limited amounts of reaction along grain boundaries and fractures through the cores. While there was some minor Fe oxidation leading to a green to orange color change in some of the acidic starting solution experiments, the production of new mineral phases armoring the olivine plates was not observed.

Nearly all olivine crystals showed some amount of weight loss by the end of the experiments (see Table VI-1). The greatest amount of weight loss occurred in the HCl experiments, with percent weight loss for HCl experiments ranging from 0.12% for the H03 (25 °C, 16 day, 5:1 fluid–mineral ratio) experiment up to 0.50% (avg) for the H06 (150 °C, 29 day, 15:1 fluid–mineral ratio experiment. The H_2SO_4 experiments had smaller amounts of weight change than the HCl experiments, but the H_2O experiments had significantly less change in weight, compared with the other two types of experiments. This higher weight loss for the experiments using acidic starting solutions is consistent with the change in olivine dissolution rates with pH; faster dissolution rates (10^{-7} to 10^{-8} mol/m^{2}s) under low pH conditions and slower dissolution rates (10^{-9} to 10^{-10} mol/m^{2}s) under neutral pH conditions (Brantley, 2008; Olsen et al., 2008; Rimstidt et al., in press; Part V of this dissertation). The starting pH for the HCl and H_2SO_4 experiments was lower (pH 2) than the starting pH for the H_2O experiments (pH 7), and the

subsequent amount of pH change was larger for the experiments that started with low pH (Table VI-1). The larger weight changes of the low pH experiments likely resulted from an initial surge of dissolution at low pH followed by slowing dissolution and decreasing weight loss as the pH became more neutral and the dissolution rate became slower (Part V of this dissertation). Most of this dissolution surge, weight loss, and fast pH change probably occurred within the first few hours of the experiment. Experiment H04, for example, had a pH change from 2 to 6.17 and an average percent weight change of 0.18% after only 1 day at 150 °C.

4.2. Profilometry

The topography of olivine plate surfaces from the gold capsule experiments was measured by profilometry before and after experiment. The surfaces of all these experiments had some amount of topography change, with low pH starting solution experiments showing more change than those that used H_2O (Table VI-2). Both 2D profile scans and 3D surface scans were performed to better quantify these changes to surface topography.

4.2.1. 2D profile scans

The primary objective in performing 2D profile scans was to collect detailed topographic information that could be processed and used to determine surface roughness parameters. A 500 μm long traverse was performed at a randomly selected location on each olivine plate before and after experiment. Each of these traverses measured over 20,000 points per line, with each measured spot spaced approximately 20 nm apart.

Despite efforts to keep the two sides of each olivine plate parallel with one another during cutting and polishing, all of the olivine plates used in these experiments

have slightly sloped surfaces at the nanometer scale. The first step in processing these data, therefore, is to level each profile so that peaks and valleys can be measured relative to a graphical centerline. The most common leveling method, and the one used here, is the least squares method. This method works by leveling a profile by a line of the least squares that best fits the slope of the sample. This leveling operation was performed on each of the collected 2D profiles, and an example of leveled profiles using this method can be seen for the S08 experiment (Figures VI-1 and VI-2).

Qualitative comparison between the profiles in Figures VI-1 and VI-2 show a noticeable increase in surface roughness. Increases in surface roughness can be quantified by filtering the wavelengths into two parts: long wavelengths (waviness) and short wavelengths (roughness). The filter selected for this data manipulation was a robust Gaussian filter with a cut-off value of 0.1 mm (see ISO standard TS 16610-22 for more details). Generally, wavelengths larger than the cut-off value are distributed to the waviness component and wavelengths smaller than the cut-off value are distributed to the roughness component. However, the cut-off value of 0.1 mm selected here was significantly large enough to ensure all values were distributed to the roughness component. For this reason, the roughness profiles are nearly identical to leveled profiles.

Several roughness parameters (*Ra*, *Rq*, *Rp*, *Rv*, *Rt*) have been determined from the roughness profiles of each experiment (Table VI-2). Three of these roughness parameters found in Table VI-2 are the maximum profile peak height (*Rp*), the maximum profile valley depth (*Rv*), and the maximum relief of the profile (*Rt*) over the sampling length, which for these measurements was the entire 500 μm length of the profiles. The

roughness parameter *Ra* is the arithmetic mean deviation from the graphical centerline of the roughness profile, and is defined by the following equation:

$$Ra = \frac{1}{L}\int_0^L |y| dx \tag{1}$$

where L is the sampling length (500 μm) and y is the ordinate height of the roughness profile relative to the mean. The roughness parameter R_q is the root mean squared average of the roughness profile, and is defined by the following equation:

$$Rq = \sqrt{\frac{1}{L}\int_0^L y^2 dx} \tag{2}$$

where again L is the sampling length (500 μm) and y is the ordinate height of the roughness profile relative to the mean.

The *Ra* value provides a general scale of roughness that is symmetrical about the centerline and has a Gaussian distribution of peak and valley heights. However, it does not always accurately describe the true nature of the roughness. For example, the surface of one sample having similar peak heights and valley depths could have comparable *Ra* values to the surface of a second sample having no peaks but valley depths similar to the first sample. Instead, the *Rq* parameter calculates roughness by squaring the y value, giving emphasis to large values of y over small values. The *Rq* parameter values can then be compared with *Ra* parameter values to determine if there is regular distribution of peaks and valleys or if the roughness of the surface is dominated by either peaks or valleys. Large differences between *Ra* and *Rq* values ($Rq > 2Ra$) would indicate that the surface has a more even distribution of peaks and valleys whereas smaller differences

between *Rq* and *Ra* values ($Rq < 2Ra$) would indicate that surface roughness is dominated by either peaks or valleys but not both.

Comparison of *Ra* and *Rq* values from the olivine plates before experiment indicate that these surfaces did not have a regular distribution of peaks and valleys (i.e. the *Rq* values are generally less than $2Ra$). It is likely that the surfaces of these experiments had more valleys than peaks before experiment due to the development of small scratches during the polishing process. Comparison of *Ra* and *Rq* values from the olivine plates after experiment do not indicate any consistency between experimental conditions and prevalence of peaks or valleys. However, these parameters do indicate significant increases in surface roughness resulting from experiments. The change in the *Ra* parameter resulting from experiment ranges from a minimum increase of 54% in experiment W11 up to a maximum increase of 2658% in experiment H09. There may also be some correlation between increasing surface roughness and duration of the experiment. Comparison between experimental group 08 and 09, which had the same experimental conditions but different durations (28 days for group 08, 90 days for group 09), show much larger % *Ra* increases in the longer duration experiments (see Table 2).

4.2.2. 3D surface scans

A limited number of 3D surface scans were also performed to observe changes to surface topography resulting from experiments. The resolution of these scans was not as high as the 2D profile scans, but they have the advantage of generating three dimensional images better suited to qualitative comparison. An example of this type of 3D surface scan performed for experiment S09 (see Table 1) can be found in Figure VI-3. This figure compares randomly located 100×100 μ m 3D surface scans both before and after

experiment. Higher resolution 25×25 μm 3D surface scans collected from within the larger squares are also in Figure VI-3. Most of the area in the scan before experiment has a surface that is relatively smooth with an average vertical relief of ~25 nm (*Rt* = 22 nm from 2D surface roughness measurements before experiment). The large peak located near the center of the before experiment image in Figure VI-3 is because of the presence of a grain of dust on the surface and does not reflect the actual surface roughness of this plate. The after experiment 3D surface scan image, by comparison, shows a much rougher surface, with an approximate average vertical relief in this image between 500 and 600 nm (*Rt* = 283 nm from 2D surface roughness measurements after experiment). The comparison of 3D scans in Figure VI-3 before and after experiment show a general increase in the height of peaks and depth of valleys after experiment. Interestingly, the after experiment image also shows the development of a few significantly larger peaks, which may indicate the location of very small (< 50 nm) alteration phases.

4.3. SEM imaging

SEM imaging was used to examine the olivine plate surfaces for any changes in texture or topography, and to locate and chemically examine any potential alteration products. Unfortunately, the application of this technique using a variable pressure SEM and uncoated samples was not sensitive enough to detect any significant changes to the olivine surface (Figure VI-4). There was no new observable mineralization with use of this SEM, and the nanometer scale textural and topographic changes that did occur were better observed using other techniques. Performing SEM image collection with coated samples and a higher resolution SEM was considered, but analyses using XPS and SIMS

suggested that collecting these additional images would not have changed our initial SEM interpretation of a lack of significant amounts of alteration phases.

4.4. XPS depth profiling

XPS analysis was used to examine the change in elemental composition with depth in these experiments. Though this technique is only able to obtain compositional information from the first 1 to 10 nm of material being analyzed, samples was successively sputtered with an Ar^+ beam to remove material and then reexamined to gather compositional information with increasing depth.

Prior to beginning any XPS depth profile analysis, a wide-scan survey spectrum of photo-emitted electrons is collected to identify peaks corresponding to the presence of different elements (Figure VI-5). Figure VI-5 shows the survey spectrum for unreacted olivine starting material, identifying peaks for O 1s, Mg 1s, Fe $2p_{3/2}$, C 1s, Si 2p, and possibly Na 1s. Some survey spectra from other experiments has also identified Al 2p, Mg 2p and Ni 1s, but, with the exception of Mg 2p, these are all very minor compositional components. XPS depth profile analysis began after the peaks were identified and continued to the depth of interest (Figure VI-6). Figure VI-6 shows a collected depth profile for the unreacted olivine starting material showing composition in percentage of atoms versus depth. There is a minor skew in the Mg 1s, Si 2p, and O 1s data at the beginning of the profile because of the presence of a small amount of carbon. Because these samples have been exposed to the atmosphere or, perhaps, SEM analysis prior to XPS analysis, some small amount of carbon is observed in the first few nanometers of nearly all the samples. The background concentrations of Fe and any possible Na are extremely low in these olivine sample, so they are not given significant

further consideration. Counts for O 1s and Si 2p are fairly constant in all experimental samples, so the focus is primarily on the changes to Mg 1s with depth.

XPS analyses of experimental samples have confirmed the presence of a Mg depleted layer at the surface of many experiments (Figures VI-7–VI-10). Experimental results seem to indicate a correlation of Mg depletion depth with experimental conditions, with the most extreme conditions having the greatest depth of Mg depletion. This type of dissolution-derived Mg depletion has been observed in other olivine studies and is often coupled with the formation of an amorphous Si-rich rind (Brantley, 2008). Though the formation of a definitive Si-rich phase was not observed in these experiments, the concentration of Si does remain nearly constant through the Mg depletion zone, indicating that the concentration of remnant Si becomes enhanced relative to the amount of remaining Mg. Interestingly, the experiments that used Pyrex also indicated the presence of minor amounts of aluminum on the sample surface. This aluminum may be the result of acid leaching of the Pyrex tube, however, dissolution experiments performed by Chen and Brantley (2000) found that aluminum does not affect dissolution rate. Regardless, gold capsule experiments were also performed to help reduce chances of contamination, and these also showed Mg depletions similar to the Pyrex experiments.

Because the concentration of Si remains fairly constant with depth in XPS analyses of olivine plates, it can be used to normalize the Mg data by dividing the Mg1s counts by the Si2p counts. This has been done for all of the XPS depth profile data presented in Figures 7–10. These figures contain comparisons of data based on variation in experimental conditions and either use data from H_2O or H_2SO_4 starting solution experiments. Because of limited availability for the XPS instrument, only one set of

acidic starting solution experiments were analyzed (i.e. no HCl starting solution experiments).

Figure VI-7 shows a time-difference comparison of the 1 day and 14 day experiments performed in Pyrex with both H_2O (W04, W01) and H_2SO_4 (S04, S01) starting solutions at 150 °C, 0.1 MPa, and 5:1 fluid–mineral ratio. These experiments show a definite increase in the amount of Mg removed from the surface after 14 days compared with the amount removed after 1 day. The type of starting solution also affects the amount of dissolution, and, after 14 days, there is noticeably more Mg removal overall in the S01 experiment than in the W01 experiment.

A comparison of differences in fluid–mineral ratio for H_2O starting solution experiments is shown in Figure VI-8. Though the amount of Mg removal is generally less for H_2O experiments when compared with acidic starting solution experiments, this figure shows that the fluid–mineral ratio also affects dissolution rate. Experiment W02 (5:1 fluid–mineral ratio) shows significantly less dissolution than the W06 (15:1 fluid–mineral ratio) experiment. The higher fluid–mineral ratio in the W06 experiment likely acts as a buffer against pH change. The result of this buffering is that more Mg dissolution can occur because olivine dissolution rate is known to be faster at lower values of pH (Brantley, 2008; Rimstidt et al., in press). The final pH of both experimental solutions was higher than initial values (see Table VI-1), but there was likely a delay in pH change for the 15:1 fluid–mineral ratio experiment. This type of pH change delay was also observed in olivine powder experiments as a result of differences in fluid–mineral ratio (Part V of this dissertation).

The response of these experiments to use of two different types of capsules and different external pressure is shown in Figure VI-9. In both the W08 (H_2O) and S08 (H_2SO_4) experiments, the higher external pressure, gold capsule experiments showed decreased dissolution compared with the lower external pressure, Pyrex capsule experiments (W02, S02). In the gold capsule experiments where there was no applied external pressure (W11, S11), the amount dissolution was comparable to the Pyrex experiments. One explanation for these differences may be that the applied external pressure limited fluid accessibility to the olivine plates by collapsing the gold around the olivine. Additionally, the increased pressure on the capsules also likely created a condition at which olivine became more thermodynamically stable. At 150 °C, the external pressure of 5 MPa used in the group 08 experiments may place the olivine sample within the stability field for forsterite and H_2O.

None of the Pyrex capsule experiments run at 25 °C were analyzed using XPS, so comparison on the basis of temperature is limited to 08 and 10 group experiments only (Figure VI-10). These two sets of experiments were run for the same duration at the 5:1 fluid–mineral ratio, but did differ in the temperature and applied external pressure (150 °C at 5 MPa and 300 °C at 20 MPa). The results from these experiments are remarkably similar and show very limited dissolution. This again may be the result of large external pressures limiting dissolution of the olivine plates in these experiments.

4.5. SIMS depth profiling

A limitation of the XPS technique is that it can not be used to examine changes to the concentration of hydrogen in these samples. Surface analysis with Fourier transform infrared spectroscopy (FTIR) was initially attempted to look for O-H absorption and

other possible hydrogen features, but the olivine plates used in these experiments were too thick for transmission FTIR and interferences from Si made the use of attenuated total reflectance spectroscopy (ATR-FTIR) problematic. Instead, SIMS depth profiling was used to directly measure changes in concentration of $^{1}H^{+}$, $^{24}Mg^{+}$, $^{30}Si^{+}$, and $^{54}Fe^{+}$ in both starting material and experimental samples.

A example of SIMS depth profiling is shown for the starting material and the 09 group experiments (Figure VI-11). These experiments were all performed at 150 °C, 5 MPa, in gold capsules, and with a 5:1 fluid–mineral ratio, but the starting solutions and initial pH varied (Table VI-1). This set of experiments was selected for discussion because they were the longest duration of all of the experiments performed (90 days), so presumably these experiments should show the most changes to the olivine surface. The shape of the raw depth profiles in Figure VI-11 have some commonalities and some differences. The feature common to these four profiles, and, in fact, all collected SIMS depth profiles, is the large peak in the curves of all measured ions that begins within the first few nanometers. Though the precise reason for these peaks is unknown, we surmise that they are either an artifact of some instrumentation effect (e.g. knock–on of ions) or the result from some sample preparation process (e.g. olivine plate cutting and polishing) that affected all samples equally. The shape and depth of these peaks, however, vary significantly, with the starting material and W09 (H_2O) experiment having narrower peaks than the H09 (HCl) and S09 (H_2SO_4) experiments, indicating that the acidic solutions had more of an influence on the surfaces than did water. The broad and skewed shape of the H09 and S09 peaks, particularly in the $^{24}Mg^{+}$ curves, may reflect increased

dissolution in those experiments, which would correlate with the Mg depletion observed in XPS analysis of these samples.

Another notable difference among the depth profiles in Figure VI-11 was the measurements of hydrogen ($^{1}H^{+}$) with depth. The counts of $^{1}H^{+}$ are higher than both $^{30}Si^{+}$ or $^{54}Fe^{+}$ over the depth range where the sharp peaks in the curves are observed, but quickly drop to lower values past these peaks. This may indicate that these peaks represent a depth range for dissolution and exchange on the surface, with higher $^{1}H^{+}$ concentration resulting from protonation of vacated octahedral sites. This increase in $^{1}H^{+}$ on the surface would also be consistent with the measured increase in pH observed in all experiments.

To further examine the relationship between removal of $^{24}Mg^{+}$ ions and the addition of $^{1}H^{+}$ ions, these two cations were normalized to $^{30}Si^{+}$in both the experimental samples and in unreacted olivine. The rationale for using $^{30}Si^{+}$ for normalization is that the concentration of Si is not likely to vary within the first 100 nm, since Mg is known to be preferentially dissolved instead of Si at low pH (Pokrovsky and Schott, 2000a; Rimstidt et al., in press; Part V of this dissertation). The Si-normalized experimental sample values were then divided by the Si-normalized unreacted samples to observe variation in cation concentration resulting from the experiments only (Figure VI-12). The values in Figure VI-12 show that the concentration of $^{1}H^{+}$ is lower than the concentration of $^{24}Mg^{+}$ at all depths for the starting material and the W09 experiment, but is higher than the concentration of $^{24}Mg^{+}$ for the beginning portions of the H09 and S09 experiments. Additionally, the concentration of $^{24}Mg^{+}$ in the H09 and S09 experiments in the first 10 nm is significantly lower than the starting material values of $^{24}Mg^{+}$. These results indicate

that the surfaces of acidic starting solution experiments were affected more by dissolution than the surfaces of water experiments, and that removal of Mg was indeed coupled with protonation of the surface.

4.6. Summary

While many olivine dissolution–alteration studies are focused on changes to the fluid in the experiment (i.e. pH change, dissolved and precipitated species, etc.), the goal for this study was to examine changes to the solid surface of the olivine. Surface analysis of the olivine plates used in this study showed that the experimental conditions were sufficient to dissolve and protonate olivine surfaces, and that these types of changes were detectable at the nanometer scale. Comparison of XPS and SIMS analyses show the amount of dissolution of Mg was highly dependant on the temperature, external pressure, fluid–mineral ratio, and duration of experiments, and that the results from the two techniques were similar in showing that dissolution was limited to the first 50–100 nm in most experiments.

Though these experiments did not produce any readily observable alteration products, there is some indication from profilometry that limited nucleation of new phases may have occurred. The durations (90 days or less) of these experiments at the chosen experimental conditions may simply have been too short to dissolve the solid sufficiently to saturate the fluids with the concentration of dissolved cations necessary for production of new phases.

The results of the experiments performed here are analogous to the very beginning of both chemical weathering of olivine in surface environments and alteration of olivine in hydrothermal circulation environments. In these environments, the

composition of fluid and its interaction with olivine will vary considerably depending on many more variables than can be reproduced experimentally. We attempted to select experimental conditions that have the broadest impact in these environments. Though the effects of fluid–mineral interaction in different natural systems will vary, we have shown that neutral and low pH fluids interacting with olivine have the general result of dissolving Mg^{2+} from the surface of olivine grains, protonation of vacant octahedral sites with H^{+} ions from the fluid, and roughening of surfaces resulting from this transfer of ions and possible nucleation of alteration phases.

Acknowledgements

This manuscript is a portion of M.T. DeAngelis' dissertation work at the University of Tennessee, Knoxville. Many thanks to Jay Jellison at Oak Ridge National Laboratory for help with profilometry, Larry Anovitz at Oak Ridge National for help with SEM analyses, and Sharon Hull, Brandi Shabaga, and Rong Liu at the University of Manitoba with SIMS analyses. Special thanks to Dave Wesolowski and the other members of the Geochemistry and Interfacial Sciences group at Oak Ridge National Laboratory for their support of this research. This research was supported by the Division of Chemical Sciences, Geosciences, and Biosciences, Office of Basic Energy Sciences, U.S. Department of Energy. Oak Ridge National Laboratory is managed and operated by UT-Battelle for the U.S. Department of Energy under contract DE-AC05-00OR22725.

References Cited

Allen, D. E. and Seyfried, W. E. (2003) Compositional controls on vent fluids from ultramatic-hosted hydrothermal systems at mid-ocean ridges: An experimental study at 400 degrees C, 500 bars. *Geochimica et Cosmochimica Acta* **67**, 1531-1542.

Alt, J. C. (1995) Subseafloor processes in mid-ocen ridge hydrothermal systems. In: Humphris, S. E., Zierenberg, R. A., Mullineaux, L. S., and Thompson, R. E. Eds., *Geophysical Monograph 91 Seafloor Hydrothermal Systems: Physical, Chemical, Biological, and Geological Interactions.* American Geophysical Union, Washington, DC.

Awad, A., van Groos, A. F. K., and Guggenheim, S. (2000) Forsteritic olivine: Effect of crystallographic direction on dissolution kinetics. *Geochimica et Cosmochimica Acta* **64**, 1765-1772.

Berndt, M. E., Allen, D. E., and Seyfried, W. E. (1996) Reduction of CO_2 during serpentinization of olivine at 300 °C and 500 bar. *Geology* **24**, 351-354.

Berner, R. A., Holdren, G. R., and Schott, J. (1985) Surface-Layers on Dissolving Silicates - Comment. *Geochimica et Cosmochimica Acta* **49**, 1657-1658.

Bischoff, J. L. and Seyfried, W. E. (1978) Hydrothermal Chemistry of Seawater from 25 °C to 350 °C. *American Journal of Science* **278**, 838-860.

Blum, A. and Lasaga, A. (1988) Role of Surface Speciation in the Low-Temperature Dissolution of Minerals. *Nature* **331**, 431-433.

Bowen, N. L. and Tuttle, O. F. (1949) The System $MgO–SiO_2–H_2O$. *Geological Society of America Bulletin* **60**, 439-460.

Brady, P. V. and Walther, J. V. (1989) Controls on Silicate Dissolution Rates in Neutral and Basic Ph Solutions at 25 °C. *Geochimica et Cosmochimica Acta* **53**, 2823-2830.

Brady, P. V. and Walther, J. V. (1992) Surface-Chemistry and Silicate Dissolution at Elevated-Temperatures. *American Journal of Science* **292**, 639-658.

Brantley, S. (2008) Kinetics of mineral dissolution. In: Brantley, S., Kubicki, J. D., and White, A. F. Eds.*The Kinetics of Water-Rock Interactions*. Springer, New York.

Brantley, S. L. (2003) Reaction kinetics of primary rock=forming minerals under ambient conditions. In: Drever, J. I. Ed., *Fresh water geochemistry, weathering, and soils*. Pergamon Press, Oxford.

Casey, W. H. and Westrich, H. R. (1992) Control of Dissolution Rates of Orthosilicate Minerals by Divalent Metal Oxygen Bonds. *Nature* **355**, 157-159.

Chen, Y. and Brantley, S. L. (2000) Dissolution of forsteritic olivine at 65 °C and 2 < pH < 5. *Chemical Geology* **165**, 267-281.

Chernosky, J. V. (1975) Aggregate refractive-indexes and unit-cell paramaters of synthetic serpentine in the system MgO-Al2O3-SiO2-H2O. *American Mineralogist* **60**, 200-208.

Chevrier, V. and Mathe, P. E. (2007) Mineralogy and evolution of the surface of Mars: A review. *Planetary and Space Science* **55**, 289-314.

Dungan, M. A. (1977) Metastability in serpentine-olivine equilibria. *American Mineralogist* **62**, 1018-1029.

Evans, B. W. (2004) The serpentinite multisystem revisited: Chrysotile is metastable. *International Geology Review* **46**, 479-506.

Fisher, A. T., Becker, K., and Narasimhan, T. N. (1994) Off-Axis Hydrothermal Circulation - Parametric Tests of a Refined Model of Processes at Deep-Sea Drilling Project Ocean Drilling Program Site 504. *Journal of Geophysical Research-Solid Earth* **99**, 3097-3121.

Grandstaff, D. E. (1978) Changes in Surface-Area and Morphology and Mechanism of Forsterite Dissolution. *Geochimica et Cosmochimica Acta* **42**, 1899-1901.

Grauby, O., Baronnet, A., and Devouard, B. (1998) Chrysotile-to-polygonal serpentines-to-lizardite reaction reproduced from a MgO-SiO_2-H_2O (MSH) gel. *17th General Meeting of the International Mineralogical Association, August 9-14,Toronto Canada, Abstracts and Programs*, A81.

Hanchen, M., Prigiobbe, V., Storti, G., Seward, T. M., and Mazzotti, M. (2006) Dissolution kinetics of fosteritic olivine at 90-150 °C including effects of the presence of CO_2. *Geochimica et Cosmochimica Acta* **70**, 4403-4416.

Hofmann, A. W. (1988) Chemical differentiation of the Earth - The relationship between mantle, continental-crust, and oceanic-crust *Earth and Planetary Science Letters* **90**, 297-314.

Janecky, D. R. and Seyfried, W. E. (1986) Hydrothermal Serpentinization of Peridotite within the Oceanic-Crust - Experimental Investigations of Mineralogy and Major Element Chemistry. *Geochimica et Cosmochimica Acta* **50**, 1357-1378.

Johannes, W. (1968) Experimental investigation of the reaction forsterite + $H_2O \rightleftharpoons$ serpentine + brucite. *Contributions to Mineralogy and Petrology* **19**, 309-315.

Jonckbloedt, R. C. L. (1998) Olivine dissolution in sulphuric acid at elevated temperatures - implications for the olivine process, an alternative waste acid neutralizing process. *Journal of Geochemical Exploration* **62**, 337-346.

Kelley, D. S., Karson, J. A., Blackman, D. K., Fruh-Green, G. L., Butterfield, D. A., Lilley, M. D., Olson, E. J., Schrenk, M. O., Roe, K. K., Lebon, G. T., and Rivizzigno, P. (2001) An off-axis hydrothermal vent field near the Mid-Atlantic Ridge at 30 degrees N. *Nature* **412**, 145-149.

Kelley, D. S., Karson, J. A., Fruh-Green, G. L., Yoerger, D. R., Shank, T. M., Butterfield, D. A., Hayes, J. M., Schrenk, M. O., Olson, E. J., Proskurowski, G., Jakuba, M., Bradley, A., Larson, B., Ludwig, K., Glickson, D., Buckman, K., Bradley, A. S., Brazelton, W. J., Roe, K., Elend, M. J., Delacour, A., Bernasconi, S. M., Lilley, M. D., Baross, J. A., Summons, R. T., and Sylva, S. P. (2005) A serpentinite-hosted ecosystem: The lost city hydrothermal field. *Science* **307**, 1428-1434.

Labotka, T. C., Cole, D. R., Fayek, M., and Anovitz, L. M. (2006) An experimental study of the serpentine cycle: The hydration of dunite. *EOS Trans. AGU* **87(52)**, Fall Meet. Suppl., Abstract V32B-05.

Lemmon, E. W., McLinden, M. O., and Friend, D. G. (2011) Thermophysical properties of fluid systems. In: Linstrom, P. J. and Mallard, W. G. Eds., *NIST Chemsitry WebBook, NIST Standard Reference Database Number 69*. National Institute of Standards and Technology, Gaithersburg, MD 20899.

Liu, Y., Olsen, A. A., and Rimstidt, J. D. (2006) Mechanism for the dissolution of olivine series minerals in acidic solutions. *American Mineralogist* **91**, 455-458.

Luce, R. W., Bartlett, R. W., and Parks, G. A. (1972) Dissolution Kinetics of Magnesium Silicates. *Geochimica et Cosmochimica Acta* **36**, 35-&.

Martin, B. and Fyfe, W. S. (1970) Some experimental and theoretical observations on kinetics of hydration reactions with particular reference to serpentinization. *Chemical Geology* **6**, 185-&.

McCollom, T. M. and Seewald, J. S. (2001) A reassessment of the potential for reduction of dissolved CO_2 to hydrocarbons during serpentinization of olivine. *Geochimica et Cosmochimica Acta* **65**, 3769-3778.

McSween, H. Y., Wyatt, M. B., Gellert, R., Bell, J. F., Morris, R. V., Herkenhoff, K. E., Crumpler, L. S., Milam, K. A., Stockstill, K. R., Tornabene, L. L., Arvidson, R. E., Bartlett, P., Blaney, D., Cabrol, N. A., Christensen, P. R., Clark, B. C., Crisp, J. A., Des Marais, D. J., Economou, T., Farmer, J. D., Farrand, W., Ghosh, A., Golombek, M., Gorevan, S., Greeley, R., Hamilton, V. E., Johnson, J. R., Joliff, B. L., Klingelhofer, G., Knudson, A. T., McLennan, S., Ming, D., Moersch, J. E., Rieder, R., Ruff, S. W., Schroder, C., de Souza, P. A., Squyres, S. W., Wanke, H., Wang, A., Yen, A., and Zipfel, J. (2006) Characterization and petrologic interpretation of olivine-rich basalts at Gusev Crater, Mars. *Journal Of Geophysical Research-Planets* **111**, E02S10.

Moody, J. B. (1976) Serpentinization - Review. *Lithos* **9**, 125-138.

Normand, C., Williams-Jones, A. E., Martin, R. F., and Vali, H. (2002) Hydrothermal alteration of olivine in a flow-through autoclave: Nucleation and growth of serpentine phases. *American Mineralogist* **87**, 1699-1709.

O'Hanley, D. S. and Dyar, M. D. (1998) The composition of chrysotile and its relationship with lizardite. *Canadian Mineralogist* **36**, 727-739.

O'Hanley, D. S. and Wicks, F. J. (1995) Conditions of Formation of Lizardite, Chrysotile and Antigorite, Cassiar, British-Columbia. *Canadian Mineralogist* **33**, 753-773.

Oelkers, E. H. (2001) An experimental study of forsterite dissolution rates as a function of temperature and aqueous Mg and Si concentrations. *Chemical Geology* **175**, 485-494.

Olsen, A. A., Brantley, S. L., and Kijbicki, J. D. (2008) Developing models to predict silicate mineral dissolution. *Geochimica et Cosmochimica Acta* **72**, A705-A705.

Olsen, A. A. and Rimstidt, J. D. (2007) Using a mineral lifetime diagram to evaluate the persistence of olivine on Mars. *American Mineralogist* **92**, 598-602.

Olsen, A. A. and Rimstidt, J. D. (2008) Oxalate-promoted forsterite dissolution at low pH. *Geochimica et Cosmochimica Acta* **72**, 1758-1766.

Pokrovsky, O. S. and Schott, J. (2000a) Forsterite surface composition in aqueous solutions: A combined potentiometric, electrokinetic, and spectroscopic approach. *Geochimica et Cosmochimica Acta* **64**, 3299-3312.

Pokrovsky, O. S. and Schott, J. (2000b) Kinetics and mechanism of forsterite dissolution at 25 °C and pH from 1 to 12. *Geochimica et Cosmochimica Acta* **64**, 3313-3325.

Rimstidt, J. D., Brantley, S., and Olsen, A. A. (in press) Systematic review of forsterite dissolution rate data. *Geochimica et Cosmochimica Acta*.

Rosenberg, N. D., Spera, F. J., and Haymon, R. M. (1993) The relationship between flow and permeability field in sea-floor hydrothermal systems. *Earth and Planetary Science Letters* **116**, 135-153.

Rosso, J. J. and Rimstidt, J. D. (2000) A high resolution study of forsterite dissolution rates. *Geochimica et Cosmochimica Acta* **64**, 797-811.

Seyama, H., Soma, M., and Tanaka, A. (1996) Surface characterization of acid-leached olivines by X-ray photoelectron spectroscopy. *Chemical Geology* **129**, 209-216.

Seyfried, W. E. and Bischoff, J. L. (1979) Low-Temperature Basalt Alteration by Seawater - Experimental-Study at 70 °C and 150 °C. *Geochimica et Cosmochimica Acta* **43**, 1937-1947.

Seyfried, W. E. and Bischoff, J. L. (1981) Experimental Seawater-Basalt Interaction at 300 °C, 500 Bar, Chemical-Exchange, Secondary Mineral Formation and Implications for the Transport of Heavy-Metals. *Geochimica et Cosmochimica Acta* **45**, 135-147.

Seyfried, W. E. and Dibble, W. E. (1980) Seawater-Peridotite Interaction at 300 °C and 500 Bars - Implications for the Origin of Oceanic Serpentites. *Geochimica et Cosmochimica Acta* **44**, 309-321.

Seyfried, W. E., Foustoukos, D. I., and Fu, Q. (2007) Redox evolution and mass transfer during serpentinization: An experimental and theoretical study at 200 °C, 500 bar with implications for ultramafic-hosted hydrothermal systems at Mid-Ocean Ridges. *Geochimica et Cosmochimica Acta* **71**, 3872-3886.

Seyfried, W. E. and Mottl, M. J. (1982) Hydrothermal Alteration of Basalt by Sea-Water under Seawater-Dominated Conditions. *Geochimica et Cosmochimica Acta* **46**, 985-1002.

Seyfried, W. E. J., Foustoukos, D. I., and Allen, D. E. (2004) Ultramafic-hosted hydrothermal systems at mid-ocean ridges: Chemical and physical controls on

pH, redox, and carbon reduction reactions. In: German, C. R., Lin, J., and Parson, L. M. Eds., *Geophysical Monograph 148 Mid-Ocean Ridges: Hydrothermal Interactions between the Lithosphere and Oceans.* American Geophysical Union, Washington, DC.

Siegel, D. I. and Pfannkuch, H. O. (1984) Silicate Mineral Dissolution at pH 4 and near Standard Temperature and Pressure. *Geochimica et Cosmochimica Acta* **48**, 197-201.

Siever, R. and Woodford, N. (1979) Dissolution Kinetics and the Weathering of Mafic Minerals. *Geochimica et Cosmochimica Acta* **43**, 717-724.

Snow, J. E. and Dick, H. J. B. (1995) Pervasive Magnesium Loss by Marine Weathering of Peridotite. *Geochimica et Cosmochimica Acta* **59**, 4219-4235.

Staudigel, H. (2003) Hydrothermal alteration processes. In: Holland, H. D. and Turekian, K. K. Eds., *Treatise of Geochemistry*.

Stein, C. A. and Stein, S. (1994) Constraints on Hydrothermal Heat-Flux through the Oceanic Lithosphere from Global Heat-Flow. *Journal of Geophysical Research-Solid Earth* **99**, 3081-3095.

Vanherk, J., Pietersen, H. S., and Schuiling, R. D. (1989) Neutralization of Industrial-Waste Acids with Olivine - the Dissolution of Forsteritic Olivine at 40 Degrees-C70 Degrees-C. *Chemical Geology* **76**, 341-352.

Wegner, W. W. and Ernst, W. G. (1983) Experimentally determined hydration and dehydration reaction rates in the system MgO-SiO_2-H_2O. *American Journal of Science* **283-A**, 151-180.

Westrich, H. R., Cygan, R. T., Casey, W. H., Zemitis, C., and Arnold, G. W. (1993) The Dissolution Kinetics of Mixed-Cation Orthosilicate Minerals. *American Journal of Science* **293**, 869-893.

Wheat, C. G. and Mottl, M. J. (2000) Composition of pore and spring waters from Baby Bare: Global implications of geochemical fluxes from a ridge flank hydrothermal system. *Geochimica et Cosmochimica Acta* **64**, 629-642.

Wogelius, R. A. and Walther, J. V. (1991) Olivine Dissolution at 25 °C - Effects of pH, CO_2, and Organic-Acids. *Geochimica et Cosmochimica Acta* **55**, 943-954.

Wogelius, R. A. and Walther, J. V. (1992) Olivine Dissolution Kinetics at near-Surface Conditions. *Chemical Geology* **97**, 101-112.

Zhao, Y. H., Ginsberg, S., and Kohlstedt, D. L. (2001) Experimental investigation on water solubility in olivine single crystals with different Fe content. *Acta Petrologica Sinica* **17**, 123-128.

Appendix VI

Table VI-1. Experimental conditions and results

Experiment group	Temperature (°C)	External pressure (bar)	Duration (days)	Capsule type	Experiment name*	Initial fluid weight (g)	Fluid–mineral ratio (by mass)	Initial fluid pH	Final fluid pH	Sample number	Initial sample weight (g)	Final sample weight (g)	Sample weight loss (%)
01	150	1	14	Pyrex	W01	0.5576	5:1	7	8.33	1	0.0564	0.0562	0.35
										2	0.0549	0.0549	0.02
					H01	0.3864	5:1	2	7.53	1	0.0333	0.0332	0.22
										2	0.0415	0.0414	0.17
					S01	0.4568	5:1	2	7.32	1	0.0379	0.0378	0.01
										2	0.0512	0.0511	0.01
02	150	1	28	Pyrex	W02	0.5255	5:1	7	7.45	1	0.0433	0.0433	0.07
										2	0.0606	0.0605	0.01
					H02	0.4352	5:1	2	6.72	1	0.0345	0.0065	–
										2	0.0511	0.0510	0.22
					S02	0.4699	5:1	2	6.73	1	0.0387	0.0386	0.01
										2	0.0527	0.0526	0.01
03	25	1	16	Pyrex	W03	0.5536	5:1	7	7.71	1	0.0477	0.0476	0.01
										2	0.0618	0.0618	0.00
					H03	0.4587	5:1	2	2.59	1	0.0435	0.0435	0.11
										2	0.0471	0.0470	0.12
					S03	0.4420	5:1	2	4.24	1	0.0443	0.0442	0.01
										2	0.0446	0.0445	0.01
04	150	1	1	Pyrex	W04	0.3856	5:1	7	8.15	1	0.0331	0.0330	0.07
										2	0.0427	0.0427	0.04
					H04	0.3944	5:1	2	6.17	1	0.0484	0.0483	0.20
										2	0.0286	0.0286	0.16
					S04	0.5547	5:1	2	4.94	1	0.0345	0.0344	0.01
										2	0.0761	0.0646	1.15

* Experiment name starting is related to solution type used; 'W' = deionized H_2O, 'H' = 0.01 M HCl, 'S' = 0.005 M H_2SO_4

** S06 sample 2 split into two pieces (2a & 2b); weight loss was calculated using the combined weight of these two pieces

Table VI-1. (Continued)

Experiment group	Temperature (°C)	External pressure (bar)	Duration (days)	Capsule type	Experiment name*	Initial fluid weight (g)	Fluid–mineral ratio (by mass)	Initial fluid pH	Final fluid pH	Sample number	Initial sample weight (g)	Final sample weight (g)	Sample weight loss (%)
05	25	1	43	Pyrex	W05	0.5511	5:1	7	7.65	1	0.0664	0.0664	0.01
										2	0.0436	0.0436	0.02
					H05	0.524	5:1	2	4.15	1	0.0705	0.0704	0.12
										2	0.0342	0.0341	0.19
					S05	0.7035	5:1	2	3.66	1	0.0521	0.0520	0.01
										2	0.0865	0.0863	0.02
06	150	1	29	Pyrex	W06	1.0815	15:1	7	8.76	1	0.0403	0.0403	0.00
										2	0.0310	0.0310	0.06
					H06	1.6238	15:1	2	–	1	0.0422	0.0420	0.66
										2	0.0645	0.0643	0.34
					S06**	1.5045	15:1	2	6.14	1	0.0644	0.0640	0.04
										2a	0.0323	0.0243	0.04
										2b	–	0.0077	–
07	25	1	63	Pyrex	W07	0.6071	5:1	7	7.15	1	0.0938	0.0938	0.02
										2	0.0272	0.0259	4.83
					H07	0.4945	5:1	2	4.15	1	0.0706	0.0705	0.15
										2	0.0273	0.0272	0.22
					S07	0.4773	5:1	2	3.84	1	0.0468	–	–
										2	0.0461	–	–

Table VI-1.(Continued)

Experiment group	Temperature (°C)	External pressure (bar)	Duration (days)	Capsule type	Experiment name*	Initial fluid weight (g)	Fluid–mineral ratio (by mass)	Initial fluid pH	Final fluid pH	Sample number	Initial sample weight (g)	Final sample weight (g)	Sample weight loss (%)
08	150	50	28	gold	W08	0.4467	5:1	7	–	1	0.0889	0.0888	0.06
					H08	0.35442	5:1	2	–	1	0.0683	0.0680	0.40
					S08	0.3673	5:1	2	–	1	0.0735	0.0717	0.18
09	150	50	90	gold	W09	0.2647	5:1	7	–	1	0.0508	–	–
					H09	0.26801	5:1	2	–	1	0.0502	–	–
					S09	0.2682	5:1	2	–	1	0.0527	–	–
10	300	200	34	gold	W10	0.3070	5:1	7	–	1	0.0618	–	–
					H10	0.30734	5:1	2	–	1	0.0570	–	–
					S10	0.3002	5:1	2	–	1	0.0588	–	–
11	150	1	34	gold	W11	0.1369	5:1	7	–	1	0.0263	0.0259	1.22
					H11	0.21226	5:1	2	–	1	0.0406	0.0405	0.39
					S11	0.1184	5:1	2	–	1	0.0023	0.0023	0.00

Table VI-2. Surface roughness parameters measured by 2D profilometry before and after experiment*

Experiment group	Experiment name	Before experiment roughness parameters					After experiment roughness parameters				
		Ra (nm)	*Rq* (nm)	*Rp* (nm)	*Rv* (nm)	*Rt* (nm)	*Ra* (nm)	*Rq* (nm)	*Rp* (nm)	*Rv* (nm)	*Rt* (nm)
08	W08	3.8	4.7	6.5	13.5	20.0	7.3	16.0	167.4	17.1	184.6
	H08	2.4	3.1	8.2	12.5	20.7	23.4	30.2	107.2	81.3	188.5
	S08	2.5	3.0	8.3	10.3	18.6	8.0	12.1	64.0	24.1	88.1
09	W09	2.6	3.2	8.4	5.1	13.5	46.9	58.7	231.2	61.2	292.4
	H09	3.9	4.9	14.3	16.6	30.9	103.9	322.5	2328.7	1196.3	3525.0
	S09	3.1	3.9	9.5	12.5	22.0	21.6	31.4	130.4	152.6	283.0
10	W10	5.3	7.9	38.0	19.1	57.1	6.3	21.8	172.1	8.8	180.9
	H10	2.1	3.6	24.8	4.4	29.2	12.9	19.5	102.7	65.3	168.0
	S10	8.0	13.0	111.9	24.8	136.7	69.7	94.7	298.9	380.3	679.1
11	W11	26.8	54.1	222.5	219.3	441.8	14.4	33.5	301.1	27.2	328.3
	H11	4.7	9.1	71.5	10.1	81.6	9.8	20.9	251.8	45.3	297.2
	S11	4.3	5.9	22.3	10.3	32.6	26.6	35.6	221.7	99.7	321.4

* gold capsule experiments only; all parameters determined from leveled and roughness filtered profiles using a least squares leveling method, robust Gaussian filtering, and a cut-off value of 0.1 mm

Table VI-2. (Continued)

Experiment group	Experiment name	Change in roughness parameters				
		Ra change (%)	*Rq* change (%)	*Rp* change (nm)	*Rv* change (nm)	*Rt* change (%)
08	W08	194	339	160.9	3.6	925
	H08	970	969	99.1	68.8	912
	S08	323	398	55.7	13.8	474
09	W09	1792	1840	222.8	56.1	2166
	H09	2658	6532	2314.4	1179.7	11395
	S09	695	808	120.9	140.1	1287
10	W10	118	274	134.1	-10.4	317
	H10	610	539	77.9	60.9	576
	S10	867	729	187.0	355.4	497
11	W11	54	62	78.6	-192.1	74
	H11	207	231	180.3	35.2	364
	S11	614	605	199.4	89.4	987

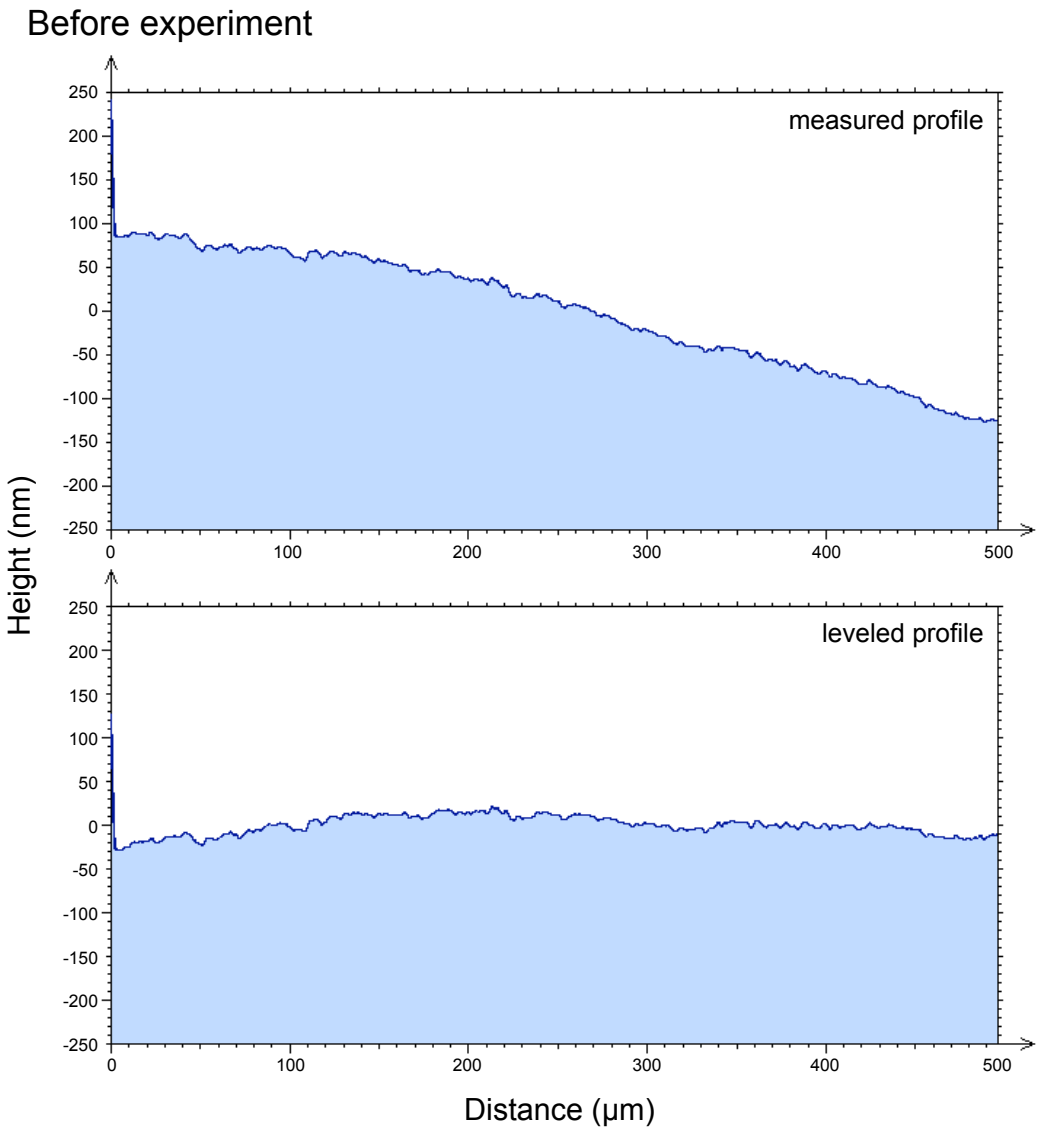

Figure VI-1. Measured and leveled 2D profile scans showing the surface topography of the olivine plate before use in the S08 experiment. The 2D profile was measured by profilometry, and was performed over a distance of 500 µm and contains 20,840 measured points spaced approximately 20 nm apart. The leveled 2D profile was created using a least squares method, and was generated to determine roughness parameters before experiment (see Table VI-2 for parameters).

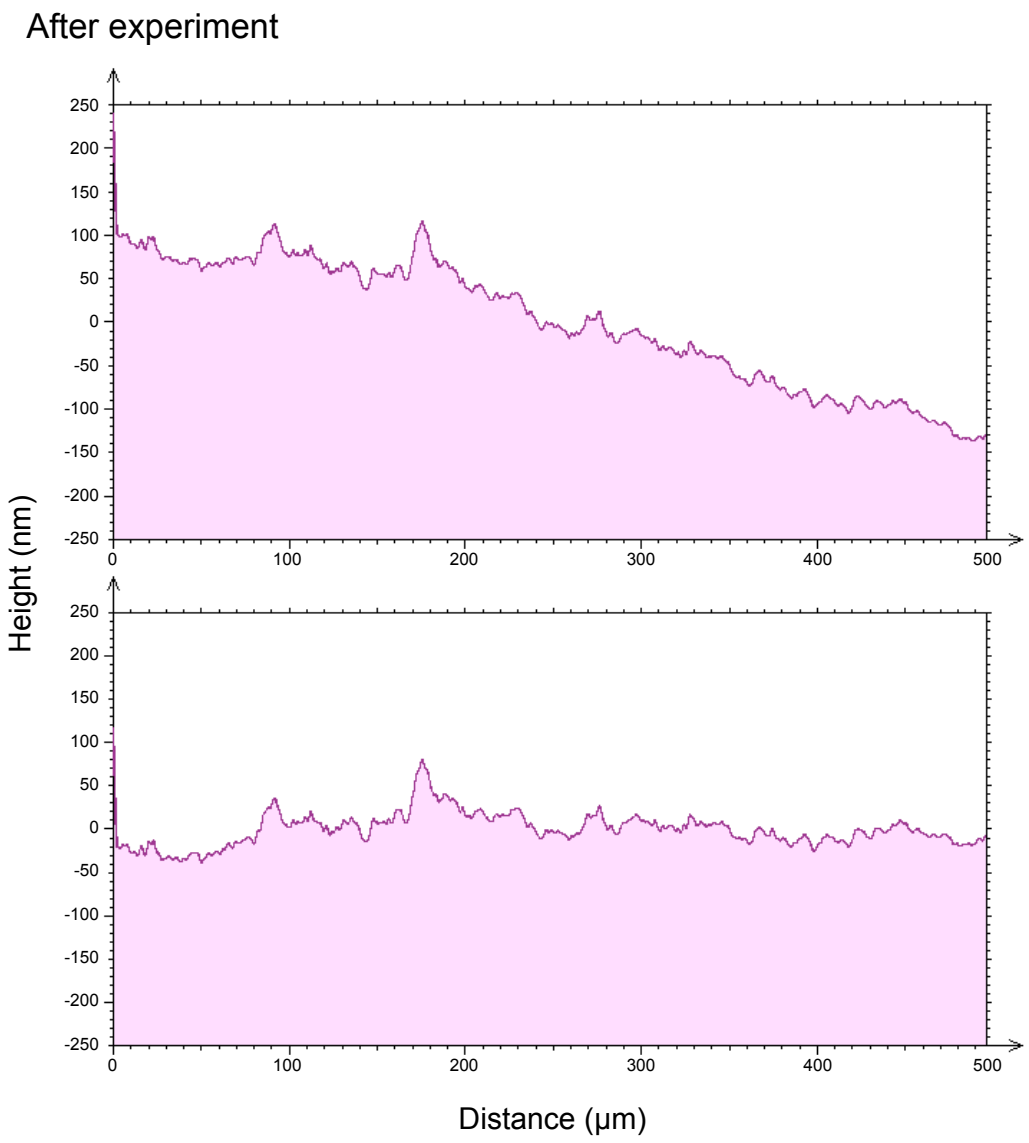

Figure VI-2. Measured and leveled 2D profile scans showing the surface topography of the olivine plate after use in the S08 experiment. The 2D profile was measured by profilometry, and was performed over a distance of 500 μm and contains 20,840 measured points spaced approximately 20 nm apart. The leveled 2D profile was created using a least squares method, and was generated to determine roughness parameters after experiment (see Table VI-2 for parameters).

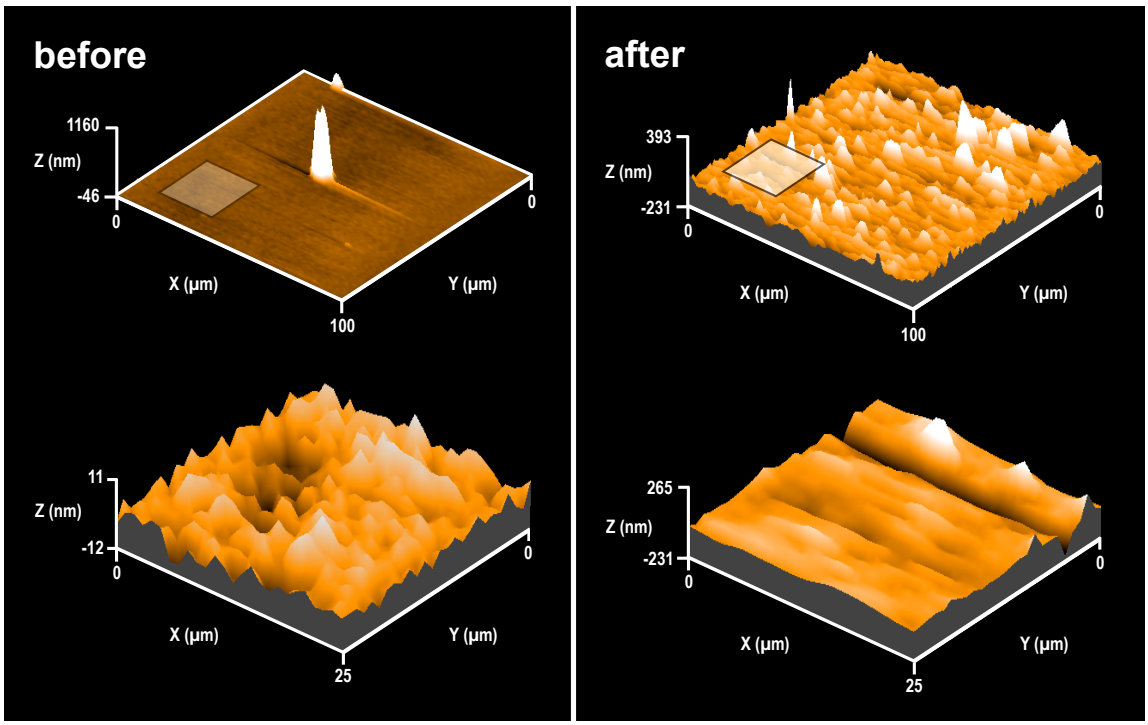

Figure VI-3. Before and after experiment surface topography of the olivine plate used in the S08 experiment. Primary 3D surface scans (100×100 µm) were measured by profilometry, and show an increase from an average relief of ~25 nm before experiment to an average relief of ~250 nm after experiment. Smaller inset 3D area scans (25 × 25 µm) are also shown.

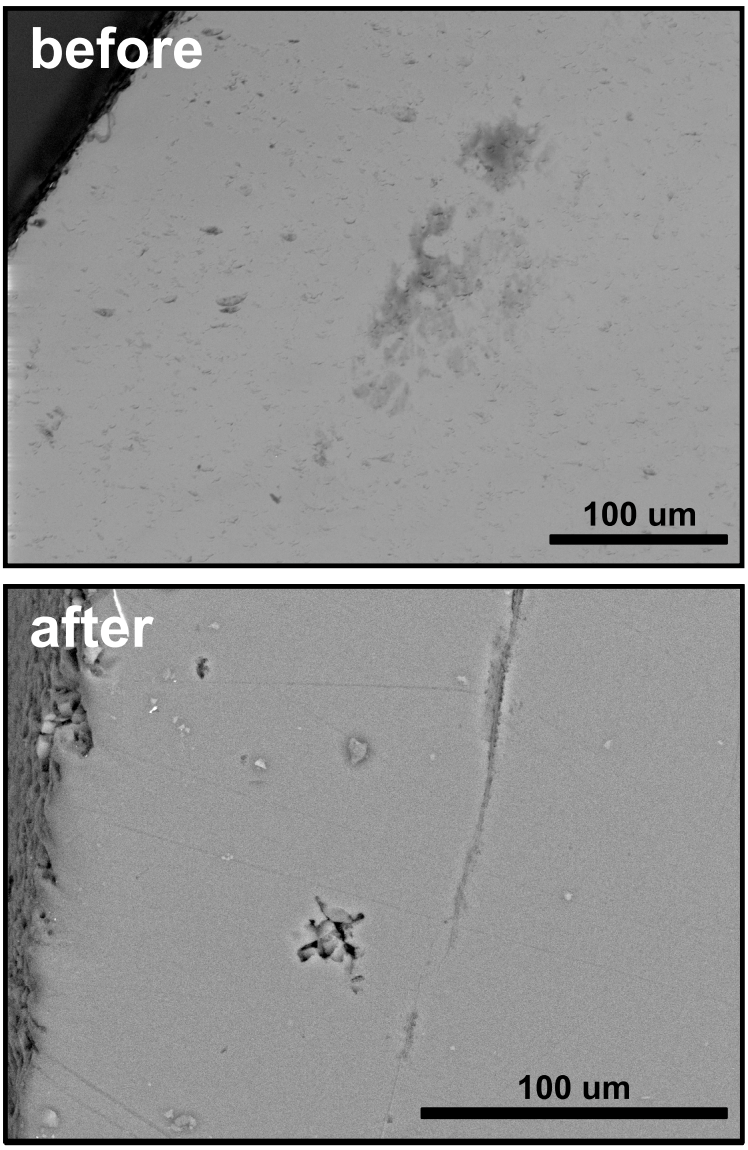

Figure VI-4. SEM images of experiment S09 before and after experiment showing that alteration phases did not form, even for this longest duration (90 days) experiment (see Table VI-1 for experiment conditions).

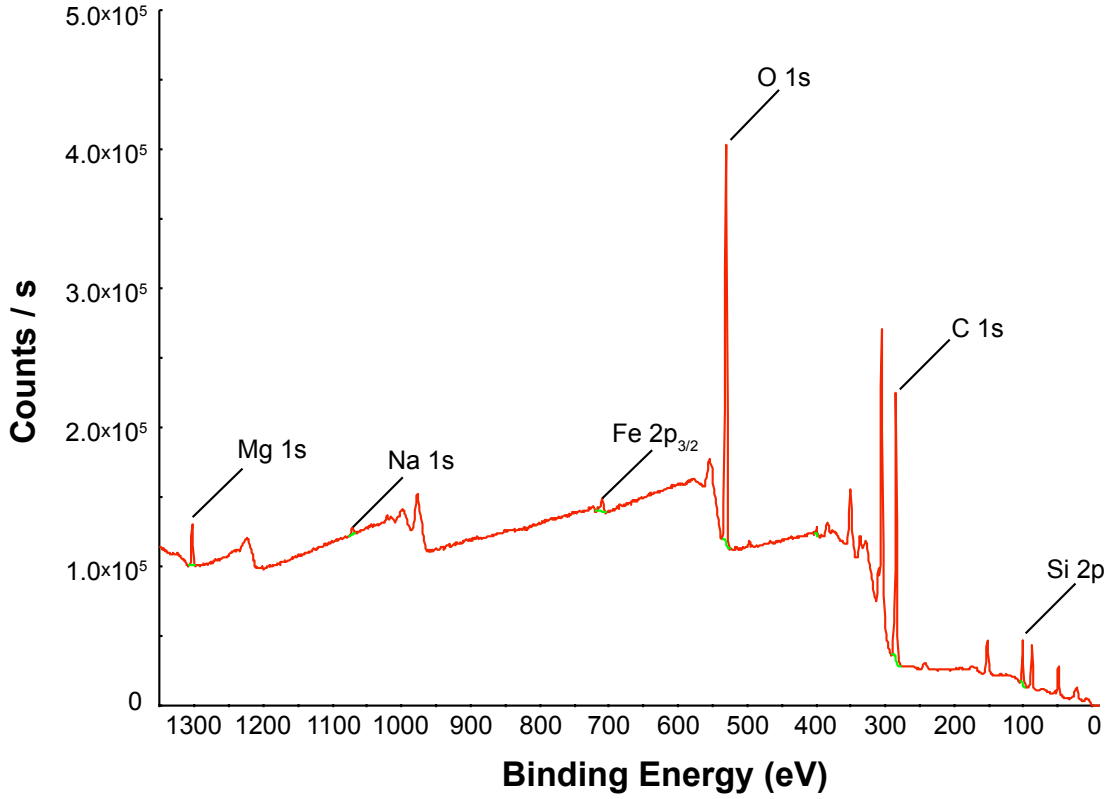

Figure VI-5. XPS survey spectra of unreacted olivine starting material. This survey identified peaks corresponding to O 1s, Mg 1s, Si 2p, C ls, Fe $2p_{3/2}$, and possibly Na 1s.

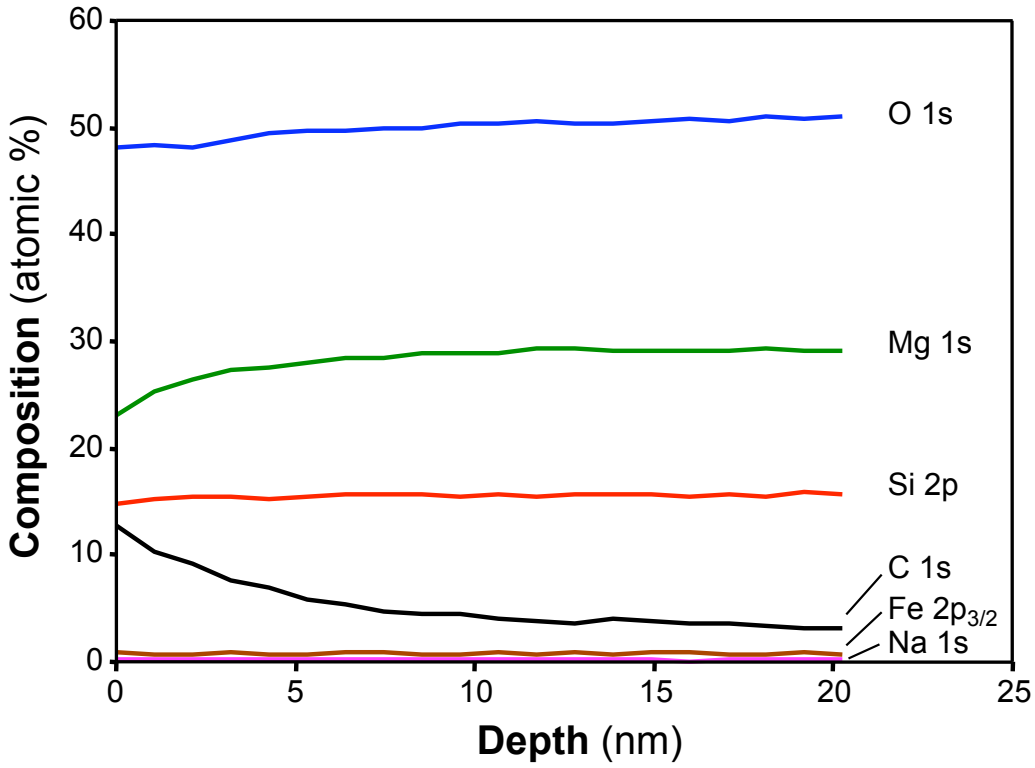

Figure VI-6. XPS depth profile of unreacted starting material showing composition in atomic % versus depth in nanometers.

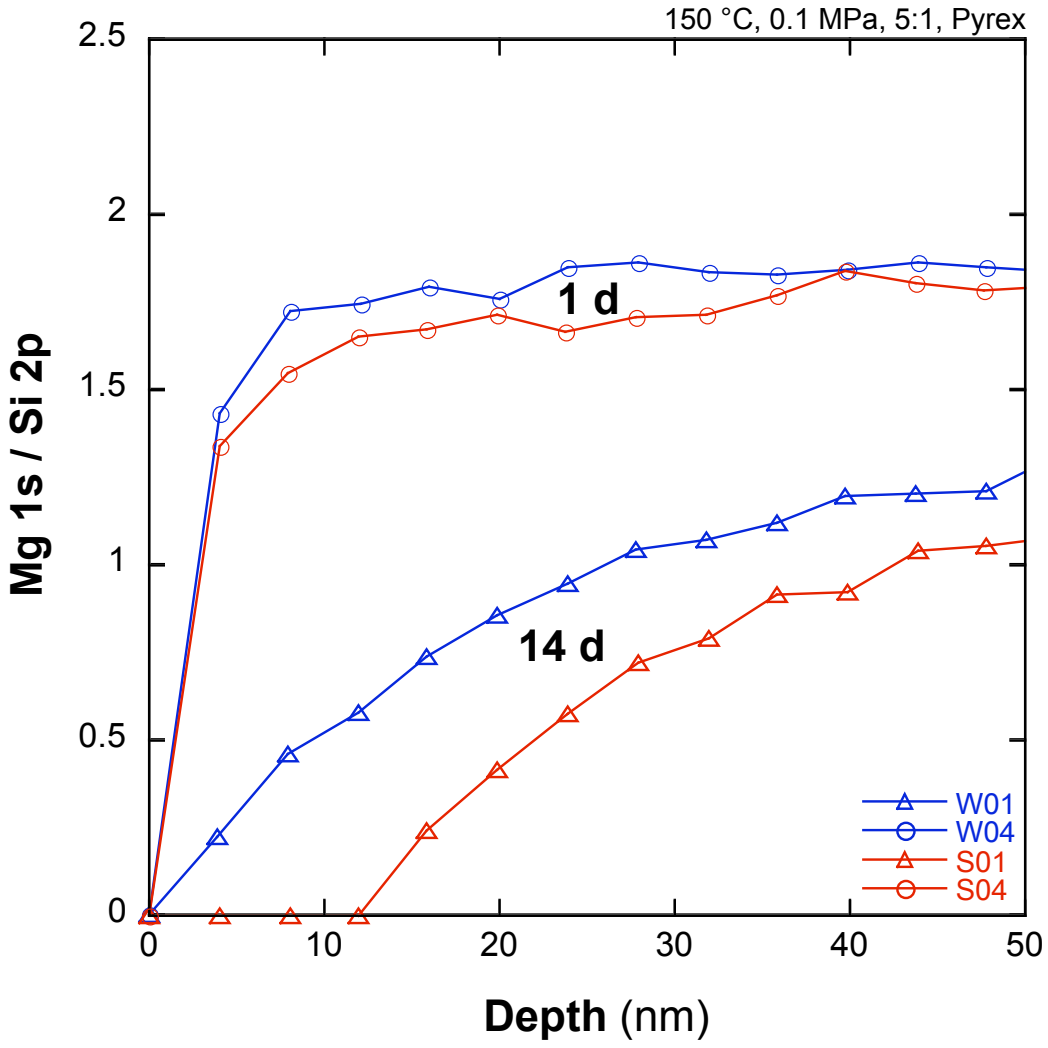

Figure VI-7. XPS depth profiles plotting Mg 1s normalized to Si 2p versus depth from two H_2O experiments and two H_2SO_4 experiments showing the change in Mg concentration with time.

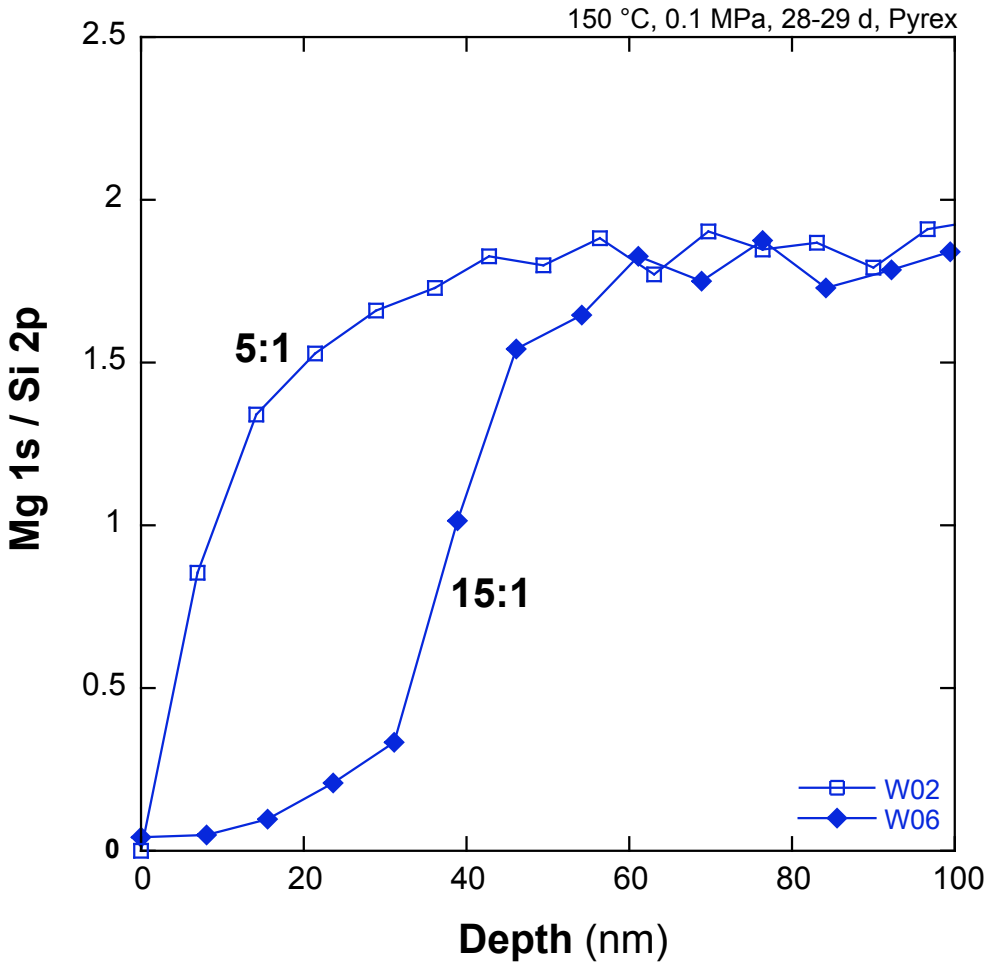

Figure VI-8. XPS depth profiles plotting Mg 1s normalized to Si 2p versus depth from two H_2O experiments showing the change in Mg concentration with fluid–mineral ratio.

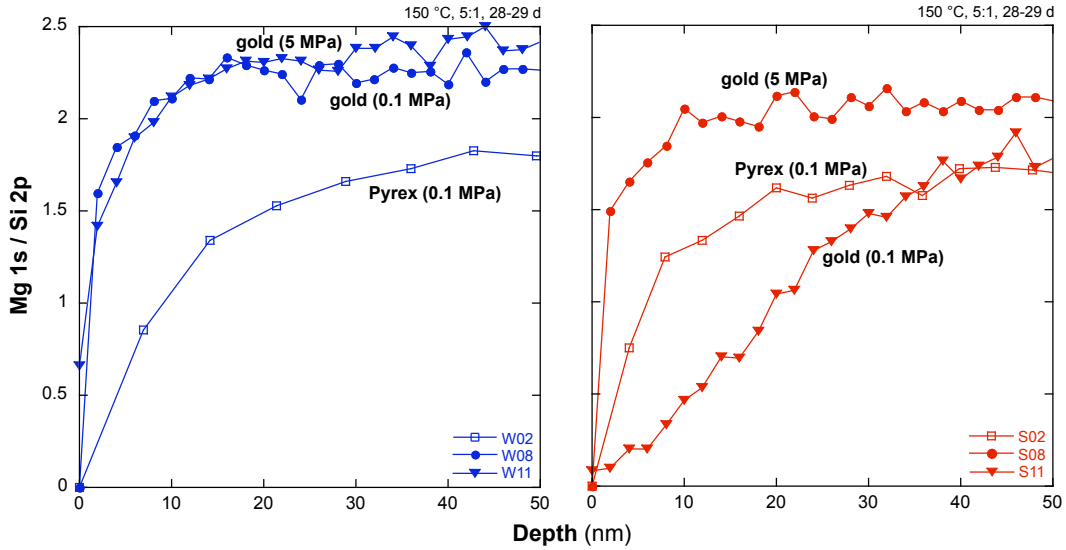

Figure VI-9. XPS depth profiles plotting Mg 1s normalized to Si 2p versus depth from three H_2O experiments and three H_2SO_4 experiments showing the change in Mg concentration with capsule type and external pressure used.

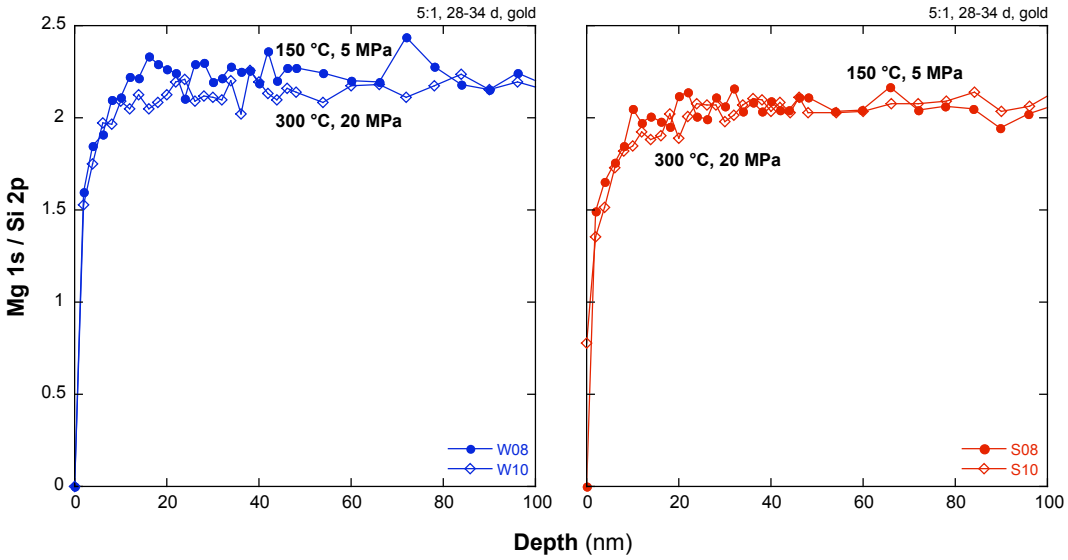

Figure VI-10. XPS depth profiles plotting Mg1s normalized to Si2p versus depth from two H_2O experiments and two H_2SO_4 experiments showing the change in Mg concentration with temperature and external pressure used.

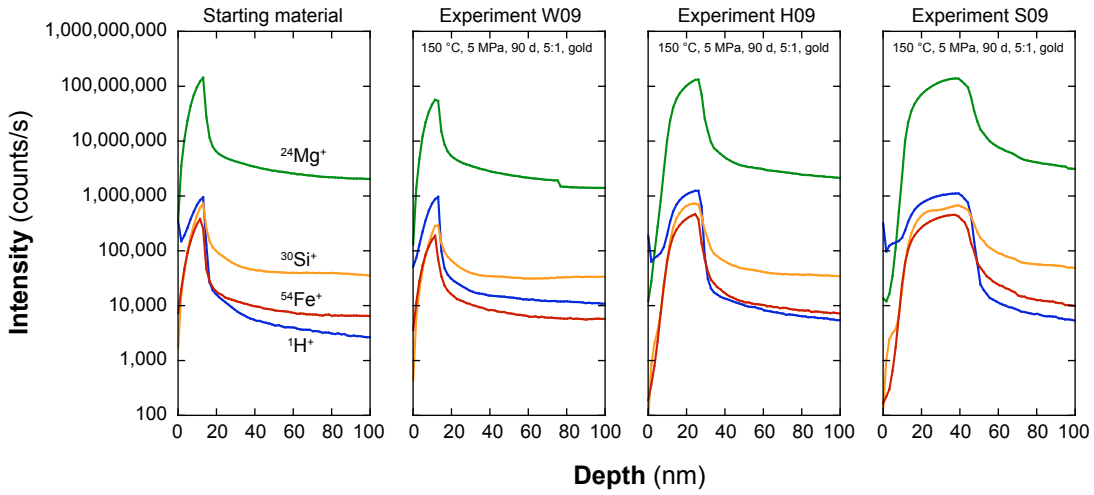

Figure VI-11. SIMS depth profiles of $^1H^+$, $^{24}Mg^+$, $^{30}Si^+$, and $^{54}Fe^+$ for starting material and experiments W09, H09, and S09.

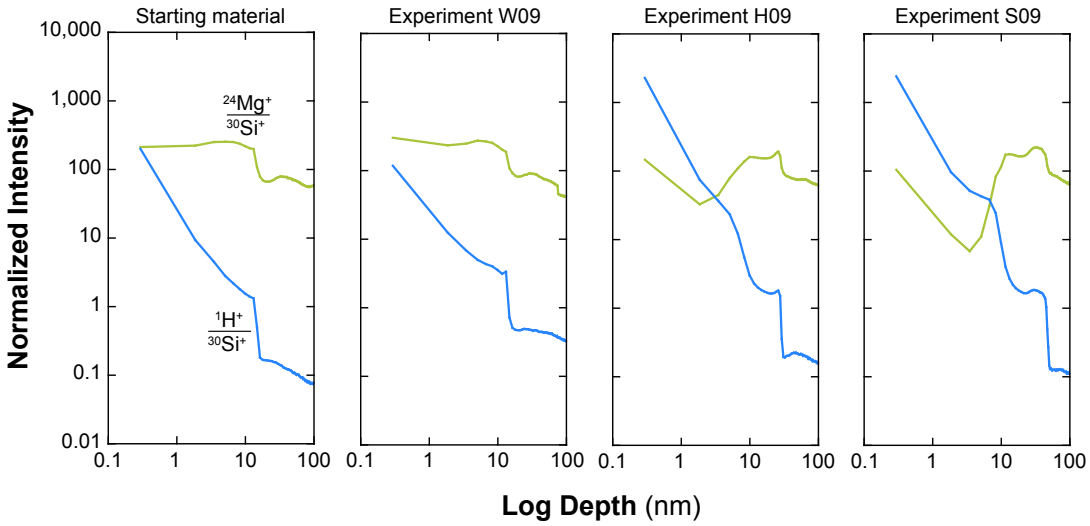

Figure VI-12. SIMS depth profiles of $^{24}Mg^+$ and $^{1}H^+$ normalized to $^{30}Si^+$ for starting material and the W09, H09, and S09 experiments.

Part VII.
Conclusions

The experiments performed in this dissertation were done with the intent of examining fluid–mineral interaction processes as they apply to a variety of natural environments and environmental conditions. The methods used to achieve this goal varied depending on the type of environment under investigation.

In Part II, the role of an $H_2{}^{18}O$-rich fluid reacting with dolomite rock under environmental conditions analogous to contact metamorphism was investigated. These experiments resulted in the production of new mineral phases (calcite and periclase) along grain boundaries, fractures, and the outside of the core. Some dolomite recrystallization was observed by measuring Fe mobility, and ^{18}O from the fluid exchanged with O in reaction products, unreacted dolomite, and recrystallized dolomite. The ^{18}O value of the products of reaction were similar at various locations in the core with a value of $F = 0.14$, and show that these neomorphic phases recorded a mix of both dolomite- and fluid-derived oxygen. Calculated diffusion coefficient estimates from measurement of ^{18}O diffusion into unreacted dolomite was found to be between $D = 1\times10^{-14}$ and 5×10^{-12} cm^2/s. These experiments showed that there was extensive exchange between the extant dolomite and fluid by both recrystallization and diffusion.

In Parts III and IV, new crystal growth techniques were developed for the growth of nanocrystalline fayalite and intermediate composition olivine. Part III developed a wet chemical, sol-gel technique to synthesis the fayalite, and resulted in the production of 100–150 nm sized grains that had surface areas between 27 and 45 m^2/g depending on the surface area measurement method used. This technique was extremely sensitive to oxygen fugacity during the gel formation, gel drying, and calcination stages of synthesis,

so various steps had to be taken to ensure appropriate redox conditions, including: 1) gel formation under flowing argon, 2) gel drying using a rotary evaporator, and 3) calcination under flowing N_2.

Part IV developed a coupled decarbonation and flux-growth method to synthesis olivine crystals having an intermediate, $(Mg_xFe_{1-x})_2SiO_4$ (x=0.4-0.6), composition. This method used a mixture of magnesite, siderite, and an amorphous SiO_2 powder along with a lithium-borate flux to form small (~200 μm), euhedral grains of olivine by heating the mixture under vacuum at 1100 °C. Electron probe microanalysis of these olivine grains showed core to rim growth zoning in both Mg and Fe, and secondary ion microprobe analysis showed core to rim incorporation of Li and B. Use of zone refinement techniques may be possible, resulting in homogenization of these element zones.

Experiments in Parts V and VI used either H_2O or acidic solutions of 0.005 M H_2SO_4 or 0.01 M HCl at low temperature (25–300 °C) and pressure (1 atm up to 20 MPa) to examine processes of dissolution, protonation, and alteration in natural samples of olivine. Part V used San Carlos olivine powders of various sizes to examine the changes to solid and solution that resulted from performing closed system, non-buffered experiments in which the composition and pH of the fluid was allowed to change with time. These experiments resulted in a pH change from pH 2 to near pH 10, but the time to reach this higher pH varied with surface area of the powders and fluid–mineral ratio of the experiments. Geochemical modeling suggests that pH change is related to the precipitation and consummation of several secondary phases (quartz, talc, antigorite, brucite) as dissolution of the olivine powder proceeds. Scanning electron microscope examination of olivine surfaces and powder X-ray diffraction analysis of suspended

powders suggest that both physical and chemical processes were occurring simultaneously. These experiments show that pH is very sensitive to reaction progress, and are representative of natural systems where finite amounts of olivine reacts with finite amounts of fluid.

The experiments in Part VI used single crystal plates of San Carlos olivine to examine the changes to surfaces resulting from interaction with H_2O, HCl, and H_2SO_4 fluid at low temperature and pressure. The use of nanoscale analytical techniques such as profilometry, X-ray photoelectron spectroscopy, and secondary ion mass spectrometry (SIMS) revealed that nearly every experiment showed Mg dissolution up to 100 nm depth on the surfaces of olivine samples, with acidic starting solution experiments generally showing more dissolution than H_2O experiments under similar conditions of temperature, pressure, fluid–mineral ratio, and experiment duration. SIMS analyses were also used to examine the concentration of H^+ ions on the surface, and found that the surfaces of experimental samples became protonated to depths between 10 and 50 nm. Surface roughness parameters were determined by profilometry and showed an increase in surface roughness of over 2000% in some samples. The presence of small peaks identified by profilometry and covering the surface of some samples may be very small (< 50 nm) secondary phases. The results of the experiments performed in this study are analogous to the very beginning of both chemical weathering of olivine in surface environments and alteration of olivine in hydrothermal circulation environments.

The link that connects all of these studies is that experiments were performed under disequilibrium conditions of temperature, pressure, and fluid-mineral ratio. This was done so that chemical and physical responses of the minerals being grown or reacted

with fluid could be observed within the time frame available for experiments. This is different from natural systems in that the amount of time it takes for these processes to occur in nature is generally much slower, but it is similar to natural systems in that the final result of the processes can be the same. The goal of any analog experiment is to determine and describe processes that are known to occur in the real world but are not possible to observe directly because of limits on time, location, or some other combination of environmental conditions. The experiments presented in this dissertation have attempted to do just that, by investigating the interactions of fluids with natural samples of dolomite and olivine under experimental conditions specifically chosen to be analogous to natural conditions.

Vita

Michael Thomas DeAngelis was born on September 21, 1975, in Milwaukee, Wisconsin. He was raised in Waukesha, Wisconsin, where he attended Hadfield Elementary School, Central Middle School, and graduated from Waukesha South High School in 1993. In elementary school, Michael first became interested in the study of geology, having worked on a rewarding independent study project to build a "glacier-in-a-box". He spent countless hours during his childhood exploring the glacially sculpted landscape of the Kettle Moraine area of southeastern Wisconsin and the Wisconsin Northwoods.

After graduating from high school, Michael attended the University of Wisconsin – Madison where he majored in geology with an emphasis in metamorphic petrology. His senior thesis project focused on skarn formation within calc-silicate rocks related to the Morin Anorthosite Massif in Quebec, Canada.

Upon completion of his undergraduate degree in the spring of 1998, Michael worked as a computer programmer for the next four years. He returned to the study of geology in the fall of 2002, attending the Department of Earth and Planetary Sciences at the University of Tennessee under the advising of Dr. Theodore C. Labotka. There his research focused on determining the kinetics of dolomite breakdown commonly associated with metamorphism within contact metamorphic aureoles. He graduated from the University of Tennessee with a Masters of Science in Geology in May of 2005.

In 2006, Michael returned to the University of Tennessee to complete his doctorate degree working again with Dr. Theodore C. Labotka. His dissertation research

presented here focuses on experimental investigations of a variety of fluids–minerals interaction processes.

When Michael finds a few spare moments to pursue other interests besides geology, they generally include playing racquetball, playing on and composing for the piano, losing games of low stakes Texas Hold'em poker, occasional hikes in the mountains, a bit of gardening, a bit of recreational reading, some moderately adventurous cooking, and dining out with good friends. He is known to frequent coffee shops, movie theaters, and farmers markets, but generally not to the point where his presence annoys those around him (to his knowledge).

If asked if he could travel back in time and choose to go through graduate school all over again, he might answer "NO!", but the truth is that he would not trade any of the wonderful experiences, accumulation of knowledge, and lasting friendships he has made in pursuing his graduate degrees. He is optimistic about the future, and is very much looking forward to seeing what comes next.